

**Advances in
Boundary
Element
Techniques VII**

**Edited by
B Gattmiri
A Sellier
M.H Aliabadi**

Advances in Boundary Element Techniques VII

ECi

ISBN 0-9547783-3-2

Advances
In
Boundary Element Techniques VII

Advances
In
Boundary Element Techniques VII

Edited by

B. Gatmiri
A. Sellier
M H Aliabadi

EC_{Ita}

Published by EC, Ltd. , UK
Copyright © 2006, Published by EC Ltd, P.O.Box 425, Eastleigh, SO53 4YQ, England

Phone (+44) 2380 260334

All Rights reserved. No part of this publication may be reproduced, stored in a retrieval system or transmitted in any form or by any means, electronic, mechanical, photocopying, except under terms of the Copyright, Designs and Patents Act 1988.

Requests to the Publishers should be addressed to the Permission Department, EC, Ltd Publications, P.O.Box 425, Eastleigh, Hampshire, SO53 4YQ, England.

ISBN: 0-9547783-3-2

The text of the papers in this book was set individually by the authors or under their supervision.

No responsibility is assumed by the editors or the publishers for any injury and/or damage to person or property as a matter of product liability, negligence or other wise, or from any used or operation of any method, instructions or ideas contained in the material herein.

**International Conference
on
Boundary Element Techniques VII
4-6th September, Paris, France**

Conference Organizing Committee

Professor Behrouz Gatmiri
Ecole Nationale des Ponts et Chaussées
Paris, France

Professor Antoine Sellier
LadHyx, Ecole Polytechnique
Palaiseau Cedex, France

Professor Ferri M H Aliabadi
Imperial College London
London, United Kingdom

International Scientific Advisory Board

Abascal,R	Escuela Superior de Ingenieros Sevilla	Spain
Cisilino,A	Universidad Nacional de Mar del Plata	Argentina
Davies,A	University of Hertfordshire	UK
Denda,M	Rutgers University	USA
Fedeliński,P	Silesian University of Technology	Poland
Frangi,A	Politecnico of Milan	Italy
Gallego,R	University of Granada	Spain
Gaspar,C	Széchenyi István University	Hungary
Gatmiri B.	ENPC, Paris and University of Tehran	France
Gray,L	Oak Ridge National Laboratory	USA
Hirose,S	Tokyo Institute of Technology	Japan
Ingham,D.B	University of Leeds	UK
Kinnas,S.A	The University of Texas at Austin	USA
Mallardo,V	University of Ferrara	Italy
Mantic,V	University of Seville	Spain
Mattheij,R	University of Eindhoven	Netherlands
Mikhailov,S	Glasgow Caledonian University	UK
Minutolo,V	University of Naples Second	Italy
Mohamad Ibrahim,M.N	Universiti Sains Malaysia	Malaysia
Ochiai,Y	Kinki University	Japan
Perez-Gavilan,J.J	UNAM	Mexico
Selvadurai,A.	McGill University	Canada
Sarler,B	University of Maribor	Slovenia
Sladek,J	Slovak Academy of Sciences	Slovakia
Sollero.P.	UNICAMP	Brazil
SapountzakisE,J	National Technical University	Greece
Song,C	University of New South Wales	Australia
Tanaka,M	Shinshu University	Japan
Telles,J.C.F.	Federal University of Rio de Janeiro	Brazil
Venturini,W.S.	University of São Paulo	Brazil
Wen,P.H.	Queen Mary, University of London	UK
Wrobel,L.C.	Brunel University	UK
Yao,Z	Tsinghua University	China
Zhang,Ch.	University of Siegen	Germany

PREFACE

The Conferences in Boundary Element Techniques are devoted to fostering the continued involvement of the research community in identifying new problem areas, mathematical procedures, innovative applications and novel solution techniques in boundary element methods (BEM). Previous successful conferences devoted to Boundary Element Techniques were held in London, UK (1999), New Jersey, USA (2001), Beijing, China (2002), Granada, Spain (2003), Lisbon, Portugal (2004), and Montreal, Canada (2005)

The present volume is a collection of edited papers that were accepted for presentation at the Boundary Element Techniques Conference held at École Nationale des Ponts et Chaussées, Paris, France, during 4-6th September 2006. Research papers received from 21 countries formed the basis for the Technical Program. The themes considered for the technical program included, solid mechanics, heat and fluid flow, composite materials, fracture mechanics, damage mechanics, contact and wear, optimization, dynamics and vibrations, acoustics and computational and mathematical aspects. Some of the papers presented at the conferences will be published in special issues of *Communications in Numerical Methods in Engineering*, *Computer Methods in Engineering and Sciences*, *Electronic Journal for Boundary Elements* and *Structural Durability and Health Monitoring*.

The Keynote Lectures were given by Jean-Claude Nedelec, Leonard Gray and Marc Bonnet. Other invited presentations were given by R.Abascal, A. Davies, D.Ingham, A.Frangi, V.Mantic, Y.Ochiai, and J.C.F.Telles.

The organizers are indebted to École Nationale des Ponts et Chaussées (ENPC) for their support of the meeting. The organizers would also like to express their appreciation to the International Scientific Advisory Board for their assistance in supporting and promoting the objectives of the meeting and for their assistance in the form of reviews of the submitted papers.

Editors
September 2006

Table of Contents

Modelling Microfracture in Polycrystalline Materials G.K.Sfantos and M.H.Aliabadi	1
BEM Poroplastic Analysis Applied to Reinforced Solids W.W. Wutzow, A.S. Botta, W.S. Venturini and A. Benallal	7
Boundary Problem for Percussive Deep Drilling Modeling by BEM S.E.Mikhailov and I.V.Namestnikova	15
Computation of Dynamic Stress Intensity Factors in 2-D Anisotropic Elastic Solids: A Comparison of Two Time-Domain BEM S. Beyer, M. Wünsche, Ch. Zhang, S. Hirose, J. Sladek and V. Sladek	23
Inverse acoustic scattering by higher-order topological expansion of misfit function M. Bonnet	29
Analysis and Optimization of Dynamically Loaded Reinforced Plates by the Coupled Boundary and Finite Element Method P. Fedelinski and R. Gorski	33
Local buckling of thin walled structures by BEM P.M.Baiz and M.H.Aliabadi	39
A Procedure to Solve Generalized Plane Problems with Contact Using a 2D BEM Code A. Blázquez, V. Mantič and F. París	45
Accelerating Fluid layers G.Baker	51
Accurate Modelling of Rigid and Soft Inclusions in 2D Elastic Solids by the Boundary Element Method L.G. S. Leite and W.S. Venturini	57
Boundary Elements for Elastoplastic Solids without Domain Integrals M. Brun, K. Bertoldi and D. Bigoni	63
Time-domain BEM Formulation Applied to the Solution of the Scalar Wave Equation: a Step-by-Step Approach J. A. M. Carrer and W. J. Mansur	67
Meshless Boundary Interpolation: Local and Global Multi-Level Techniques C. Gáspár	73
FMM accelerated BEM for 3D Laplace & Helmholtz Equations N.A.Gumerov and R. Duraiswami	79

An Iterative Boundary Element Method for the Determination of a Spacewise Dependent Heat Source T.Johansson and D.Lesnic	85
Unsteady Panel Method for Oscillating Foils M. La Mantia and P. Dabnichki	91
Improving Secondary Recovery of an Oil Reservoir Using Hot Water M. N. Mohamad Ibrahim and S. Shuib	97
Three-Dimensional Elastoplastic Analysis by Triple-Reciprocity Boundary Element Method Y. Ochiai	103
Boundary Element Analysis of Cracked Sheets Repaired with Adhesively Bonded Anisotropic Patches J.Useche, P.Sollero and E.L. Albuquerque	109
Dynamic Analysis of Piezoelectric Structures by the Dual Reciprocity Boundary Element Method G. Dziatkiewicz and P. Fedelinski	121
Local Radial Basis Function Collocation Method for Heat Transfer and Fluid Flow Problems B. Šarler	127
Dual Reciprocity Boundary Element Analysis of Steady-state Heat Conduction in Nonlinear Anisotropic Materials K.M.Singh and M.Tanaka	133
Cracked Orthotropic Strip Dynamic Analysis by Displacement Discontinuity Method P.H.Wen ,M.H.Aliabadi ,J.Sladek and V.Sladek	139
Numerical Determination of the Mode-I Crack SIF in Gradient Elastic Materials via the BEM G.F. Karlis, S. V. Tsinopoulos and D. Polyzos	145
A Boundary Integral Method for iterative solution of scattering problems with variable impedance surface condition F.Collino,F.Millot and S.Pernet	153
Dual BEM for fracture analysis of magnetoelastoelectroelastic solids F. García-Sánchez, A. Sáez, R. Rojas-Díaz and Ch. Zhang	159
A 2-D Time-Domain BEM for Dynamic Analysis of Cracked Piezoelectric Solids F. García-Sánchez, Ch. Zhang and A. Sáez	165

Boundary Element Model for Breakup of a Free Conducting Droplet in the Electric Field K. Adamiak, and J.M. Floryan	173
A Time Domain BEM Inverse Method for Identification of Launchers Acoustic Sources S.Alestra, I.Terrasse and B.Troclet	179
Analysis of Plates with Stiffeners by The Boundary Element Method with Condensation of Variables W.W. Wutzow, J.B. de Paiva	185
Boundary Element Method for Magneto-electro-elastic Laminates A. Milazzo, I. Benedetti and C. Orlando	191
BEM Based Solution for an Inverse Problem in MRI by the Tikhonov Regularization Method L.Marin, H.Power, R.W.Bowtell, C.Cobos Sanchez, A.A.Becker, P.Gloverand and I.A.Jones	197
The Green Element Method Applied to Plate Bending A. E. Taigbenu and A. Elvin	203
<i>Extended Abstracts</i>	
A Boundary Element Topology Optimization Problem using the Level Set Method K.Abe, S.Kazama and K.Koro	211
High Performance Preconditioners and Solvers for the Fast Multipole Methods G.Alléon, G.Sylvanda and L. Giraudba	213
Influence of the Soil Profile Randomness on the Seismic Response of Multilayered Soils with a Rigid Inclusion M. Badaoui, M.K. Berrah and A. Mebarki	215
A Fundamental-Solution-Less Boundary Element Method for Exterior Wave Problems C. Song and M.H. Bazyar	217
Performance Analysis of Parallel Krylov Methods for Solving Boundary Integral Equations in Electromagnetism B.Carpentieri	219
Topology Optimization of 2D Potential Problems Using Boundary Elements A.P. Cisilino	221
An Alternative BEM for Fracture Mechanics G. Davi and A. Milazzo	223

Integrated Numerical Approach to Surface Reconstruction from Noisy Data P. Dabnichki and A.Zhivkov	229
A Hybrid Laplace Transform/Finite Difference Boundary Element Method for Diffusion Problems A. J. Davies, D. Crann, S. J. Kane and C-H. Lai	231
A Relation Between the Logarithmic Capacity and the Condition Number of the BEM-Matrices W.Dijkstra and R.M.M.Mattheij	233
An Alternative Approach to Boundary Element Methods via the Fourier Transform F.M.E. Duddeck	235
Fast BEM-FEM Coupling for Magnetostatics A.Frangi, L.Ghezzi and P.Faure-Ragani	237
Computational Modelling of Added mass effect on Hydrodynamic forces P. Gardano and P. Dabnichki	241
Meshless Virtual Boundary Method and its Applications to 2D Elasticity Problems Sun Hai-tao and Wang Yuan-han	243
The Detection of Super-Elliptical Inclusions in Infrared Computerised Axial Tomography N.S.Mera, L.Elliott and D.B.Ingham	245
Thermo-Pro-Elastostatic Green's Functions for Unsaturated Soils E. Jabbari and B. Gatzmiri	247
Application of the Method of the Fundamental Solutions as a Coupling Procedure to Solve Outdoor Sound Propagation S. Hampel, A.P. Cibilino and S. Langer	249
Local Defect Correction for the Boundary Element Method G.Kakuba, R.M.M.Mattheij and M.J.H.Anthonissen	251
The Boundary Element Method for Solving the Laplace Equation in Two-dimensions with Oblique Derivative Boundary Conditions D.Lesnic	253
From Damage to Crack: a B.E. approach V.Mallardo and C.Alessandri	255
Boundary Element Analysis of Three-dimensional Exponentially Graded Isotropic Elastic Solids R. Criado, J.E. Ortiz, V. Mantic, L.J. Gray and F. Paris	257

Numerically Synthesized Displacement and Stress Solutions for a 3D Viscoelastic Half Space Subjected to a Vertical Distributed Surface Stress Loading Using the Radon and Fourier Transforms M. Adolph, E.R Carvalho and E. Mesquita	261
Isoparametric FEM vs. BEM for Elastic Functionally Graded Materials V. Minutolo, E. Ruocco and T. Colella	263
A New High-order Time-kernel BIEM for the Burgers Equation N. Mai-Duy, T. Tran-Cong and R.I. Tanner	267
The Use of the Tangential Differential Operator in the Boundary Integral Equation for Stresses and the Dual Boundary Element Method L. Palermo Jr, L.P.C.P.F Almeida and P.C Gonçalves	269
A MLPG(LBIE) Numerical Method for Solving 2D Incompressible and Nearly Incompressible Elastostatic Problems V. Vavourakis and D. Polyzo	271
A Strain Energy Density Rate Approach to the BEM Analysis of Creep Fracture Problems C. P. Providakis and S.G. Kourtakis	273
An Efficient Green's Function for Acoustic Waveguide Problems J. A. F. Santiago and L. C. Wrobel	275
Green Functions for a Continuously Non-homogeneous Saturated Media S. Seyrafian, B. Gatmiri and A. Nourzad	277
Sedimentation of a Solid Particle Immersed in a Thin Fluid A.Sellier and L.Pasol	279
The Application of a Hybrid Inverse Boundary Element Problem Engine for the Solution of Potential Problems S. Noroozi, P. Sewell and J. Vinney	281
Analyzing Production-Induced Subsidence Using Coupled Displacement Discontinuity and Finite Element Methods Shunde Yin, L. Rothenburg and M.B. Dusseault	283
Analysis of Thick Functionally Graded Plates by Local Integral Equation Method J. Sladek, V. Sladek, Ch. Hellmich and J. Eberhardsteiner	285
Shear Deformation Effect in Second-Order Analysis of Composite Frames Subjected in Variable Axial Loading by BEM E.J. Sapountzakis and V.G. Mokos	287

How EADS uses the Fast Multipole Method to boost its simulation in electromagnetism and acoustics G. Sylvand and I. Terrasse	289
Boundary Element Stress Analysis of Thin, Layered Anisotropic Bodies Y.C. Shiah, Y.C. Lin, and C. L. Tan	291
On The NGF Procedure for LBIE Elastostatic Fracture Mechanics L. S. Miers and J. C. F. Telles	293
Fast Multipole Boundary Element Analysis of Two-Dimensional Elastoplastic Problems P. B. Wang and Z. H. Yao	295
Quasi-static 3D Rolling-Contact R. Abascal and L. Rodríguez-Tembleque	297
High Order Boundary Integral Methods for Maxwell's Equations: Coupling of Micro Local Discretization and Fast Multipole Methods L.Gatard,A.Bachelot and K.Mer-Nkonga,	299
Time Domain 3D Fundamental Solutions for Saturated Porelastic Media with Incompressible Constituents M. Kamalian, B.Gatmiri and M. Jiryaei Sharahi	301
Correction of the Crack Extension Direction in the Dual Boundary Element Method T. Lucht and M.H. Aliabadi	303
Propagation of Seismic P and SV Waves in Alluvial Valleys with Vertical Gradient of Velocity F. Luzón, F. J. Sánchez-Sesma, J. Alfonso Pérez-Ruiz, L. Ramírez-Guzmán and A. Pech	305
Recursive Evaluation of Time Convolution Integrals in the Spectral Boundary Integral Method for Mode III Dynamic Fracture Problems H. Zafarani, As. Noorzad, Kh. Bargi and A. Ansari	307
Amplification Pattern of 2D Semi-sine Shaped Valley Subjected to Vertically Propagating Incident Waves M. Kamalian, B. Gatmiri, A. Sohrabi-bidar and A. Kalaj	309
Infinite Boundary Elements in 2D Elasticity A. Salvadori	311
Index	

Modelling Microfracture in Polycrystalline Materials

G. K. Sfantos^{1,a}, M. H. Aliabadi^{1,b}¹Department of Aeronautics, Faculty of Engineering, Imperial College, University of London,
South Kensington Campus, London SW7 2AZ, U.K.^ag.sfantos@imperial.ac.uk, ^bm.h.aliabadi@imperial.ac.uk**Keywords:** intergranular, microfracture, polycrystalline, grains, boundary element method.**Abstract:** Brittle intergranular microfracture evolution in polycrystalline materials is investigated using a boundary cohesive grain element method. Artificially generated microstructures are considered and a linear cohesive law is employed for modelling multiple microcracking initiation, propagation, branching and arresting, under mixed mode failure conditions, encountering the stochastic effects of the grain location, morphology and orientation. In cases of fully formed microcracks under local compressive loading, a fully frictional non-linear contact analysis is performed to allow for crack surfaces to come into contact, slide or separate.**Introduction**

Grain boundaries of polycrystalline materials, as appears in the majority of engineering metallic alloys (ferrous, nonferrous) and ceramics, are often characterised by the presence of deleterious features and increased surface free energy that makes them more susceptible to aggressive environmental conditions. These conditions often lead to brittle intergranular failure [1,2] and stress-corrosion cracking [3,4], respectively. Modelling fracture initiation and propagation in polycrystalline materials in a microscale range of $10^{-6} \div 10^{-3}m$, is a challenging task since the geometric modelling of fracture is more important, considering the effect of different grain morphology, mechanical behaviour and orientation.

The cohesive surfaces approach inside the Finite Element Method (FEM) remains the most popular approach for modelling initiation, propagation, branching and arresting of multiple intergranular cracks running along grain boundaries in polycrystalline materials. Among the proposed cohesive failure models, the linear law proposed by Camacho and Ortiz [5] and later by Ortiz and Pandolfi [6] for mixed mode failure initiation and propagation, and the potential-based laws proposed by Tvergaard [7] and Xu and Needleman [8] are among the most popular. Various applications of the aforementioned method can be found for dynamic fragmentation [9], dynamic plasticity and spall fracture of polycrystalline alloys [10], microfracture of ceramic composites materials [11], and others. Brittle fracture in polycrystalline materials was also modelled using the extended finite element method [12], where the transition from intergranular to transgranular fracture was also investigated.

On the other hand, the Boundary Element Method (BEM) nowadays provides a powerful tool for solving a wide range of fracture problems [13]. In the special case of modelling the microstructure of a polycrystalline material, due to the boundary only modelling requirement the BEM provides, only the grain boundaries should be modelled. Moreover, in the BEM the field unknowns are directly the displacements and the surface tractions; therefore any cohesive law that couples the tractions and the displacements between cohesive surfaces can be implemented in a more straightforward way.

In this paper a cohesive grain boundary element formulation is presented [14]. Each grain is considered as a single crystal of general anisotropic mechanical behaviour, with random location, morphology and material orientation. The grain boundary interfaces are modelled using a linear cohesive law [6], which allows for initiation and propagation of multiple cracks under mixed mode failure conditions. In cases of completely damaged-cracked grain boundary interfaces, a fully frictional non-linear contact analysis is employed, to encounter problems where the cracks' surfaces come into contact, slide under local compressive pressures or separate.

Microstructure modelling

To date, the Poisson-Voronoi tessellation method is extensively used in the literature for modelling polycrystalline materials in a random manner [1,15]. In the field of grain level material modelling, Voronoi tessellations have been coupled with the FEM [16] to simulate polycrystalline microstructures and used for modelling fragmentation of ceramic microstructures under dynamic loading [9],

grain boundary sliding and separation in nanocrystalline metals [17], creep cavitation damage [18], microdamage and microplasticity under dynamic uniaxial strains [19] and for simulating the effective elastic constants of polycrystalline materials [20]. Fig. 1 illustrates a randomly generated artificial microstructure, using the aforementioned method. Each grain is considered as a single crystal with anisotropic elastic behaviour and specific material orientation, defined randomly by an angle θ off the x geometrical axis, where $0^\circ \leq \theta < 360^\circ$ (non-directional solidification is assumed). Since the present study considers two-dimensional problems, to maintain the random character of the generated microstructure and the stochastic effects of each grain on the overall behaviour of the system, three different cases are considered for each grain in view of which material axis is normal to the plane [9], i.e. *Case 1*: $1 \equiv z$, *Case 2*: $2 \equiv z$ and *Case 3*: $3 \equiv z$ (working plane is assumed the xy).

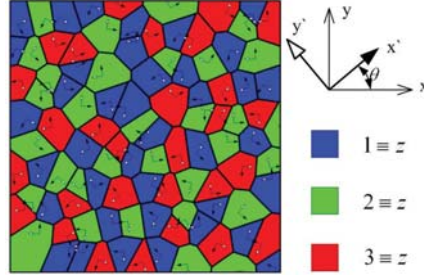


Figure 1: Artificial microstructure with randomly distributed material orientation for each grain.

Considering the microstructure illustrated in Fig. 1, two kinds of grains can be distinguished. The grains that are intersected by the domain boundary \mathfrak{S} and the internal grains that are not intersected by \mathfrak{S} . The difference is that the internal grains have completely unknown boundary conditions while the others have both unknown and prescribed boundary conditions. Each grain is bounded by a boundary S^H , where $H = 1, N_g$ and N_g denotes the number of grains. The boundary of each grain is divided into the contact boundary S_c^H , indicating the contact with a neighbour grain boundary and into the free boundary S_{nc}^H , indicating the grain boundaries that coincide with the domain boundary \mathfrak{S} . Hence for every grain:

$$S^H = S_{nc}^H \cup S_c^H \quad (1)$$

For the internal grains $S_{nc}^H = \emptyset$ and thus $S^H = S_c^H$. Therefore S_{nc}^H exists only on boundary grains resulting to $\bigcup_{H=1}^{N_g} S_{nc}^H = \mathfrak{S}$. For each grain interface, that is a boundary of two neighbour grains, say A & B , tractions equilibrium and displacements compatibility are directly imposed; that is:

$$\tilde{\mathbf{t}}^I = \tilde{\mathbf{t}}_c^A = \tilde{\mathbf{t}}_c^B \quad \& \quad \delta \tilde{\mathbf{u}}^I = \tilde{\mathbf{u}}_c^A + \tilde{\mathbf{u}}_c^B = \mathbf{0} \quad (2)$$

where $\tilde{\mathbf{t}}^I$ and $\delta \tilde{\mathbf{u}}^I$ denote the interface tractions and relative displacements jump and the upper bar ($\tilde{\cdot}$) denotes values in the local coordinate system.

The displacements integral equation [13] for each grain, can now be written as:

$$C_{ij}^H(\mathbf{x}') \tilde{u}_j^H(\mathbf{x}') + \int_{S_{nc}^H} \tilde{T}_{ij}^H(\mathbf{x}', \mathbf{x}) \tilde{u}_j^H(\mathbf{x}) dS_{nc}^H + \int_{S_c^H} \tilde{T}_{ij}^H(\mathbf{x}', \mathbf{x}) \tilde{u}_j^H(\mathbf{x}) dS_c^H = \int_{S_{nc}^H} \tilde{U}_{ij}^H(\mathbf{x}', \mathbf{x}) \tilde{t}_j^H(\mathbf{x}) dS_{nc}^H + \int_{S_c^H} \tilde{U}_{ij}^H(\mathbf{x}', \mathbf{x}) \tilde{t}_j^H(\mathbf{x}) dS_c^H \quad (3)$$

where $\tilde{T}_{ij}^H, \tilde{U}_{ij}^H$ denote the anisotropic fundamental solutions [13] and C_{ij}^H is the so-called free-term. All components in equation (3) refer to the local coordinate system. In the case of internal grains,

the first integral on the left and the right-hand side of equation (3) vanishes since for these grains $S_{nc}^H = \emptyset$.

The boundaries S_c^H and S_{nc}^H of each grain $H = 1, N_g$ are discretized into N_c^H and N_{nc}^H constant sub-parametric elements respectively. The motivation for using constant elements is that all field unknowns, these are interface tractions and displacements discontinuities, are located at the center of these elements and not at the edges; thus problems at triple points (points where three grains meet) are automatically avoided. After the discretization and applying the interface boundary conditions (Eqs. 2), the final system of equations can be written, in matrix form as:

$$\begin{bmatrix} [\mathbf{A}] \\ [\mathbf{0}] \end{bmatrix} \begin{bmatrix} \tilde{\mathbf{x}} \\ \delta \tilde{\mathbf{u}}^I \\ \tilde{\mathbf{t}}^I \end{bmatrix} = \begin{bmatrix} \mathbf{R}\tilde{\mathbf{y}} \\ \mathbf{F} \end{bmatrix} \quad (4)$$

where the submatrices \mathbf{A} and \mathbf{R} are sparsed containing known integrals of the product of the shape functions, the Jacobians and the fundamental fields. Submatrix \mathbf{A} also contains the interface boundary conditions (Eqs. 2). The vectors $\tilde{\mathbf{x}}$ and $\tilde{\mathbf{y}}$ denotes the unknown boundary conditions and the prescribed boundary values along the domain boundary \mathfrak{S} , respectively. The submatrix \mathbf{BC} contains all the interface conditions for the grain facets, corresponding to $\delta \tilde{\mathbf{u}}^I$ and $\tilde{\mathbf{t}}^I$, while the submatrix \mathbf{F} contains the right-hand sides of these interface conditions.

To insure mesh independency and reproducibility of the solution in the present study, the grain boundary elements size was always $\frac{L_{CZ}}{2L_e} > 15$, where L_{CZ} denotes the cohesive zone size at the crack tip, given by [21]:

$$L_{CZ} = \frac{\pi}{2} \left(\frac{K_{IC}}{T_{\max}} \right)^2 \quad (5)$$

where K_{IC} denotes the fracture toughness of the material in Mode I for plane strain conditions and T_{\max} denotes the strength of the cohesive grain boundary pair under pure normal separation [21].

Grain boundaries interface

Cohesive modelling is ideal for interfaces where materials with different properties are met, since it avoids the singular crack fields very close to the crack tip. In the present formulation, the displacements compatibility conditions (2) are directly implemented resulting in the cancellation of any penetration or separation of the grain boundaries interfaces. In this way, difficulties with the initial slope of the bilinear cohesive law extensively used in the FEM are avoided [9,21]. However, to initiate damage in the BEM formulation, considering mixed mode failure criteria, all the information must be gathered by the interface tractions. Therefore an effective traction is introduced $t^{I,eff}$, over all grain boundary interface node pairs $i = 1, M_c : i \in \mathcal{PC}$, where \mathcal{PC} denotes the potential crack zone. Once damage has initiated on a specific grain boundary node pair, say i_o , it is assumed that this pair enters the cohesive zone; that is $i_o \in \mathcal{CZ}$. Following Ortiz and Pandolfi [6], an effective opening displacement is introduced, that accounts for both opening (Mode I) and sliding (ModeII) separation. The effective traction and opening displacement are given as:

$$t^{I,eff} = \left[\langle t_n^I \rangle^2 + \left(\frac{\beta}{\alpha} t_t^I \right)^2 \right]^{\frac{1}{2}} \quad \& \quad d = \left[\left(\frac{\delta u_n^I}{\delta u_n^{I,cr}} \right)^2 + \beta^2 \left(\frac{\delta u_t^I}{\delta u_t^{I,cr}} \right)^2 \right]^{\frac{1}{2}} \quad (6)$$

where t_n^I, t_t^I are the normal and tangential components of the interface traction $\tilde{\mathbf{t}}^I$; β and α assign different weights to the sliding and opening mode and $\langle \cdot \rangle$ denotes the Mc-Cauley bracket defined as $\langle x \rangle = \max \{0, x\}$ $x \in \mathbb{R}$. Damage is initiated once the effective traction, $t^{I,eff}$, exceeds a maximum traction, denoted as T_{\max} ; hence: $t^{I,eff} \geq T_{\max}$. The terms $\delta u_n^I, \delta u_t^I$ denote the normal and tangential

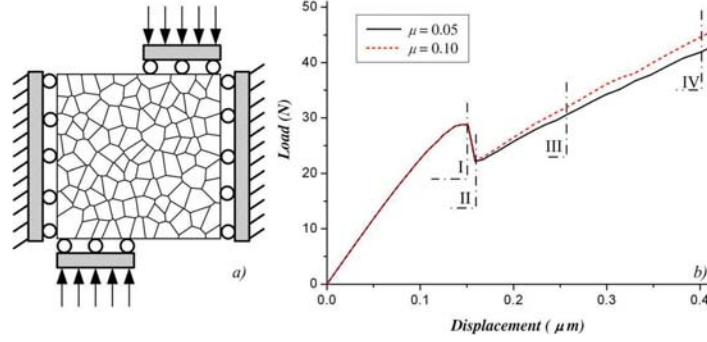


Figure 2: Polycrystalline SiC: a) shear loading conditions, b) simulated load-displacement response , for different friction coefficients μ .

relative displacements of the interface and $\delta u_n^{I,cr}$, $\delta u_t^{I,cr}$ are critical values at which interface failure takes place in the case of pure Mode I and pure Mode II, respectively.

The normal and tangential components of the traction acting on the interface in the fracture process zone are given by:

$$\mathbf{t} = \frac{1-d}{d} \mathbf{K} \delta \mathbf{u} \quad (7)$$

where $\mathbf{K} = \begin{bmatrix} T_{\max}/\delta u_n^{I,cr} & 0 \\ 0 & \alpha T_{\max}/\delta u_t^{I,cr} \end{bmatrix}$ and $\alpha = \beta^2 \frac{\delta u_n^{I,cr}}{\delta u_t^{I,cr}}$. Due to the irreversibility of the interface cohesive law, unloading-reloading in the range $0 \leq d < d^*$ is given by Eq. (7) where d is replaced by d^* , which denotes the last effective opening displacement where unloading took place.

Once a microcrack has formed, that is $d = 1$, the two free surfaces of the microcrack can come into contact, slide or separate. Upon interface failure, the equivalent nodal tangential tractions are computed using the Coulomb's frictional law. Therefore a fully frictional contact analysis is introduced in the proposed formulation to encounter such effects.

It worths noting that all the aforementioned interface laws can be implemented directly in the submatrix \mathbf{BC} of the final system of equations (4). This is a great advantage of the proposed boundary element formulation, since the introduction of the cohesive elements and later of the free microcracks do not affect the size of the final system. This is due to the fact that all the interface laws can be directly implemented as local boundary conditions along the grain boundaries of the microstructure, by coupling the local tractions and relative displacements discontinuities through the interface laws. The system becomes non-linear only when interface elements exist along grain boundaries that are in the loading case (not unloading/reloading), since the interpretation of equation (7) is required. For all other cases the system is fully linear.

Results and Discussion

Polycrystalline SiC under shear loading is considered in the present paper, as Fig. 2(a) illustrates. The components of the stiffness tensor for the hexagonal single crystal SiC [22] are: $C_{11} = 502$, $C_{33} = 565$, $C_{44} = 169$, $C_{12} = 95$, $C_{13} = 96 GPa$. The fracture toughness of the material was considered to be $K_{IC} = 3 MPam^{1/2}$, $T_{\max} = 500 MPa$, $\alpha = \beta = 1$ and plain strain conditions were assumed. The specimen was composed by 100 grains, randomly distributed with random material orientation, of average grain size ASTM $G = 12$ ($\bar{A}^{gr} = 22.3 \mu m^2$, $\bar{d}^{gr} = 4.7 \mu m$ [23]). Displacements control loading was employed throughout this analysis. Figure 2(b) illustrates the resulting load-displacement graph for the different coefficients of internal friction; $\mu = 0.05$ and $\mu = 0.1$. It is obvious that as the coefficient of friction increases the closed crack surfaces slide less due to the frictional forces opposing the sliding and therefore higher load can be carried for the same applied displacements.

Figure 3 illustrates the microcracking evolution as the load increases, for the corresponding phases I-V illustrated in Figure 2(b). Taking a closer look at Figure 3, a slower crack propagation in cases of higher internal friction can be seen, due to the higher frictional forces opposing the sliding and carrying more load. As load continuously increases, crack branching appears that separates completely some grains. The proposed formulation is able to handle such cases, considering the fact that these cracked grains act as free bodies under frictional contacts.

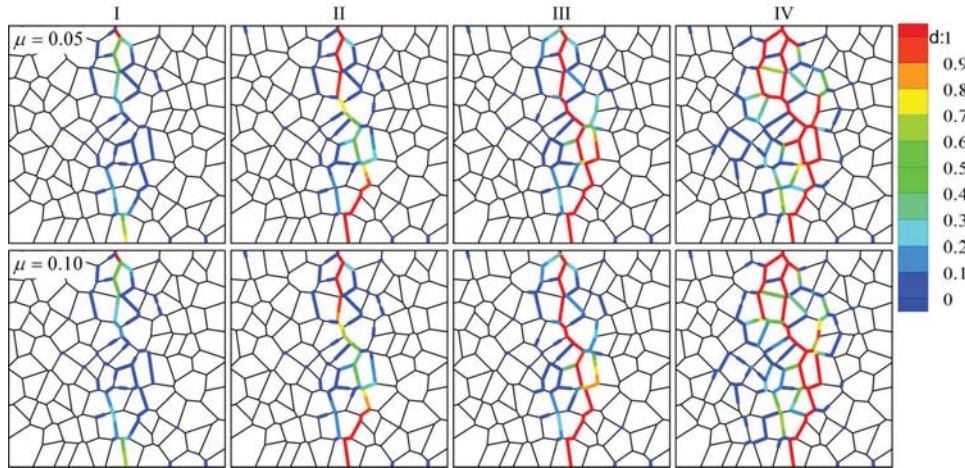


Figure 3: Microcracking evolution under shear loading for various friction coefficients.

Conclusions

In the present paper, brittle intergranular microfracture evolution in polycrystalline SiC was modelled using a cohesive grain boundary element formulation. The analysis demonstrates that the proposed method is capable for modelling initiation and propagation of multiple microcracks under mixed mode failure conditions, encountering the stochastic effects of grain location, morphology and orientation of polycrystalline microstructures. In cases of fully formed cracks, under local compressive loading conditions, a fully frictional contact analysis was employed to encounter cases where crack surfaces come into contact, slide or separate. The computational effort remains low due to the grain boundary only modelling requirement.

References

- [1] A.G. Crocker, P.E.J. Flewitt and G.E. Smith *Int. Materials Reviews*, **50**, 99-124 (2005).
- [2] R.W. Rice *Mechanical properties of ceramics and composites: grain and particle effects*, Marcel Dekker (2000).
- [3] C.J. Jr McMahon *Engineering Fracture Mechanics*, **68**, 773-788 (2001).
- [4] E.P. George, C.T. Liu, H. Lin and D.P. Pope, *Materials Science and Engineering A*, **92-93**, 277-288 (1995).
- [5] G.T. Camacho and M. Ortiz *International Journal of Solids and Structures*, **33**, 2899-2938 (1996).
- [6] M. Ortiz and A. Pandolfi *International Journal for Numerical Methods in Engineering*, **44**, 1267-1282 (1999).
- [7] V. Tvergaard *Materials Science & Engineering A: Structural Materials: Properties, Microstructure and Processing A*, **125**, 203-213 (1990).
- [8] X-P Xu and A. Needleman *International Journal of Fracture*, **74**, 289-324 (1995-1996).
- [9] H.D. Espinosa and P.D. Zavattieri *Mechanics of Materials*, **35**, 333-364 (2003).
- [10] J.D. Clayton *Int. Journal of Solids and Structures*, **42**, 4613-4640 (2005).

- [11] J. Zhai, V. Tomar and M. Zhou *J. of Engng Materials and Techn., Trans. ASME*, **126**, 179-191 (2004).
- [12] N. Sukumar, D.J. Srolovitz, T.J. Baker and J.H. Prevost *Int. J. for Num. Meth. in Engng*, **56**, 2015-2037 (2003).
- [13] M.H. Aliabadi *The Boundary Element Method, Volume 2, Applications in Solids and Structures*, Wiley (2002).
- [14] G.K. Sfantos and M.H. Aliabadi *Int. J. for Num. Meth. in Engng* (2006), submitted.
- [15] A. Okabe, B. Boots, K. Sugihara and S.N. Chiu *Spatial Tessellations: Concepts and Applications of Voronoi Diagrams*, Wiley (2000).
- [16] S. Weyer, A. Fröhlich, H. Riesch-Oppermann, L. Cizelj and M. Kovac *Engineering Fracture Mechanics*, **69**, 945-958 (2002).
- [17] Y.J. Wei and L. Anand *Journal of the Mechanics and Physics of Solids*, **52**, 2587-2616 (2004).
- [18] Y. Liu, Y. Kageyama and S. Murakami, *International Journal of Mechanical Sciences*, **40**, 147-158 (1998).
- [19] K.S. Zhang, D. Zhang, R. Feng and M.S. Wu *Journal of Applied Physics*, **98**, 023505 (2005).
- [20] R.L. Mullen, R. Ballarini, Y. Yin and A.H. Heuer *Acta Materialia*, **45**, 2247-2455 (1997).
- [21] V. Tomar, Z. Jun and Z. Min *Int. J. for Num. Meth. in Engng*, **61**, 1894-1920 (2004).
- [22] R.F.S. Hearmon, in: *Numerical data and functional relationships in science and technology: Group III, Crystal and solid state physics, Vol.1, Elastic, piezoelectric, piezooptic and electrooptic constants of crystals*, edited by K.H. Hellwege, Springer, Berlin (1966).
- [23] ASTM E112-96 (Reapproved 2004): *Standard Test Methods for Determining Average Grain Size* (ASTM International).

BEM Poroplastic Analysis Applied to Reinforced Solids

W.W. Wutzow¹ A.S. Botta¹ W.S. Venturini¹ and A. Benallal²

¹ São Carlos School of Engineering, University of São Paulo, Av. Trabalhador
SãoCarlense, 400, 13566-590 – São Carlos, Brazil, email: venturin@sc.usp.br

² Laboratoire de Mécanique et Technologie, ENS de Cachan/CNRS/Université Paris 6,
61 Avenue du Président Wilson, 94235, Cachan, France, email:
ahmed.benallal@lmt.ens-cachan.fr

Keywords: poroplasticity, reinforcements, non-linear analysis, boundary elements

Abstract. In this article a poroplastic BEM formulation is extended to analyze reinforced multi-region domains. The Biot's theory extended to consider irreversible phenomena, as plasticity, used to formulate the integral equations. Embedded beams inside the domain constitute the reinforcements. The beams are treated separated as independent structural elements or joined together defining a 2D frame totally or partially embedded in the solid. The sub-region technique is adopted to combine different zones enforcing interface force and flux equilibrium and displacement and pore-pressure compatibility. The reinforcement is considered by combining the algebraic system of BEM non-linear equations with the 2D frame FEM algebraic equations. Independent approximations are adopted to represent displacements, rotations and contact forces along the reinforcements. A regularization procedure based on the least square method is adopted to couple the BEM and FEM algebraic equations, avoiding expected force oscillations usually present when the domain and the reinforcement rigidities are too much different. The numerical solution of the non-linear system of equations is based on the Newton-Raphson procedure whereby the loading/unloading conditions are fully taken into account and the consistent tangent operator defined.

Introduction

Analysis of two-phase poroelastic quasi-static systems belongs to a class of problem for which the boundary element approaches (BEM) have already demonstrated to be suitable. The first works BEM approaches to analyze porous media were published in the end of seventies and beginning of eighties [1]. During the last 30 year there were many contributions such as: Cheng [2,3], Park & Banerjee [4] and others. More recently, other works has been developed where the integral representations have been derived by using simple fundamental solutions of the elastic and Laplace problems. This procedure results into simpler formulations, although requiring approximation of domain integrals [5,6]. Following this way, the authors are preparing a more complete non-linear formulation based on the porous media theory based thermodynamic concepts due to Coussy [7] to be published soon [8].

In this paper the formulation given in [8] is extended to include domain reinforced by frame elements approximated by finite elements and joined into the boundary element system of equations by using the least square method to regularize the interface forces. An example is shown to illustrate the accuracy of the proposed technique.

Basic equations

The basic static variables to write extended consolidation theory due to Coussy [7] to take into account the plastic deformation are: the total Cauchy stress, σ_{ij} in the continuum domain and the pore-pressure p in the fluid. The displacement u_i and the strain ε_{ij} in the skeleton and the variation of fluid content per unit volume of porous material ζ are the assumed kinematic variables. Additive forms are assumed to write ε_{ij} and p , i.e., $\varepsilon = \varepsilon^e + \varepsilon^p$ and $\zeta = \zeta^e + \zeta^p$, in which the superscripts e and p are referred to the elastic and plastic parts, respectively.

In order to obtain the integral representation for elastoplastic porous media the following field equations are required: a) equilibrium equation:

$$\sigma_{ij,j} + \bar{b}_i = 0 \quad (1) \text{ and b)}$$

the continuity equation (mass balance) for the fluid:

$$\partial \zeta / \partial t + q_{i,i} = \gamma \quad (2)$$

Assuming the Darcy's law for the isotropic permeability conditions for the fluid part, $q_i = -k(p_{,i} - f_i)$, one obtains:

$$k(p_{,kk} - f_{k,k}) + \gamma - \partial \zeta / \partial t = 0 \quad (3)$$

In the above equations, q_i the specific fluid discharge, \bar{b}_i is the body force vector, k denotes the permeability of the porous media, f_i is the fluid body forces, and γ the fluid source.

$$\rho \psi(\varepsilon^e, \zeta^e, \alpha) = \left[\varepsilon_{ij}^e E_{ijkl}^d \varepsilon_{kl}^e + b^2 M (\varepsilon_{kk}^e)^2 + M (\zeta^e)^2 - 2bM \zeta^e \varepsilon_{kk}^e + \alpha_j h_{jk} \alpha_k \right] / 2 \quad (4)$$

where $E_{ijkl}^d = 2G[\nu(1-2\nu)]\delta_{ij}\delta_{kl} + G(\delta_{ik}\delta_{jl} + \delta_{il}\delta_{jk})$ is the isotropic drained elastic tensor, G is the drained shear modulus, ν is the Poisson's ratio, M is the Biot's modulus, b is the Biot's coefficient of the effective stress and α represents the vector of supplementary internal variables describing the dissipative phenomenon.

Thus, the stress tensor, σ_{ij} , the pore pressure, p , and the thermodynamical forces χ_i are given by:

$$\sigma_{ij} = \rho \frac{\partial \psi}{\partial \varepsilon_{ij}} = E_{ijkl}^d (\varepsilon_{kl} - \varepsilon_{kl}^p) + bp \delta_{ij}; \quad p = \rho \frac{\partial \psi}{\partial \zeta} = M(\zeta - \zeta^p) - b(\varepsilon_{kk} - \varepsilon_{kk}^p); \quad \chi_i = \rho \frac{\partial \psi}{\partial \alpha_i} \quad (5)$$

The internal variable evolutions are governed a plastic potential $F(\sigma_{ij}, p, \chi_i)$, as follows:

$$\dot{\varepsilon}_{ij}^p = \dot{\lambda} F / \partial \sigma_{ij}; \quad \dot{\zeta}^p = \dot{\lambda} F / \partial p; \quad \dot{\alpha}_i = \dot{\lambda} F / \partial \alpha_i \quad (6)$$

where $\dot{\lambda}$ is the plastic multiplier that must satisfy the classical Kuhn-Tucker conditions ($\dot{\lambda} \geq 0$; $f \leq 0$ and $\dot{\lambda} f = 0$), in which $f = f(\sigma_{ij}, p, \chi_i)$ is the adopted loading function.

Integral equations for the poroplastic problem

Let us consider the 2D porous media domain Ω depicted in Fig. 1 constituted by elastoplastic material that, for simplicity but without loss of generality, is reinforced by a single beam element Ω_f .

To apply the Betti's reciprocity theorem to the skeleton part the solid problem one has to consider the effective stress tensor $\sigma_{ij}^{ef} = E_{ijkl}^d (\varepsilon_{kl} - \varepsilon_{kl}^p) = E_{ijkl}^d \varepsilon_{kl} - \sigma_{ij}^p$, in which $\sigma_{ij}^p = E_{ijkl}^d \varepsilon_{kl}^p$ is the plastic stress tensor as follows:

$$\int_{\Omega} (\dot{\sigma}_{ij} + \dot{\sigma}_{ij}^p + bp \dot{\delta}_{ij}) \varepsilon_{ij}^* d\Omega = \int_{\Omega} \sigma_{ij}^* \dot{\varepsilon}_{ij} d\Omega \quad (7)$$

where σ_{ij}^* and ε_{ij}^* are fundamental solutions and the field values are given in rates.

From eq (7) one can derive the displacement and stress integral representations,

$$C_{ik} \dot{u}_k = - \int_{\Gamma} T_{ij}^* \dot{u}_j d\Gamma + \int_{\Gamma} u_{ij}^* \dot{T}_j d\Gamma + \int_{\Omega} \varepsilon_{ikk}^* \dot{p} d\Omega + \int_{\Gamma_f} u_{ik}^* f_k d\Gamma + \int_{\Omega} \varepsilon_{ijk}^* \dot{\sigma}_{jk}^p d\Omega \quad (8)$$

$$\dot{\sigma}_{ij} = - \int_{\Gamma} S_{ijk} \dot{u}_k d\Gamma + \int_{\Gamma} D_{ijk} \dot{T}_k d\Gamma + \int_{\Omega} C_{ijk} \dot{p} d\Omega + \int_{\Gamma_f} D_{ijk} f_k d\Gamma + \int_{\Omega} C_{ijk} \dot{\sigma}_{kl}^p d\Omega + g_{ijk}(\dot{p} \delta_{kl}) + g_{ijk}(\dot{\sigma}_{kl}^p) \quad (9)$$

where u_{ij}^* and T_j^* are fundamental solutions, D_{ijk} , S_{ijk} and C_{ijk} are fundamental solutions, T_j is the boundary tractions, f_k is the embedded beam interface force, while g_{ijk} is the well-known free term given by:

$$g_{ijk}(\mathbf{a}_{kl}) = -[2a_{ij} + (1-4\nu)a_{mm} \delta_{ij}] / 8(1-\nu) \quad (10)$$

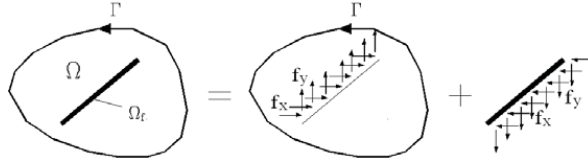


Figure 1. Domain reinforced by single beam; interactive forces f_k acting along the interface Γ_f .

Denoting $q_i^e = -kp_i$ in eq (3) the reciprocity relation can also be used to write

$$\int_{\Omega} q_i^* p_j d\Omega = \int_{\Omega} q_i^e p_j^* d\Omega = \int_{\Omega} (q_i - kf_i) p_j^* d\Omega \quad (11)$$

By performing the relevant integration by parts and using eq (2) the integral equation for the pressure is obtained, as follows:

$$cp = -\int_{\Gamma} pq^* d\Gamma + \int_{\Gamma} qp^* d\Gamma + \int_{\Omega} (-\gamma + \partial\zeta/\partial t)p^* d\Omega - \int_{\Omega} kf_i p_j^* d\Omega \quad (12)$$

where c is the free term of the potential problem.

Algebraic equations

Frame finite element equations. The reinforcement elements are modelled by frame finite elements. The matrix equation to be written to express the equilibrium of the reinforcements is obtained from the Virtual Work Principle,

$$\int_{V_f} \bar{\epsilon}_{ij} \sigma_{ij} dV = \int_{\Gamma_f} \bar{u}_k f_k d\Gamma \quad (13)$$

where σ_{ij} is the beam element stress tensor, f_k gives the interface force components, while the upper bars indicate virtual strains and displacements.

Assuming the beam hypotheses, only the components σ_{11} , normal component in the beam axis direction, and σ_{12} , shear component in the cross-section plane of σ_{ij} are taken into account. Then they are written in terms of three displacement components, two translations and one rotation, which are independently approximated over the beam element using cubic shape functions.

Replacing the approximations in eq (13) and performing the relevant integrals one can obtain the finite element system of algebraic equations in the following format:

$$\mathbf{H}_f \mathbf{u}_f = \mathbf{G}_f \mathbf{f}_f \quad (14)$$

where \mathbf{H}_f and \mathbf{G}_f are the stiffness matrix and the lumped matrix given by,

$$\mathbf{H}^f = \begin{bmatrix} \frac{37GA}{10L} & 0 & \frac{GA}{2} & -\frac{189GA}{40L} & 0 & \frac{57GA}{80} & \frac{27GA}{20L} & 0 & -\frac{3GA}{10} & \frac{13GA}{40L} & 0 & \frac{7GA}{80} \\ 0 & \frac{37EA}{10L} & 0 & 0 & \frac{189EA}{40L} & 0 & 0 & \frac{27EA}{20L} & 0 & 0 & -\frac{13EA}{40L} & 0 \\ \frac{GA}{2} & 0 & \frac{37EI}{10L} + \frac{8GAL}{105} & -\frac{57GA}{80} & 0 & -\frac{189EI}{40L} + \frac{33GAL}{560} & \frac{3GA}{10} & 0 & \frac{27EI}{20L} + \frac{3GAL}{140} & -\frac{7GA}{80} & 0 & -\frac{13EI}{40L} + \frac{19GL}{1680} \\ -\frac{189GA}{40L} & 0 & -\frac{57GA}{80} & \frac{54GA}{5L} & 0 & 0 & -\frac{297GA}{40L} & 0 & \frac{81GA}{80} & \frac{27GA}{20L} & 0 & -\frac{3GA}{10} \\ 0 & -\frac{189EA}{40L} & 0 & 0 & \frac{54EA}{5L} & 0 & 0 & -\frac{297EA}{40L} & 0 & 0 & \frac{27EA}{20L} & 0 \\ \frac{57GA}{80} & 0 & -\frac{189EI}{40L} + \frac{33GAL}{560} & 0 & 0 & \frac{54EI}{5L} + \frac{27GAL}{70} & -\frac{81GA}{80} & 0 & -\frac{27(154EI + GAL^2)}{560L} & \frac{3GA}{10} & 0 & \frac{27EI}{20L} + \frac{3GAL}{140} \\ \frac{27GA}{20L} & 0 & \frac{3GA}{10} & -\frac{297GA}{40L} & 0 & -\frac{81GA}{80} & \frac{54GA}{5L} & 0 & 0 & -\frac{189GA}{40L} & 0 & \frac{57GA}{80} \\ 0 & \frac{27EA}{20L} & 0 & 0 & -\frac{297EA}{40L} & 0 & 0 & \frac{54EA}{5L} & 0 & 0 & -\frac{189EA}{40L} & 0 \\ -\frac{3GA}{10} & 0 & \frac{27EI}{20L} + \frac{3GAL}{140} & \frac{81GA}{80} & 0 & -\frac{27(154EI + GAL^2)}{560L} & 0 & 0 & \frac{54EI}{5L} + \frac{27GAL}{70} & -\frac{57GA}{80} & 0 & -\frac{189EI}{40L} + \frac{33GAL}{560} \\ \frac{13GA}{40L} & 0 & \frac{7GA}{80} & \frac{27GA}{20L} & 0 & \frac{3GA}{10} & -\frac{189GA}{40L} & 0 & \frac{57GA}{80} & \frac{37GA}{10L} & 0 & -\frac{GA}{2} \\ 0 & -\frac{13EA}{40L} & 0 & 0 & \frac{27EA}{20L} & 0 & 0 & 0 & 0 & 0 & \frac{37EA}{10L} & 0 \\ \frac{7GA}{80} & 0 & -\frac{13EI}{40L} + \frac{19GL}{1680} & -\frac{3GA}{10} & 0 & \frac{27EI}{20L} + \frac{3GAL}{140} & \frac{57GA}{80} & 0 & -\frac{189EI}{40L} + \frac{33GAL}{560} & -\frac{GA}{2} & 0 & \frac{37EI}{10L} + \frac{8GAL}{105} \end{bmatrix} \quad (15)$$

$$[G^T]^T = \begin{bmatrix} \frac{13L}{120} & 0 & 0 & \frac{3L}{10} & 0 & 0 & \frac{3L}{40} & 0 & 0 & \frac{L}{60} & 0 & 0 \\ 0 & \frac{13L}{120} & 0 & 0 & \frac{3L}{10} & 0 & 0 & \frac{3L}{40} & 0 & 0 & \frac{L}{60} & 0 \\ \frac{L}{60} & 0 & 0 & \frac{3L}{40} & 0 & 0 & \frac{3L}{10} & 0 & 0 & \frac{13L}{120} & 0 & 0 \\ 0 & \frac{L}{60} & 0 & 0 & \frac{3L}{40} & 0 & 0 & \frac{3L}{10} & 0 & 0 & \frac{13L}{120} & 0 \end{bmatrix}^T \quad (16)$$

where EI , GA , ES , are the bending, shear force and stretching beam cross-section rigidities.

The lumping matrix G_f in eq (16) appears when transforming the nodal forces (standard FEM formulations) into interface traction nodal values. It is obtained by performing the integral of the product of the three-degree displacement approximating functions ϕ and linear shape function ψ (as shown in Fig. 2) assumed to approximate the interface forces, i.e., $G_f = \int_{-f}^f \phi \psi dA$.

BEM algebraic equations for non-linear porous media. Before transforming the integral equations into algebraic ones one has to write the integral representations of displacement, stress and pore-pressure replacing the rate quantities by the corresponding increments. A typical time-step in the time discretization $\Delta t = t_{n+1} - t_n$ has to be defined and then the backward Euler algorithm has to be used to express the time derivatives by: $\dot{x} = \Delta x / \Delta t = (x_{n+1} - x_n) / \Delta t$. Thus, from \dot{x} one can compute $\Delta x = \dot{x} \Delta t = x_{n+1} - x_n$. In the integral representations, the variable given in rates (\dot{u}_k , \dot{T}_k , $\dot{\sigma}_{ij}$, \dot{p} , etc.) will be replaced by their increments (Δu_k , ΔT_k , $\Delta \sigma_{ij}$, Δp , etc.).

To obtain the algebraic equations the domain integrals will be approximate by using triangular cells, while straight elements are used to discretize the boundary and the reinforcements along the boundary or embedded in the domain. Fig. 2 defines node positions and the approximation function adopted for boundary, reinforcement and domain variables. It is important to stress that displacements at internal point do not require approximations. The three-degree polynomial shown in the Fig. 2 is referred to the FEM approximation.

Thus, from the eqs (10) and (11) integral representations for the solid problem one can write the boundary and internal point displacement and internal point stress algebraic representations as follows:

$$H_i^b \Delta U = G_i^b \Delta T + R_b \Delta f + Q_b^p \Delta p + Q_b^\sigma \Delta \sigma^p \quad (17)$$

$$\Delta u = -H_i^b \Delta U + G_i^b \Delta T + R_i \Delta f + Q_i^p \Delta p + Q_i^\sigma \Delta \sigma^p \quad (18)$$

$$\Delta \sigma = -H_o^b \Delta U + G_o^b \Delta T + R_o \Delta f + Q_o^p \Delta p + Q_o^\sigma \Delta \sigma^p \quad (19)$$

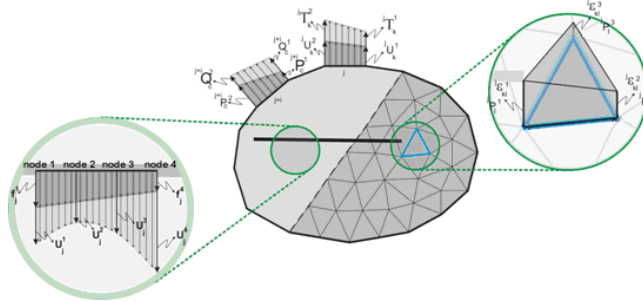


Figure 2. The adopted approximations for boundary, reinforcement interface and domain variables.

where the matrices are the well-known ones obtained by integrating boundary and reinforcement elements and internal cells, while the vectors ΔU , ΔT , Δf , Δp , $\Delta \sigma^p$ and $\Delta \sigma$ represent incremental values of boundary displacements and tractions, interface forces, and domain pore pressures, stress corrector or plastic stresses, and total stresses, respectively. It is important to observe that Q_b^p , Q_i^p and Q_o^p are simple contractions of Q_b^σ , Q_i^σ and Q_o^σ , respectively.

Similarly, the pore pressure integral representation can be transformed into algebraic pore pressure increment representations for boundary and internal points, as follows:

$$H_p^p P = G_p^p Q + Q_p^c \Delta \zeta \quad (20)$$

$$P_i = -H_i^p P + G_i^p Q + Q_i^c \Delta \zeta \quad (21)$$

BEM/FEM coupling. The BEM and FEM systems of algebraic equations derived in the previous sections are now coupled to define the reinforced solid equations. As usual the coupling is made by enforcing traction equilibrium and displacement compatibility at the interface nodes, i.e., $u^f = u$ and $f + f_f = 0$. As a result of choosing different shape functions to approximate interface displacements and interactive forces, we obtained, in eq (18), a number of unknown interface displacements Δu larger than the number of unknown interface forces Δf . To reduce the number of equations to be equal to the number of unknowns one can apply the least square method as it has been made in ref. [9] by multiplying eq (18) by R_f^T transpose matrix R_f^T , as follows:

$$R_f^T \Delta u = -R_f^T H^i \{\Delta U\} + R_f^T G^i \{\Delta T\} + R_f^T R_f^i \{\Delta f\} + R_f^T Q_p^i \{\Delta p\} + R_f^T Q_\sigma^i \{\Delta \sigma^p\} \quad (22)$$

Equations (14), (17) and (22) defines the reinforced solid system of algebraic equations to be solved in terms of boundary and values and interface tractions, as follows:

$$\begin{bmatrix} H & 0 & -R_f \\ H_s & R_f^T & R_s \\ H_f^b & H_f^i & G_f \end{bmatrix} \begin{bmatrix} \Delta U \\ \Delta u \\ \Delta f \end{bmatrix} = \begin{bmatrix} G \\ G_s \\ 0 \end{bmatrix} \Delta T + \begin{bmatrix} Q_p \\ Q_p^T \\ 0 \end{bmatrix} \Delta p + \begin{bmatrix} Q_\sigma \\ Q_\sigma^T \\ 0 \end{bmatrix} \Delta \sigma^p \quad (23)$$

where the sub-matrices of the second line block have been properly renamed and FEM stiffness matrix H_f was split into two sub-matrices: H_f^b and H_f^i .

One can solve eq (23) in terms of boundary and internal unknowns, replace this solution into eq (19), and carry out the required mathematical operations to find the following algebraic system:

$$\Delta N^s + S_p^s \Delta p + \bar{S}_\sigma^s \Delta \varepsilon - S_\sigma^s \Delta \sigma = 0 \quad (24)$$

where ΔN^s is an independent vector depending only on the applied load and boundary conditions, S_p^s , S_σ^s and \bar{S}_σ^s are matrices found after performing the required algebraic operations.

Regarding the pore-pressure problem we can continue in a similar way, solving eq (20) in terms of boundary values and replacing the solution into eq (21) to find after performing the required algebraic operations the following equation

$$N^p + S_i^c (\Delta p^p + B \bullet \Delta \varepsilon) + \bar{S}_i^c \Delta p = 0 \quad (25)$$

where $B = MbI$ with I being the unit matrix.

Non-linear solution.

As for the usual Non-linear BEM technique [10], the equilibrium eqs (24) and (25) can be rewritten as:

$$F^s(\Delta \varepsilon, \Delta p) = \Delta N^s + S_p^s \Delta p + \bar{S}_\sigma^s \Delta \varepsilon - S_\sigma^s \Delta \sigma = 0 \quad (26)$$

$$F^p(\Delta \varepsilon, \Delta p) = N^p + S_i^c (\Delta p^p + B \bullet \Delta \varepsilon) + \bar{S}_i^c \Delta p = 0 \quad (27)$$

Equations (28) and (29) can be solved by applying Newton-Raphson's scheme. An iterative process may be required to achieve the equilibrium. Then, from the iteration i the next try, $(i+1)$, is given by:

$$\Delta \varepsilon_n^{i+1} = \Delta \varepsilon_n^i + \delta \Delta \varepsilon_n^i \quad \Delta p_n^{i+1} = \Delta p_n^i + \delta \Delta p_n^i \quad (28a,b)$$

By linearizing the equilibrium eqs (26) and (27), using the first term of the Taylor expansion, gives:

$$F^s(\Delta \varepsilon_n^i, \Delta p_n^i) + \frac{\partial \{ F^s(\Delta \varepsilon_n^i, \Delta p_n^i) \}}{\partial \{ \Delta \varepsilon_n^i \}} \{ \delta \Delta \varepsilon_n^i \} + \frac{\partial \{ F^s(\Delta \varepsilon_n^i, \Delta p_n^i) \}}{\partial \{ \Delta p_n^i \}} \{ \delta \Delta p_n^i \} \dots = 0 \quad (29a)$$

$$F^p(\Delta \varepsilon_n^i, \Delta p_n^i) + \frac{\partial \{ F^p(\Delta \varepsilon_n^i, \Delta p_n^i) \}}{\partial \{ \Delta \varepsilon_n^i \}} \{ \delta \Delta \varepsilon_n^i \} + \frac{\partial \{ F^p(\Delta \varepsilon_n^i, \Delta p_n^i) \}}{\partial \{ \Delta p_n^i \}} \{ \delta \Delta p_n^i \} \dots = 0 \quad (29b)$$

Example

The example chosen to illustrate the BEM/FEM coupling applied to non-linear porous media is the square poroplastic domain containing a frame inclusion shown in Fig. 3a, in which the geometry of the problem including the embedded inclusion and boundary conditions. The length of the square side is $4.0m$, while the horizontal and vertical structural elements composing the internal frame are $2.0m$ long. The frame elements are assumed elastic with constant cross-section, whose bending (EI) and stretching (EA) rigidities were computed by defining the bar width equal to $0.5m$. The relation between the bar and matrix Young's moduli is 100 , while the Poisson's ratio for the matrix material is $\nu = 0.2$. The porous media is defined by $k = 1.0$, $M = 1.0 \times 10^9$ and the Biot's modulus for the effective stresses $b = 1.0$. The plastic surface and the plastic potential were defined by adopting the following values: $\mu = 1.0$, $\mu^* = 0.3$, $\beta = 1.0$, $\beta^* = 0.3$, $h = 0.0$ and yield stress of the matrix material was assumed to be $\sigma_y = p/25$ in which p is the applied load along the free vertical upper side. The discretization adopted to run the example, shown in Fig. 4b and 4c consists of 64 linear boundary elements, 8 cubic finite elements and 545 triangular cells.

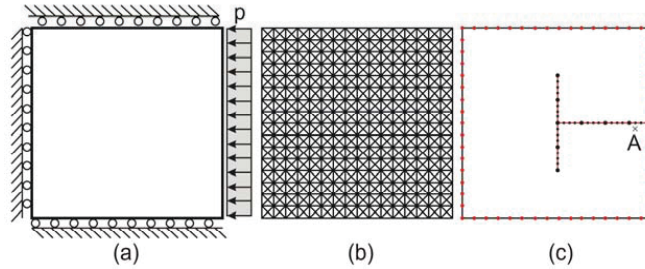


Figure 3. Reinforced domain: a) geometric and boundary conditions; b) internal cells; c) boundary and reinforcement discretizations.

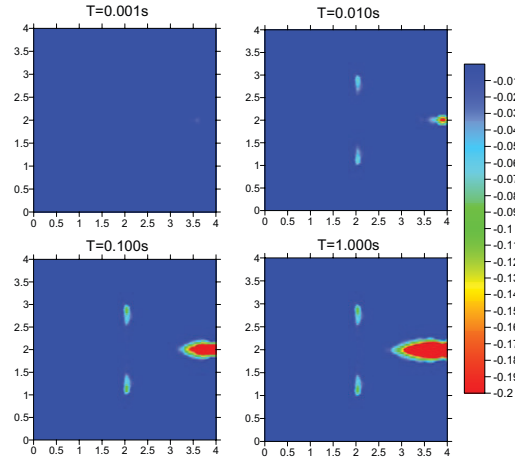


Figure 5. Cumulated plastic multiplier over the domain and the plastic zones.

The total distributed load p is instantaneously applied and the internal variables are computed along time, during which plastic strains and variations of fluid content take place. As we are coupling structural elements with very different rigidities, concentration of stresses will appear near the contacts and particularly in the vicinity of corners what makes this problem very difficult to deal with. As a consequence we have obtained plastic regions concentrated over these particular regions and exhibiting very large plastic values of the strain as well as the variation of

the fluid content. Figure 5 shows the plastic zones appearing close to the interface. The parameter α , the cumulated plastic multiplier, was chosen to identify the evolution of the plastic zones. Figure 6 shows the strain component ε_x distribution along the time. Again one can see the effects of the reinforcement that enforces the strain values in its vicinity to be very small. The normalized values of the total stress component σ_x , the corresponding plastic part, σ_x^p , the cumulated plastic multiplier and pore-pressure given along the time are shown in Fig. 7.

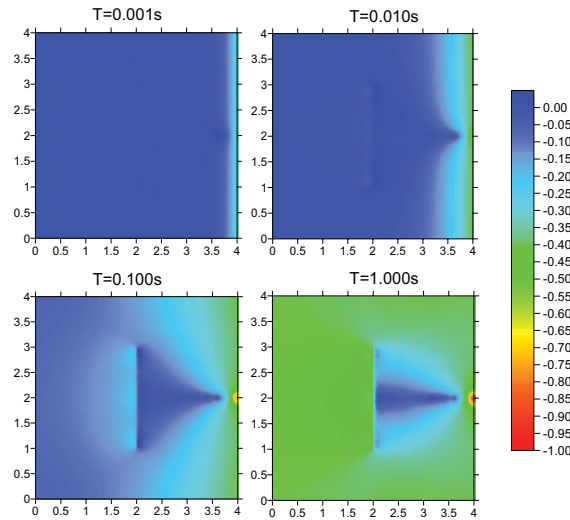


Figure 6. Computed strain ε_x component over the domain.

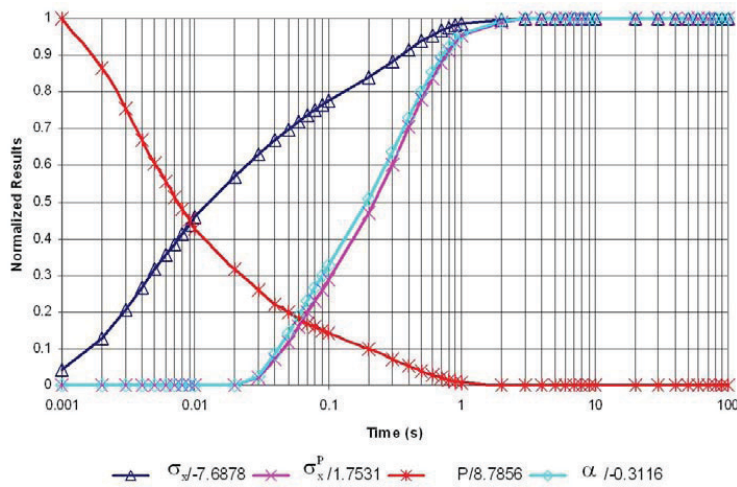


Figure 7. Stress, plastic stress, cumulated plastic multiplier and pore-pressure along the time at point A.

Conclusions

The paper has presented a domain BEM poroplastic formulation applied to reinforced solids. The extended Biot’s theory to include inelastic effects was used. The reinforcements were introduced by coupling the BEM equations with frame FEM equations, therefore introducing stress concentration. The scheme adopted to solve the non-linear system of equations based on the Newton-Raphson process show to be efficient to solve this complex problem.

References

- [1] Cleary, M.P., Fundamental solutions for a fluid-saturated porous solid. *International Journal of solids & structures*, **13**, 785-806 (1977).
- [2] Cheng, A.H.-D. & Liggett, J.A., Boundary integral equation method for linear porous-elasticity with applications to soil consolidation. *International Journal for numerical methods in Engineering*, **20**, 255-278 (1984).
- [3] Cheng, A.H.-D. and Detournay, E., A direct boundary element method for plane poroelasticity. *International Journal for numerical and analytical methods in geomechanics*, **12**, 551-572 (1988).
- [4] Park, K.H. & Banerjee, P.K., Two- and three-dimensional soil consolidation by BEM via particular integral. *Computer Methods Applied Mechanics and Engineering*, **191**, 3233-3255 (2002).
- [5] Cavalcanti M.C. and Telles J.C.F. Biot's consolidation theory – application of BEM with time independent fundamental solutions for poro-elastic saturated media. *Engineering Analysis with Boundary Elements*, **27**, 145-157 (2003).
- [6] Botta, A.S., Venturini, W.S. & Benallal, A., Domain boundary element formulation for poro-elastic solids. In: *Advances in Boundary Element Techniques*, VI, Eds. A.P.S. Selvadurai, C.L. Tan & M.H. Aliabadi, EC Ltd, Uk, 2005.
- [7] Coussy, O., *Mechanics of Porous Continua*. Wiley, New York, 1995.
- [8] Benallal, A., Botta, A.S. & Venturini, W.S., Deformation and consolidation of elastoplastic saturated porous media by the boundary element method. In preparation.
- [9] Botta, A.S. & Venturini, W.S., Reinforced 2d Domain Analysis Using BEM and Regularized BEM/FEM Combination. *Computer Modeling in Engineering and Sciences - CMES*, **8** (1),15-28 (2005).
- [10] Benallal, A., Fudoli, C.A. & Venturini, W.S., An implicit BEM formulation for Gradient plasticity and localization phenomena. *International Journal for Numerical Methods in Engineering*, **53**, 1853-1869 (2002).

Numerical Solution of a Free-Boundary Problem for Percussive Deep Drilling Modeling by BEM

S.E. Mikhailov¹ and I.V.Namestnikova²

^{1,2}Div. of Mathematics, Glasgow Caledonian Univ., Cowcaddens Road, Glasgow, G4 0BA, UK,
s.mikhailov@gcal.ac.uk, i.namestnikova@gcal.ac.uk

Keywords: elasticity, boundary rupture, free-boundary problem, contact problem, iterative algorithm

Abstract. A numerical technique related to a stationary-periodic quasi-static model of rock percussive deep drilling is presented. The rock is modeled by an infinite elastic space with a semi-infinite circular cylindrical bore-hole having a curvilinear bottom. An auxiliary problem of stationary indentation of a rigid drill bit is considered first, where it is assumed that the indentation is produced by a stationary motion of the rupture front on which an appropriate rock strength condition is violated. The bore-hole boundary is not known in advance and consists of four parts: a traction-free non-rupturing part, a contact non-rupturing part, a traction-free part of the rupture front, and a contact part of the rupture front. Thus the problem is formulated as a non-classical non-linear free-boundary contact problem of elasticity. A multi-stage hierarchical iterative algorithm is implemented reducing the problem to a sequence of mixed problems of linear elasticity with known non-smooth infinite boundaries. The Boundary Element Method is used on each iteration step for numerical solution of the direct boundary integral equations of the axially-symmetric linear elastic problems. Then the stationary-periodic percussive drilling problem is reduced to the stationary problem on the rupture stage of the cycle and to the classical contact problem on the reverse and progression-before-rupture stages of the cycle. A numerical example of the stress and displacement distributions, and progression-force diagram are presented.

General Model Description

The drill-bit progression in the percussive drilling is caused by a material rupture under the action of the bit applied at the bore-hole boundary points $x(t)$ moving in time t due to rupture. This boundary loading generates stress $\sigma_{ij}(x, t)$ and strain $\varepsilon_{ij}(x, t)$ tensors at all material points x . Let a material point x has Cartesian coordinates (x_1, x_2, x_3) in the non-deformed state. The radius-vector of the same material point x in a deformed state at a time t is $\tilde{x}(x, t) = x + u(x, t)$, where $u(x, t)$ is the displacement vector. We will use all equations in terms the non-deformed (reference) coordinates x and refer the boundary conditions to the non-deformed boundary surfaces (the Lagrange approach).

Let us consider stationary-periodic percussive drilling of a half-infinite bore-hole, $\Omega_H(t)$, spreading to $x_3 = \infty$ in an infinite elastic space, see Fig. 1. Let the x_3 -axis of the coordinate system coincide with the bore-hole axes, and the drill bit progressive-periodic motion occurs only in the x_3 direction. Let $\Omega(t) = \mathbb{R}^3 \setminus \Omega_H(t)$ be the domain occupied by the material (i.e. the infinite space with a drilled out bore-hole) and $\partial\Omega(t)$ be the bore-hole surface in the non-deformed state, while $\tilde{\Omega}_H(t)$, $\tilde{\Omega}(t) = \mathbb{R}^3 \setminus \tilde{\Omega}_H(t)$ and $\partial\tilde{\Omega}(t)$ be their counterparts in the deformed state. If the rupture front $\partial_F\Omega(t)$ constitutes only a finite part of the boundary $\partial\Omega(t)$, then the borehole is a semi-infinite cylinder with a curvilinear bottom being the rupture front $\partial_F\Omega(t)$. Otherwise, the bore-hole has a monotonously widening shape. If the bit is axially-symmetric then the bore-hole is axially symmetric as well. Let $B(t)$ be the domain occupied by the bit at an instant t , and $\partial B(t)$ be its surface.

To describe the material strength of a point x , we will use an instant strength condition at a point x at an instant t written as

$$\Lambda(\sigma(x, t)) < 1, \quad x \in \Omega(t), \quad (1)$$

where the function $\Lambda(\sigma)$ is associated with the von Mises (see expression (25)), Coulomb–Mohr, Drucker–Prager or another appropriate strength condition. We suppose that the rupture appears in

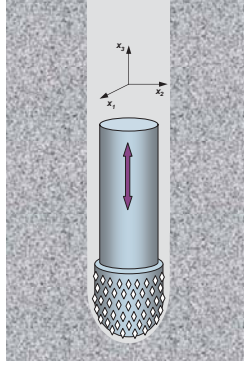


Figure 1: Stationary-periodic percussive drilling model

the form of a rupture front $\partial_F\Omega(t)$, which is a part of the bore-hole boundary $\partial\Omega(t)$. The rupture front equation can be taken as

$$\Lambda(\sigma(x), t) = 1, \quad y \in \partial_F\Omega(t), \quad (2)$$

while no rupture will be inside the material domain Ω and on the rest of the boundary, $\partial_V\Omega(t)$,

$$\Lambda(\sigma(x), t) < 1, \quad y \in \partial_V\Omega(t). \quad (3)$$

The simplest model can be obtained under the following

Model assumptions:

- (i) The deformation gradient is small.
- (ii) The drilled material is linearly elastic and homogeneous, i.e. its elastic moduli $C_{ijkl} = const.$
- (iii) The bit is rigid.
- (iv) The borehole surface is loaded by the bit at the contact surfaces and is free of tractions at all other points.
- (v) Friction between bit and rock can be neglected.
- (vi) The ruptured material, for which strength condition (1) is not satisfied, disappears (is washed away) thus leaving the fresh rupture front (the bottom of the bore-hole) either free of tractions or in contact with the bit bottom.

Under the model assumptions, the non-rupturing boundary part $\partial_V\Omega(t)$ generally consists of the traction-free non-rupturing part, $\partial_{0V}\Omega(t)$, and a contact non-rupturing part, $\partial_{cV}\Omega(t)$. Similarly, the rupturing boundary part $\partial_F\Omega(t)$ generally consists of a traction-free rupturing part, $\partial_{0F}\Omega(t)$, and a contact rupturing part, $\partial_{cF}\Omega(t)$.

Stationary Indentation Model

Let us consider in this section an auxiliary problem of stationary indentation of an infinite elastic space by a rigid indenter (bit) with an instant bit progression $h_3(t)$ (the lowest x_3 coordinate of the bit boundary) in the x_3 direction, where $h_3(t) < 0$ and $h(t) = (0, 0, h_3(t))$ is the indenter progression vector.

Let $\eta_j(x)$ be a unit outward (i.e. directed inward the bore-hole) normal vector to the *non-deformed* boundary $\partial\Omega(t)$. As shown in [1], the non-rupturing boundary part $\partial_V\Omega(t)$ consists of cylindrical pieces with the vertical axis parallel to the progression vector h , i.e.,

$$\eta_3(x) = 0, \quad x \in \partial_V\Omega(t), \quad (4)$$

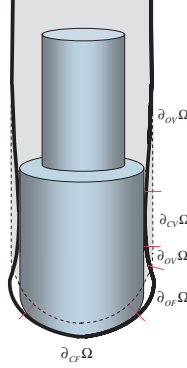


Figure 2: Bore-hole boundary partition

while on the rupturing part of the boundary,

$$\eta_i(x) > 0, \quad x \in \partial_F\Omega(t). \quad (5)$$

The boundary relations (4) and (5) mean that *there is no rupture on the cylindrical part of $\partial\Omega$, any non-cylindrical part of the boundary must be a rupture front and, moreover, there can be no material above the rupture front (in the non-deformed state).*

Summarising conditions (2), (3), (4) and (5), we can formulate them as unilateral nonlinear boundary conditions on the whole boundary,

$$\Lambda(\sigma(x)) - 1 \leq 0, \quad (6)$$

$$\eta_3(x) \geq 0, \quad (7)$$

$$(\Lambda(\sigma(x)) - 1)\eta_3(x) = 0, \quad x \in \partial\Omega. \quad (8)$$

Another set of nonlinear boundary conditions is given by unilateral contact conditions that can be written as a (slightly generalised) Signorini's problem, cf. [2, 3, 4],

$$d'(\tilde{x}) \geq 0, \quad (9)$$

$$\sigma_{ij}(x)\eta_j(x)\eta_i(x) \leq 0, \quad (10)$$

$$d'(\tilde{x})\sigma_{ij}(x)\eta_j(x)\eta_i(x) = 0, \quad x \in \partial\Omega, \quad (11)$$

where

$$d'(\tilde{x}) := (x_i^B(\tilde{x}) - \tilde{x}_i)\eta'_i(x)$$

is a (positive or negative) distance between the point \tilde{x} and the bit boundary ∂B in the $\eta'(x)$ direction; the distance is taken positive, when the point \tilde{x} in the deformed state is outside B and negative, when it is inside; $\eta'_i(x)$ is a unit vector making a sharp (or zero) angle with the external normal $\tilde{\eta}_i(x)$ to $\partial\Omega$ and can be chosen as convenient for particular applications, e.g., as $\eta_i(x)$ or $\tilde{\eta}_i(x)$; and $x_i^B(\tilde{x})$ is a point on ∂B such that the vector $x_i^B(\tilde{x}) - \tilde{x}$ lies along $\eta'_i(x)$.

The strict inequality in (9) and equality in (10) are satisfied at points on the traction-free boundary $\partial_0\Omega$ consisting of $\partial_{0V}\Omega$, $\partial_{0F}\Omega$ and a junction curve between them, while the equality in (9) and strict inequality in (10) are satisfied at points on the contact boundary $\partial_c\Omega$ consisting of $\partial_{cV}\Omega$, $\partial_{cF}\Omega$ and a junction curve between them.

Note that if the displacements $u(x)$ are small, boundary condition (9) can be linearised as

$$u_i(x)\eta'_i(x) \leq d(x), \quad x \in \partial\Omega, \quad (12)$$

where $d(x) = (x_i^B(x) - x_i)\eta'_i(x)$ is a (positive or negative) distance between the point x and the bit boundary ∂B in the $\eta'(x)$ direction in the non-deformed state, and it is known if the contact surface is known and is to be determined otherwise.

To solve the stationary indentation problem, it is sufficient to consider it only for $t = 0$. Thus, taking into account relations (6)-(9) and dropping the argument $t = 0$ for brevity, we arrive at the following non-classical non-linear free boundary problem,

$$\sigma_{ij,j}(x) = 0, \quad \Lambda(\sigma(x)) < 1, \quad x \in \Omega; \quad (13)$$

$$\begin{aligned} \sigma_{ij}(x)\eta_j(x)\xi_i(x) = 0, & \quad \sigma_{ij}(x)\eta_j(x)\zeta_i(x) = 0, & \quad \sigma_{ij}(x)\eta_j(x)\eta_i(x) < 0, \\ \eta_3(x) = 0, & \quad d'(x + u(x)) = 0, & \quad \Lambda(\sigma(x)) < 1, \end{aligned} \quad x \in \partial_{cV}\Omega; \quad (14)$$

$$\begin{aligned} \sigma_{ij}(x)\eta_j(x)\xi_i(x) = 0, & \quad \sigma_{ij}(x)\eta_j(x)\zeta_i(x) = 0, & \quad \sigma_{ij}(x)\eta_j(x)\eta_i(x) < 0, \\ \eta_3(x) > 0, & \quad d'(x + u(x)) = 0, & \quad \Lambda(\sigma(x)) = 1, \end{aligned} \quad x \in \partial_{cF}\Omega; \quad (15)$$

$$\begin{aligned} \sigma_{ij}(x)\eta_j(x) = 0, \\ \eta_3(x) = 0, & \quad d'(x + u(x)) > 0, & \quad \Lambda(\sigma(x)) < 1, \end{aligned} \quad x \in \partial_{0V}\Omega; \quad (16)$$

$$\begin{aligned} \sigma_{ij}(x)\eta_j(x) = 0, \\ \eta_3(x) > 0, & \quad d'(x + u(x)) > 0, & \quad \Lambda(\sigma(x)) = 1, \end{aligned} \quad x \in \partial_{0F}\Omega; \quad (17)$$

$$u_i(x) \rightarrow 0, \quad x \rightarrow \infty. \quad (18)$$

Here

$$\sigma_{ij}(x) = \sigma_{ij}^0 + C_{ijkl}\varepsilon_{kl}(x), \quad \varepsilon_{kl}(x) = (u_{k,l} + u_{l,k})/2, \quad (19)$$

and the constant stiffness tensor C_{ijkl} and the constant *in situ* stress σ_{ij}^0 in the rock without the drill hole are known; $\xi_j(x)$, $\zeta_j(x)$ are unit vectors orthogonal to the normal vector $\eta_j(x)$ and to each other. Condition (18) is understood on almost any straight ray originating from $x = 0$, thus permitting a non-zero limit of the displacements as $x \rightarrow \infty$ parallel to the bore-hole.

All the four boundary parts $\partial_{0V}\Omega$, $\partial_{0F}\Omega$, $\partial_{cV}\Omega$, $\partial_{cF}\Omega$, and consequently $d'(x)$, are generally unknown in this setting, and the corresponding "excessive" boundary equalities and inequalities are provided in (14)-(17) to allow their determination.

After solving problem (13)-(19), the integration of the component $\sigma_{3j}(x)\eta_j(x)$ of the contact traction gives the total axial force $P(t)$ applied to the bit during the progression,

$$\mathcal{P}(t) = \int_{\partial_c\Omega} \sigma_{3j}(x)\eta_j(x) dS(x_c). \quad (20)$$

Stationary-Periodic Indentation Model

To model the stationary-periodic motion of the drill-bit, in addition to the Model assumptions (i)-(vi), let us make the following

Reverse assumption:

- (vii) The rupture does not proceed during the reverse stage of the bit motion, i.e. the borehole boundary consists of the same material points until the load reaches the extremum value during the next cycle.

Due to assumption (vii), the stress and strain return to the same states during the reverse and the following progressive stages of the bit motion up to the rupture restarts. This implies the reverse and the following progressive stages can be considered as some interruptions of the stationary progression process, analyzed in the previous section, and moreover, the interruptions do not influence the material rupture. This means the relation between the total force and the bit progression looks as on Fig. 3, that is the elastic loading stage is followed by the rupture stage followed by the elastic unloading stage. Generally the elastic stages are non-linear on the loading and unloading stages due to the changing

contact surface between the bit and the drilled material, and the force is constant on the rupture stage. The extremum force and strains in the process coincide with those obtained in the stationary indentation analysis in the previous section.

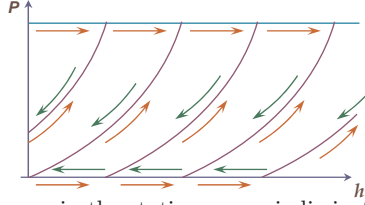


Figure 3: $h - P$ diagram in the stationary-periodic instant rupture model.

Then solution of the stationary indentation problem from the previous section fixes the bore-hole boundary for the reverse stage and gives the extremum values of the contact distribution $p(x, t^{ex})$, whose integral (20) gives the maximum force $\mathcal{P}^{ex} = \mathcal{P}(t^{ex})$ on the bit.

To predict the curvilinear part of the $h - P$ diagram, one has to solve the conforming linearly elastic contact problem with a material boundary $\partial\Omega$ known in the non-deformed state, for both the progressive (before rupture restart) and reverse stages of the cycle (which do coincide). The problem consists of the following equations,

$$\sigma_{ij,j}(x) = 0, \quad x \in \Omega; \quad (21)$$

$$\begin{aligned} \sigma_{ij}(x)\eta_j(x)\xi_i(x) &= 0, & \sigma_{ij}(x)\eta_j(x)\zeta_i(x) &= 0, \\ u_i(x)\eta_i(x) &= d(x, h_3), & \sigma_{ij}(x)\eta_j(x)\eta_i(x) &< 0, \end{aligned} \quad x \in \partial_c\Omega(h_3); \quad (22)$$

$$\sigma_{ij}(x)\eta_j(x) = 0, \quad u_i(x)\eta_i(x) < d(x, h_3), \quad x \in \partial_0\Omega(h_3); \quad (23)$$

$$u_i(x) \rightarrow 0, \quad x \rightarrow \infty. \quad (24)$$

The overall boundary $\partial\Omega$ here is known from the end of the previous progression-rupture stage, although the boundary partition into the traction-free and contact parts is to be determined for each h_3 .

Classical conforming contact problem (21)-(24), (19) can be solved by any of the well known methods, see e.g. [3]. Particularly, one can use the iteration algorithm similar to the one on the progression-rupture stage described above, that is, to choose some reasonable partition of $\partial\Omega$ onto $\partial_0\Omega$ and $\partial_c\Omega$, solve mixed elasticity problem (21)-(24), (19), modify the partition of $\partial\Omega$ to alleviate the violation of inequalities in (22)-(24) and start the next iteration.

Numerics

Numerical Algorithm. Different strategies can be chosen to solve this problem, see e.g. [5], [6, Section 8], [3]. One of the possibilities is the iteration algorithm described below.

The algorithm to solve the stationary indentation (active loading) part of the cycle generally consists of iterations, each solving a non-linear (due to Λ) mixed boundary value problem (13)-(18), (19), where the inequalities are ignored, with some *fixed* boundaries, $\partial_{0V}\Omega$, $\partial_{0F}\Omega$, $\partial_{cV}\Omega$, $\partial_{cF}\Omega$, and consequently $d(x)$. The non-linear (due to Λ) mixed boundary value problem is in turn reduced to a sequence of linear mixed problems solved by BEM or FEM. Then the inequalities in (13)-(17) are checked and the boundaries are changed to alleviate the violation of inequalities, and the next iteration starts. Some more details of the algorithm are given below.

On the first iteration one can reasonably assume that the rupture front coincides with the contact part of the bit, $\partial_c B$, which in turn coincides with the bit bottom, $\partial_b B$, (consisting of the bit surface

points with algebraically smallest x_3 coordinate, over the points with the same (x_1, x_2) coordinates), i.e. $\partial_{cF}\Omega = \partial_c B = \partial_b B$, $\partial_{0F}\Omega = \emptyset$, and there is no contact without rupture, i.e. $\partial_{cV}\Omega = \emptyset$. Those assumptions imply that the borehole free boundary $\partial_V\Omega$ is the semi-infinite cylindrical surface ended by the bit bottom, on the first iteration. Then the algorithm can be presented as a following (inside-out) sequence of imbedded iterative process.

Active loading iteration algorithm:

- (i) Solving mixed problems of linear elasticity for a homogeneous medium with prescribed boundary tractions on $\partial\Omega \setminus \partial_{cV}\Omega$, and zero shear tractions and prescribed normal displacements on $\partial_{cV}\Omega$, by a BEM/FEM code.
- (ii) Iterative algorithm of the form $\sigma_{\eta\eta}^{(i)} = f(\sigma^{(i-1)}, \Lambda^{(i-1)})$ to satisfy the nonlinear boundary condition $\Lambda = 1$ on $\partial_{cF}\Omega$.
- (iii) Iterative alternating algorithm to satisfy the contact conditions and determine the contact rupture-free part of the boundary, $\partial_{cV}\Omega$.
- (iv) Iterative algorithm to determine the non-deformed contact rupture boundary, $\partial_{cF}\Omega$, of the bore-hole $\partial\Omega$, using the known bit boundary and the material boundary displacements from previous iteration step.
- (v) Iterative algorithm to determine the non-contact rupture front boundary, $\partial_{0F}\Omega$, excluding material at the zones where $\Lambda > 1$ and adding material to the non-contact rupture front boundary $\partial_{0F}\Omega$ where $\Lambda < 1$, at the previous iteration step.

After solving the active loading problem, the computation of the unloading part of the percussive drilling cycle includes only one iteration process,

- (vi) Iterative alternating algorithm to solve the conforming contact problem for the unloading and non-active loading stages.

Axially Symmetric BEM. In numerical applications we considered the case of axially-symmetric drilling bit, and the mixed problems of linear elasticity lying in the foundation of our multi-stage iteration algorithm were reduced to corresponding axially symmetric direct boundary integral equation (BIE), see e.g. [7], on a semi-infinite (in the axially-symmetric setting) boundary of the bore-hole. The boundary element method with linear boundary elements has been used for numerical solution of the BIE. The boundary element mesh was uniform on the curvilinear part of the bore-hole and the adjacent vertical part of the boundary of approximately the same length, then the element size increased and the mesh ended with a semi-infinite boundary element. Traction and displacements have been linearly approximated over all boundary elements except the semi-infinite one and the finite-length boundary element adjacent to it, where special approximations based on the known asymptotics of the solution and BIE kernel at infinity have been employed.

Numerical Example. In the numerical example presented in Fig. 4, 5, 6, the Von Mises strength condition was used, giving the following expression for Λ ,

$$\Lambda(\sigma) = \frac{\sqrt{3\sigma_{ij}\sigma_{ij} - \sigma_{ii}\sigma_{jj}}}{\sqrt{2}\sigma_c} = \frac{\sqrt{(\sigma_1 - \sigma_2)^2 + (\sigma_2 - \sigma_3)^2 + (\sigma_3 - \sigma_1)^2}}{\sqrt{2}\sigma_c}, \quad (25)$$

where σ_c is the material strength under uniaxial loading. The Young modulus to strength ratio, $E/\sigma_c = 200$, and the Poisson ration, $\nu = 0.25$, were used in the calculations, cf. [8]. The *in situ* stress has been neglected, $\sigma_{ij}^0 = 0$. The drill-bit with the spherical contact part of a radius R has been analysed.

Fig. 4 shows the numerical $h - P$ diagram, One can see that after about 20% nonlinear growth, the force increases virtually linear with the bit progression. Fig. 5 and Fig. 6 present distributions

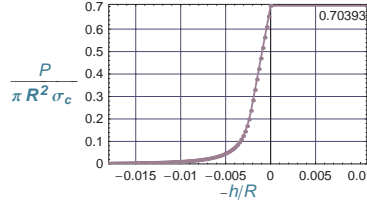


Figure 4: Numerical $h - P$ diagram for spherical bit and linearly elastic rock

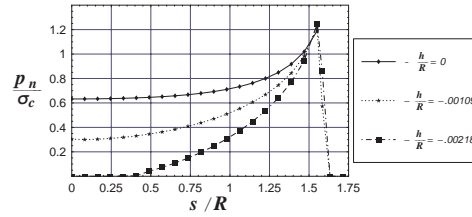


Figure 5: Boundary pressure distribution vs. arc length s

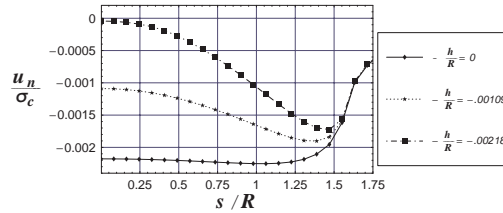


Figure 6: Boundary normal displacement distribution vs. arc length s

of the normal pressure and displacement, respectively, along the bottom of the bore-hole verses the boundary arc-length, at different values of bit progression.

In the performed calculations, we followed the multi-stage iteration algorithm described above, except item (v). This led to material overload ($\Lambda_{max} = 1.04$) on small $0.05R \times 0.07R$ zone adjacent to the upper end of the contact rupture front $\partial_{cF}\Omega$. This overload appearing in internal material points may be disregarded since the effective strength there is higher than in the contact boundary points due to action of the bit inserts on the boundary implicitly taken into account by this way.

Conclusions

A stationary-periodic quasi-static model of percussive drilling and an example of its numerical realisation are presented. The cycles of the bit progression – force diagram consist of three stages: elastic loading, constant-force rupture progression, and elastic unloading parallel to the loading. The problem is split into a stationary free-boundary non-linear problem for the rupture stage of the cycle, and a classical contact problem for the rest of the cycle. A multi-stage iteration algorithm is described reducing the solution to a sequence of linear mixed problems of elasticity. These linear problems can be solved by a general numerical method, e.g. the FEM or the Boundary Integral Equation Method. The latter method has been numerically implemented. As a result, this provides a nonlinear progression-force diagram, which is to be used in the bit dynamic motion prediction.

To take into account the damage zone, propagating ahead of the rupture zone, the rock material can be modeled as an elastic continuum with damage, decreasing the rock stiffness in the damage zone [9]. Extending the iterative algorithm, with an iterative stage taking into account damage, this non-linear problem is also reduced to a sequence of linear elastic problems solvable by the Boundary Integral Equation Method [10].

Acknowledgement. This work was supported by the research grant GR/R85556/01 "Nonlinear Dynamics and Rock Contact Fracture Mechanics in Modelling of Vibration Enhanced Drilling" of the Engineering and Physical Sciences Research Council, UK.

References

- [1] S. E. Mikhailov and I. V. Namestnikova, Quasi-static stationary-periodic model of percussive deep drilling. In: *Proceedings of the 11th International Conf. on Computer Methods and Advances in Geomechanics* (G. Barla and M. Barla, eds.), Vol. 1, 103–109, Bologna: Patron Editore (2005).
- [2] G. Duvaut and J. Lions, *Inequalities in Mechanics and Physics*, Berlin: Springer (1976).
- [3] K. Johnson, *Contact Mechanics*, Cambridge: Cambridge University Press (1985).
- [4] P. Wriggers, *Computational Contact Mechanics*, Chichester: John Wiley (2002).
- [5] C. Eliot and J. Ockendon, *Weak and Variational Methods for Moving Boundary Problems*, Boston-London-Melbourne: Pitman (1982).
- [6] J. Crank, *Free and Moving Boundary Problems*, Oxford (UK): Oxford University Press (1984).
- [7] J. Balaš, J. Sladek and V. Sladek, *Stress Analysis by Boundary Element Methods*, Amsterdam-Oxford-New York-Tokyo: Elsevier (1989).
- [8] R.D.Lama and V.S.Vutukuri, *Hanbook on Mechanical Properties of Rocks – Testing Techniques and Results*, Vol. 2, Clausthal (Germany): Trans Tech Publications (1978).
- [9] S. E. Mikhailov and I. V. Namestnikova, Application of damage mechanics in percussive drilling modelling, in: *11th International Conf. on Fracture*, 8p., Turin, Italy, March 20-25 (2005).
- [10] S. E. Mikhailov, Boundary-domain integro-differential equation of elastic damage mechanics model of stationary drilling, in: *Advances in Boundary Element Techniques VI* (A. P. S. Selvadurai, C. L. Tan and M. H. Aliabadi, eds.), 107–114, Eastligh, UK: EC Ltd. (2005).

Computation of Dynamic Stress Intensity Factors in 2-D Anisotropic Elastic Solids: A Comparison of Two Time-Domain BEM

Stefanie Beyer¹, Michael Wünsche¹, Chuanzeng Zhang², Sohichi Hirose³,
Jan Sladek⁴ and Vladimir Sladek⁴

¹ Department of Civil Engineering, University of Applied Sciences Zittau/Görlitz, D-02763 Zittau, Germany

² Department of Civil Engineering, University of Siegen, D-57068 Siegen, Germany

³ Department of Mechanical and Environmental Informatics, Tokyo Institute of Technology, Tokyo 152-8552, Japan

⁴ Institute of Construction and Architecture, Slovak Academy of Sciences, 84503 Bratislava, Slovakia

Keywords: Anisotropic elastic solids, dynamic stress intensity factors, time-domain BEM, collocation method, Galerkin-method.

Abstract. This paper presents a transient elastodynamic crack analysis in two-dimensional (2-D), homogeneous, anisotropic and linear elastic solids subjected to an impact loading. Two different time-domain boundary element methods (BEM) are developed and compared. A combination of the classical displacement boundary integral equations (BIEs) and the hypersingular traction BIEs is applied. The classical displacement BIEs are used on the external boundary of the cracked solid, while the hypersingular traction BIEs are used on the crack-faces. Time-domain elastodynamic fundamental solutions for anisotropic solids are implemented in both BEM. An explicit time-stepping scheme is developed for solving the time-domain BIEs numerically.

Introduction

Computation of dynamic stress intensity factors (SIFs) is an important task in computational mechanics and linear elastic fracture mechanics under dynamic such as impact loading conditions, since SIFs are the most important crack-tip characterizing parameters in linear elastic fracture mechanics. Beside the very established and well developed finite element method (FEM), the time-domain boundary element method (BEM) provides an efficient and accurate numerical tool for this purpose, at least for homogeneous, isotropic and linear elastic solids. The extension and the application of the time-domain BEM to computing dynamic SIFs in homogeneous, anisotropic and linear elastic solids have been reported, however, only quite recently in literature, since the corresponding dynamic fundamental solutions are much more complicated than that for homogeneous, isotropic and linear elastic solids.

This paper presents a transient dynamic crack analysis in 2-D, homogeneous, anisotropic and linear elastic solids subjected to impact loading conditions. Two different time-domain BEM are developed and compared. In both BEM, a combination of the classical displacement BIEs and the hypersingular traction BIEs is applied. On the external boundary of the cracked solid the classical displacement BIEs are used, while on the crack-faces the hypersingular traction BIEs are used. Time-domain elastodynamic fundamental solutions for anisotropic solids, which have been derived by Wang and Achenbach [1] via Radon transform, are implemented in both BEM. To solve the time-domain BIEs numerically, an explicit time-stepping scheme is developed. Both BEM use a collocation method for temporal discretization, while two different variants are adopted for spatial discretization. In the first variant, a collocation method is applied, while a Galerkin-method is used in the second variant. To describe the local behavior of the crack-opening-displacements (CODs) near the crack-tips properly, a square-root crack-tip shape-function is applied for elements on the crack-faces near the crack-tips, while standard (constant or linear) spatial shape-functions are chosen for all other boundary elements. By using constant and linear temporal shape-functions, time integrations in the system matrices can be carried out analytically. Strongly singular and hypersingular

boundary integrals are treated by special analytical and numerical techniques. The arising line-integrals in the elastodynamic fundamental solutions over a unit-circle are computed numerically. Numerical examples for computing transient elastodynamic SIFs are presented and discussed to verify and compare the accuracy, the efficiency and the stability of the two different time-domain BEM.

Problem statement and time-domain BIEs

Let us consider a homogeneous, anisotropic and linear elastic solid with a crack. In the absence of body forces, the cracked solid satisfies the equations of motion

$$\sigma_{ij,j} = \rho \ddot{u}_i, \quad (1)$$

Hookes law

$$\sigma_{ij} = E_{ijkl} u_{k,l}, \quad (2)$$

the initial conditions

$$u_i(\mathbf{x}, t) = \dot{u}_i(\mathbf{x}, t) = 0 \text{ for } t \leq 0, \quad (3)$$

and the boundary conditions

$$f_i(\mathbf{x}, t) = 0, \quad \mathbf{x} \in \Gamma_c = \Gamma_c^+ + \Gamma_c^-, \quad (4)$$

$$f_i(\mathbf{x}, t) = f_i^*(\mathbf{x}, t), \quad \mathbf{x} \in \Gamma_\sigma, \quad (5)$$

$$u_i(\mathbf{x}, t) = u_i^*(\mathbf{x}, t), \quad \mathbf{x} \in \Gamma_u. \quad (6)$$

Here, u_i , σ_{ij} and $f_i = \sigma_{ij} n_j$ represent the displacement, the stress and the traction components, n_j is the outward normal vector, ρ is the mass density, E_{ijkl} is the elasticity tensor, Γ_c denotes the upper and the lower crack-faces, Γ_σ and Γ_u stand for the external boundaries with prescribed tractions f_i^* and displacements u_i^* , respectively. A comma after a quantity represents spatial derivatives while a dot over a quantity denotes time differentiation. Greek indices take the values 1 and 2, while Latin indices take the values 1, 2 and 3. Also, the conventional summation rule over repeated indices is implied, unless otherwise stated.

On the external boundary of the cracked solid, the classical time-domain displacement BIEs are applied

$$u_j(\mathbf{x}, t) = \int_{\Gamma_\sigma + \Gamma_u} \left(u_{ij}^G * f_i - t_{ij}^G * u_i \right) ds_y + \int_{\Gamma_c} t_{ij}^G * \Delta u_i ds_y, \quad (7)$$

where $u_{ij}^G(\mathbf{x}, \mathbf{y}; t, \tau)$ and $t_{ij}^G(\mathbf{x}, \mathbf{y}; t, \tau)$ are the elastodynamic displacement and traction fundamental solutions, \mathbf{x} and \mathbf{y} represent the observation and the source points, Δu_i are the crack-opening-displacements (CODs) defined by

$$\Delta u_i(\mathbf{x}, t) = u_i(\mathbf{x} \in \Gamma_c^+, t) - u_i(\mathbf{x} \in \Gamma_c^-, t), \quad (8)$$

and $*$ denotes Riemann convolution

$$f * g = \int_0^t f(t-\tau) g(\tau) d\tau. \quad (9)$$

On the crack-faces, the following traction BIEs are used, which can be obtained by substituting eq (7) into Hookes law (2), using the relation $f_i = \sigma_{ij} n_j$, taking the limit process $\mathbf{x} \rightarrow \Gamma_\sigma + \Gamma_u + \Gamma_c$, and considering the boundary conditions (4)-(6),

$$f_j(\mathbf{x}, t) = \int_{\Gamma_\sigma + \Gamma_u} \left(U_{ij}^G * f_i - T_{ij}^G * u_i \right) ds_y + \int_{\Gamma_c} T_{ij}^G * \Delta u_i ds_y. \quad (10)$$

In eq (10), U_{ij}^G and T_{ij}^G are the elastodynamic fundamental solutions higher order, which are defined by

$$U_{ij}^G = -t_{ij}^G = -E_{ijkl} n_p u_{kp,l}^G, \quad T_{ij}^G = -E_{ijkl} n_p t_{kp,l}^G. \quad (11)$$

The elastodynamic fundamental solutions for homogenous, anisotropic and linear elastic solids derived by Wang and Achenbach [3] are implemented in the present analysis. It should be noted here that the elastodynamic fundamental solutions for homogenous, anisotropic and linear elastic solids cannot be given in closed forms in contrast to homogeneous, isotropic and linear elastic solids. In 2-D case, they can be

represented by line-integrals over a unit circle. It should be remarked here that the displacement BIEs (7) have a strong singularity in the sense of Cauchy-principal value integrals, while the tractions BIEs (10) are hypersingular in the sense of Hadamard finite-part integrals.

Numerical solution of the time-domain BIEs

To solve the strongly singular displacement BIEs (7) and the hypersingular traction BIEs (10), two different numerical solution methods are implemented. In both variants, collocation method is applied for the temporal discretization. For the spatial discretization, collocation method is adopted in the first variant while Galerkin-method is implemented in the second variant. At the crack-tips, special ‘‘crack-tip shape-function’’ is applied to describe the local behavior of the CODs near the crack-tips properly. This makes an accurate and direct calculation of the dynamic stress intensity factors from the numerically computed CODs possible. By using constant and linear temporal shape-functions, time integrations can be performed analytically. Strongly singular and hypersingular integrals are computed analytically and numerically by special regularization techniques. Regular integrals and line-integrals over the unit circle in the elastodynamic fundamental solutions are computed numerically by using standard Gaussian quadrature formula. The essential features of the two implemented time-domain BEM are summarized in Table 1 and Table 2.

Variants	Temporal discretization	Spatial discretization	Used fundamental solutions	Crack-tip elements used?
Variant 1 (BEM-C)	Collocation	Collocation	Time-domain fundamental solutions	Yes
Variant 2 (BEM-G)	Collocation	Galerkin	Time-domain fundamental solutions	Yes

Table 1: Two different variants of the time-domain BEM

Discretizations		Variant 1 (BEM-C)	Variant 2 (BEM-G)
Temporal Discretization	Displacements	Linear	Linear
	Tractions	Constant	Constant
Spatial Discretization	Displacements	Constant	Linear
	Tractions	Constant	Linear

Table 2: Temporal and spatial discretizations (except crack-tip elements)

After temporal and spatial discretizations and invoking the initial conditions (3), a system of linear algebraic equations can be obtained as

$$\mathbf{A}^1 \cdot \mathbf{u}^N = \mathbf{B}^1 \cdot \mathbf{f}^N + \sum_{n=1}^{N-1} (\mathbf{B}^{N-n+1} \cdot \mathbf{f}^n - \mathbf{A}^{N-n+1} \cdot \mathbf{u}^n), \quad (12)$$

where \mathbf{A}^n and \mathbf{B}^n are the system matrices, \mathbf{u}^N is the vector containing the boundary displacements and the CODs, and \mathbf{f}^N is the traction vector for the external boundary and the crack-faces. By considering the boundary conditions (4)-(6), equation (12) can be rearranged as

$$\mathbf{x}^N = (\mathbf{C}^1)^{-1} \cdot \left[\mathbf{D}^1 \cdot \mathbf{y}^N + \sum_{n=1}^{N-1} (\mathbf{B}^{N-n+1} \cdot \mathbf{f}^n - \mathbf{A}^{N-n+1} \cdot \mathbf{u}^n) \right], \quad (13)$$

in which \mathbf{x}^N represents the vector with unknown boundary data, while \mathbf{y}^N denotes the vector with known boundary data. Equation (13) is an explicit time-stepping scheme, which can be applied for computing the unknown boundary data including the CODs step by step.

Numerical examples

To compare the two time-domain BEM, several numerical examples are investigated. As first example, we consider a finite crack of length $2a$ in an infinite, homogeneous, anisotropic and linear elastic solid as depicted in Fig. 1. The crack is subjected to an impact tensile crack-face loading of the form $\sigma_{22} = \sigma_0 \cdot H(t)$, where σ_0 is the loading amplitude and $H(t)$ is the Heaviside step function. The crack is discretized by 20 elements and a time-step $c_T \Delta t / a = 0.1$ is selected, where $c_T = \sqrt{C_{66} / \rho}$ is the shear wave velocity. Plane stress condition is assumed in the numerical calculations.

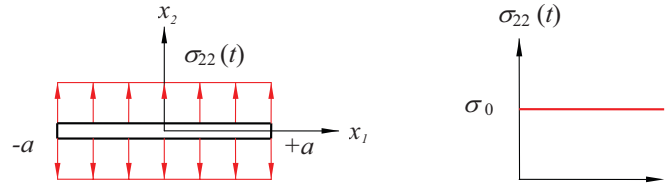


Fig. 1: A finite crack in an infinite anisotropic solid subjected to an impact tensile loading

Graphite-epoxy composite with 65% graphite and 35% epoxy is considered in the example, which has the following material constants

$$C_{ij} = \begin{bmatrix} 95.46 & 28.93 & 4.03 & 0 & 0 & 44.67 \\ & 25.91 & 4.65 & 0 & 0 & 15.56 \\ & & 16.34 & 0 & 0 & 0.54 \\ & & & 4.4 & -1.78 & 0 \\ & sym & & & 6.45 & 0 \\ & & & & & 32.68 \end{bmatrix} \text{ GPa}, \quad \rho = 1600 \text{ kg/m}^3$$

Numerical results for the normalized dynamic stress intensity factors are presented in Fig. 2. A comparison with the numerical results of Zhang *et al.* [2] shows a very good agreement.

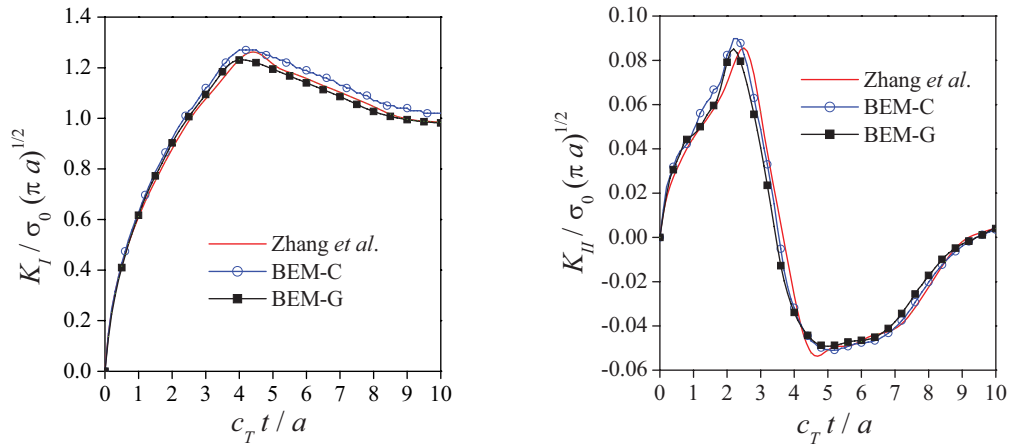


Fig. 2: Normalized dynamic stress intensity factors versus the dimensionless time (tensile loading)

In the second example, we consider the same crack problem and the same material properties as in the first example, but the crack is subjected now to an impact shear crack-face loading of the form $\sigma_{12} = \tau_0 \cdot H(t)$, where τ_0 is the loading amplitude (see Fig. 3). Here again, the crack is discretized by 20

elements and a time-step $c_T \Delta t / a = 0.1$ is chosen. As in the first example, plane stress condition is assumed.

Figure 4 shows the corresponding numerical results for the normalized dynamic stress intensity factors versus the dimensionless time. Here again, the numerical results obtained by the two time-domain BEM agree very well with the numerical results of Zhang *et al.* [2].

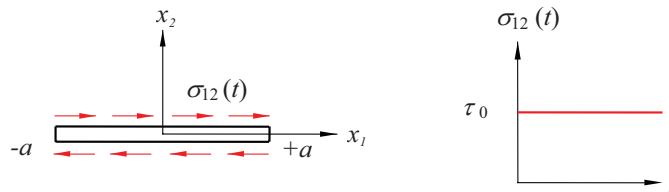


Fig. 3: A finite crack in an infinite anisotropic solid subjected to an impact shear loading

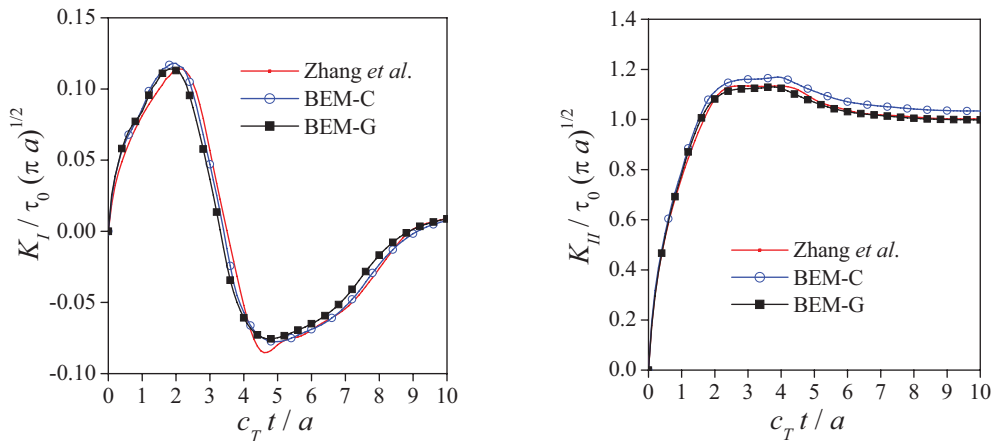


Fig. 4: Normalized dynamic stress intensity factors versus the dimensionless time (shear loading)

In the last example, we consider a finite crack of length $2a$ in a finite rectangular plate as shown in Fig. 5. The plate is subjected to an impact tensile loading of the form $\sigma = \sigma_0 \cdot H(t)$. Numerical calculations are carried out for the following geometrical parameters: $2w=20\text{mm}$, $2h=40\text{mm}$ and $2a=4.8\text{mm}$. Orthotropic material properties and plane stress condition are assumed. In particular, the following material constants are taken: $E_1=118.3\text{GPa}$, $E_2=54.3\text{GPa}$, $G_{12}=8.79\text{GPa}$, $\nu_{12}=0.083$, and $\rho=1900\text{kg/m}^3$.

The external boundary is discretized into elements with a length 0.5mm and the crack is discretized into 10 elements. A time-step $\Delta t = 0.22\mu\text{s}$ is chosen in the numerical calculation. Numerical results for the normalized dynamic stress intensity factor obtained by the two different time-domain BEM are presented in Fig. 5. The overall behavior of the normalized dynamic stress intensity factor predicted by the two different time-domain BEM is very similar. A comparison with the reference solution of Albuquerque *et al.* [3] and the finite element results using ANSYS shows a satisfactory agreement.

Summary

A comparative study of two different time-domain BEM for transient elastodynamic crack analysis in homogeneous, anisotropic and linear elastic solids is presented in this paper. A combination of the classical displacement BIEs and the hypersingular traction BIEs is applied in both BEM. The same temporal discretization is used, while two different variants for the spatial discretization are implemented. The first variant uses collocation method while the second variant applies Galerkin-method for the spatial

discretization. Numerical results for the dynamic stress intensity factors are presented and compared with available reference solutions. To compare the stability behavior and the sensitivity with respect to the used time-steps of the two time-domain BEM, extensive numerical tests have been carried out. From the present analysis, the following conclusions can be drawn:

- **Stability behavior:** Both variants are only conditionally stable. However, variant 1 is more stable than variant 2.
- **Sensitivity with respect to the used time-steps:** Variant 1 is more sensitive than variant 2 against the used time-steps.

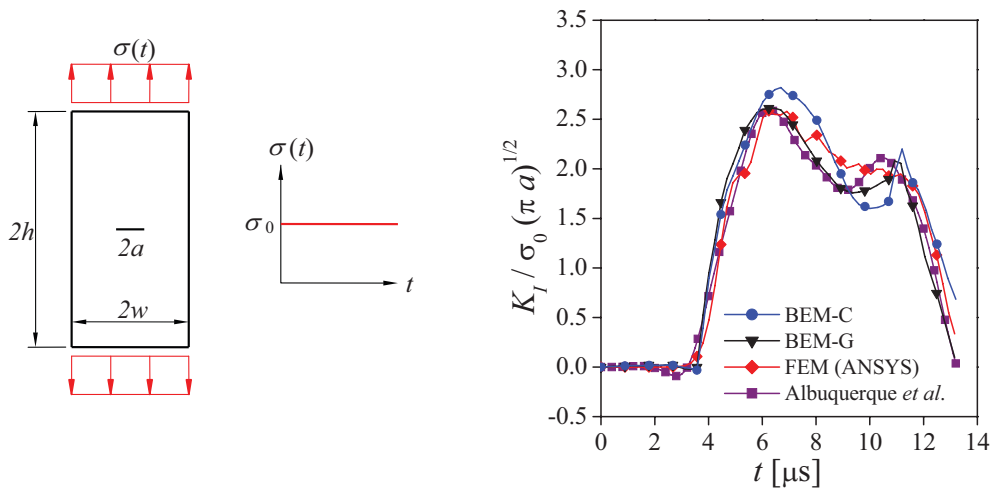


Fig. 5: Normalized dynamic stress intensity factor for a finite crack in a finite orthotropic plate

Acknowledgements

This work is supported by the German Research Foundation (DFG) under the project numbers ZH 15/5-1 and ZH 15/5-2, which is gratefully acknowledged.

References

- [1] C.-Y. Wang and J.D. Achenbach *Geophys. J. Int.*, **118**, 384-392 (1994).
- [2] Ch. Zhang, A. Savaidis and G. Savaidis *Transactions 16th Int. Conf. on Structural Mechanics in Reactor Technology* (Eds: Vernon C. Matzen and C.C. David Tung), Paper # 1981. Center for Nuclear Power Plant Structures, Equipment and Piping, North Carolina State University, USA, 2001.
- [3] E.L. Albuquerque, P. Sollero and M.H. Aliabadi *Int. J. Numer. Meth. Eng.*, **59**, 1187-1205 (2004).

Inverse acoustic scattering by higher-order topological expansion of misfit function

Marc Bonnet¹

¹ Solid Mechanics Laboratory (UMR CNRS 7649),
Ecole Polytechnique, F-91128 Palaiseau cedex, France
bonnet@lms.polytechnique.fr

1 Introduction

The present study is set in the general framework of inverse scattering of scalar (e.g. acoustic) waves. To identify hidden obstacles from external measurements (e.g. overspecified boundary data) associated with the scattering of known incident waves by the unknown object(s), it is customary to invoke iterative algorithms such as gradient-based optimization procedures. The numerical solution of the forward scattering problem associated with an assumed obstacle configuration is often a computationally demanding task. Besides, iterative inversion algorithms are sensitive to the choice of initial “guess” (number of components, initial location, shape and size of obstacle(s)).

This has prompted the definition of preliminary probing techniques, which aim at delineating in a computationally fast way the hidden obstacle(s). Such techniques have been investigated based on either the linear sampling [3], an avenue not pursued here, or the concept of topological sensitivity [2, 4], whereby the sensitivity of a cost functional with respect to the creation of an infinitesimal object of small characteristic radius ε is quantified as a function of the small object location x_s . If $J(\varepsilon, x_s)$ denotes the value achieved by the cost function used for solving the inverse problem when only the infinitesimal obstacle located at x_s is present, then in 3D situations the topological derivative $\mathcal{T}_3(x_s)$ associated with the nucleation of a small obstacle of volume $O(\varepsilon^3)$ and specified shape appears through the expansion

$$J(\varepsilon, x_s) - J(0, x_s) = \varepsilon^3 \mathcal{T}(x_s) + o(\varepsilon^3) \quad (1)$$

(note that the value $J(0, x_s)$ of J for the obstacle-free reference medium does not actually depend on x_s). The present approach is closely related to asymptotic methods developed e.g. in [1].

2 Higher-order expansion of the cost function

In this communication, an extension of the topological derivative is presented, whereby $J(\varepsilon, x_s)$ is expanded further in powers of ε . Specifically, the expansion to order $O(\varepsilon^6)$ for 3D acoustic scattering by a hard obstacle of size ε is presented. The order $O(\varepsilon^6)$ is important for cost functions J of least-squares format because the perturbations of the residuals featured in J are of order $O(\varepsilon^3)$ under the present conditions. In particular, the expansion of J for any *centrally-symmetric* infinitesimal hard obstacle of radius ε centered at x_s is found to have the form

$$J(\varepsilon, x_s) - J(0, x_s) = \varepsilon^3 \mathcal{T}_3(x_s) + \varepsilon^5 \mathcal{T}_5(x_s) + \varepsilon^6 \mathcal{T}_6(x_s) + o(\varepsilon^6) = J(0, x_s) + J_6(\varepsilon, x_s) + o(\varepsilon^6) \quad (2)$$

The previously known topological derivative $\mathcal{T}_3(x_s)$ and the new coefficients $\mathcal{T}_5(x_s)$, $\mathcal{T}_6(x_s)$ have explicit expressions in terms of the acoustic Green’s function associated with the reference acoustic domain and the structure of external boundary conditions. For cases where the Green’s function is not known analytically, setting up $\mathcal{T}_3(x_s)$, $\mathcal{T}_5(x_s)$, $\mathcal{T}_6(x_s)$ entails solving boundary integral equations for (a) the forward and adjoint acoustic fields, and (b) auxiliary solutions generated by acoustic point sources at sampling points x_s , all of which featuring the same governing integral operator, associated with the Helmholtz equation in the reference (i.e. obstacle-free) domain.

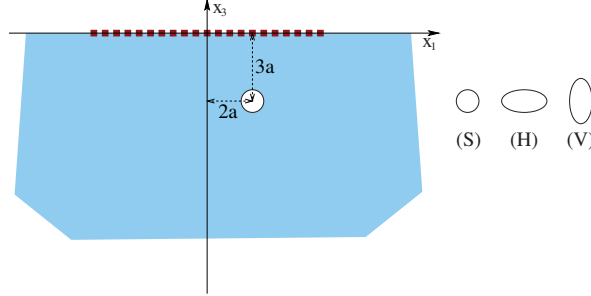


Figure 1: Identification of spherical or ellipsoidal hard scatterer in an acoustic half-space: geometry and notation.

3 A simple approximate global search procedure

Expansions of the form (2) offer the option of minimizing the approximate polynomial expression $J_6(\varepsilon; x_s)$ for sampling points chosen *a priori*. This task is, for each sampling point, simple and computationally very light. Hence, it can conceivably be performed for locations x_s spanning a fine search grid \mathcal{G} , thereby defining an approximate global search procedure over the spatial region sampled by means of \mathcal{G} . The best estimate of the unknown scatterer B^{true} yielded by this procedure is defined by the location $x_s = x^{\text{est}}$ and size $\varepsilon = R^{\text{est}}$ leading to an absolute minimum of $J_6(\varepsilon; x_s)$ over \mathcal{G} . In practice, a partial minimization of $J_6(\varepsilon; x_s)$ w.r.t. ε is performed at each sampling point. Setting $R(x_s)$ and $\hat{J}_6(x_s)$ as

$$R(x_s) = \arg \min_{\varepsilon} J_6(\varepsilon; x_s), \quad \hat{J}_6(x_s) = \min_{\varepsilon} J_6(\varepsilon; x_s) \quad (3)$$

one then defines the best estimate of the unknown scatterer over the sampling grid in terms of its radius R^{est} and center x^{est} by

$$R^{\text{est}} = R(x^{\text{est}}), \quad x^{\text{est}} = \arg \min_{x_s \in \mathcal{G}} \hat{J}_6(x_s), \quad \hat{J}_6^{\text{min}} = \min_{x_s \in \mathcal{G}} \hat{J}_6(x_s) \quad (4)$$

4 Numerical results

To demonstrate the proposed approximate search procedure and thereby demonstrate the usefulness of the $O(\varepsilon^6)$ expansion of $J(\varepsilon; x_s)$, the identification of a hard scatterer embedded in an acoustic medium occupying the half-space $\Omega = \{\xi \mid \xi_3 \leq 0\}$ is considered, as depicted on Fig. 1. A homogeneous Neumann condition is assumed on the surface $x_3 = 0$. Under these conditions, the relevant Green's function is, as mentioned earlier, explicitly known. Three synthetic testing configurations are considered (hereinafter labelled $T^{(1)}$, $T^{(2)}$, $T^{(3)}$), where the square region $-5a \leq \xi_1, \xi_2 \leq 5a$ on the surface $x_3 = 0$ is divided into 5×5 , 10×10 and 20×20 squares, respectively (a being a reference length). Sensors are placed at all vertices x^m ($1 \leq m \leq M$) of the squares thus defined, so that $T^{(1)}$, $T^{(2)}$, $T^{(3)}$ feature $M = 36, 121, 441$ points, respectively. Acoustic point sources of unit magnitude are placed in succession at all centers of the previously defined squares. The scattered field generated by each source is recorded at all sensors, so that $T^{(1)}$, $T^{(2)}$, $T^{(3)}$ support $N = 25, 100, 400$ synthetic experiments, respectively. This is a situation of limited aperture, since data is available only on part of the surface of the half-space. The identification is performed on the basis of the least-squares cost function

$$\mathcal{J}(\Omega^*) = \frac{1}{2} \sum_{q=1}^N \sum_{m=1}^M |u_q^{\text{obs}}(x_m) - u_q^*(x_m)|^2 \quad (5)$$

where u_q^{obs} and u_q^* denote the acoustic fields induced by a unit point source placed at x_q and for the 'true' and 'trial' configurations $\Omega^{\text{true}} = \Omega \setminus B^{\text{true}}$ and $\Omega^* = \Omega \setminus B^*$. The free and adjoint fields associated with the q -th experiment are given (with an overbar indicating complex conjugation) by

$$u_q(\xi) = \mathcal{G}(x_q, \xi) \quad \hat{u}_q(\xi) = \sum_{m=1}^M (\overline{u_q^{\text{obs}}(x_m) - u_q(x_m)}) \mathcal{G}(x_m, \xi) \quad (6)$$

Table 1: Radius estimates R^{est} (best estimate over sampling grid \mathcal{G}) and $R(x^{\text{true}}) = \arg \min_{\epsilon} J_6(\epsilon; x^{\text{true}})$, for testing configurations $T^{(1)}, T^{(2)}, T^{(3)}$ and noise-free synthetic data: sphere (a), horizontally elongated ellipsoid (b) and vertically elongated ellipsoid (c). A distance $\|x_s^{\text{est}} - x^{\text{true}}\| = 0.2a$ was found in all cases.

	$R^{\text{est}}/R^{\text{true}} - 1$			$R(x^{\text{true}})/R^{\text{true}} - 1$			
	$T^{(1)}$	$T^{(2)}$	$T^{(3)}$	$T^{(1)}$	$T^{(2)}$	$T^{(3)}$	
(a)	$ka=0.5$	-4.18e-02	-4.20e-02	-4.20e-02	-2.08e-02	-2.06e-02	-2.05e-02
	$ka=1$	-1.26e-01	-1.26e-01	-1.26e-01	-1.03e-01	-1.03e-01	-1.03e-01
	$ka=2$	-3.33e-01	-3.34e-01	-3.34e-01	-3.02e-01	-3.02e-01	-3.02e-01
	$ka=0.5$	-2.31e-04	9.05e-04	8.89e-04	-1.62e-02	-1.55e-02	-1.56e-02
	$ka=1$	-1.65e-01	-1.65e-01	-1.65e-01	-1.43e-01	-1.43e-01	-1.42e-01
	$ka=2$	-4.22e-01	-4.22e-01	-4.22e-01	-3.93e-01	-3.92e-01	-3.92e-01
	$ka=0.5$	-7.42e-02	-7.51e-02	-7.51e-02	-5.72e-02	-5.78e-02	-5.80e-02
	$ka=1$	-2.04e-01	-2.06e-01	-2.06e-01	-1.91e-01	-1.92e-01	-1.93e-01
	$ka=2$	-4.64e-01	-4.67e-01	-4.67e-01	-4.70e-01	-4.74e-01	-4.76e-01

The approximate global search procedure has been performed on a search grid \mathcal{G} of $51 \times 51 \times 25 = 65025$ regularly spaced sampling points spanning the 3-D box-shaped region defined by $-10a \leq x_1, x_2 \leq 10a, -10a \leq x_3 \leq -0.4a$. The approximate cost function $J_6(\epsilon; x_s)$ with coefficients $\mathcal{T}_3(x_s), \mathcal{T}_5(x_s), \mathcal{T}_6(x_s)$ defined with reference to a small trial spherical scatterer, has been set up for all 65025 sampling points $x_s \in \mathcal{G}$ of the search grid thus defined and using the explicit Green's function.

The scatterer B^{true} to be identified is centered at $x^{\text{true}} = (2a, 1.2a, -3a)$. Three geometries are considered for B^{true} : a sphere (S) of radius $0.5a$, a horizontally elongated ellipsoid (H) with semiaxes $(a, 0.5a, 0.5a)$ and a vertically elongated ellipsoid (V) with semiaxes $(0.5a, 0.5a, a)$. For comparison purposes, a 'true' radius R^{true} is defined for (S) by $R^{\text{true}} = 0.5a$ and for (H) and (V) by $R^{\text{true}} = 2^{-2/3}a$, i.e. as the radius of the sphere having the same volume as (H) or (V). Three wavenumbers $ka = 0.5, 1, 2$ have been considered. Note that $x^{\text{true}} \notin \mathcal{G}$: the sampling points closest to x^{true} are located above and below x^{true} and are separated from x^{true} by a vertical distance $0.2a$.

The obstacle radius estimates R^{est} (best estimate over sampling grid \mathcal{G}) and $R(x^{\text{true}})$ (defined by $R(x^{\text{true}}) = \arg \min_{\epsilon} J_6(\epsilon; x^{\text{true}})$) obtained for the three frequencies considered and using the three testing configurations are compared to R^{true} in table 1, for the three geometries (S), (H) and (V), using exact synthetic data. The lower-frequency case $k = 0.5a$ is seen to yield the most accurate estimation of R^{true} . In all cases, a distance $\|x_s^{\text{est}} - x^{\text{true}}\| = 0.2a$ is found, i.e. the grid point x_s^{est} at which $J_6(\epsilon; x_s)$ achieves its lowest value \hat{J}_6^{min} is one of the two closest to x^{true} featured by the sampling grid \mathcal{G} . Not surprisingly, $R(x^{\text{true}})$ realizes on average a somewhat more accurate estimation of R^{true} than R^{est} . For the cases (H) and (V) where the shapes of the trial and true scatterers do not match, the 'equivalent radius' R^{true} is nevertheless reasonably well estimated, and the location x_s^{est} found is also optimal among the sites allowed by the chosen search grid.

To further illustrate the behaviour of the present approximate search procedure, the radii $R(x_s)$ defined by (3) and the distances $\|x_s - x^{\text{true}}\|$ found at each sampling point $x_s \in \mathcal{G}$ for the true obstacle (S), testing configuration $T^{(3)}$ and $ka = 0.5$, are plotted in figure 2 against the value of $\hat{J}_6(x_s)/|\hat{J}_6^{\text{min}}|$ (only those corresponding to $\hat{J}_6(x_s)/|\hat{J}_6^{\text{min}}| < -0.5$ are shown). The best estimates R^{est} and x_s^{est} correspond to the lowest value achieved on \mathcal{G} by $\hat{J}_6(x_s)$, i.e. to the leftmost point of each graph. These graphs indicate that values of $\hat{J}_6(x_s)$ close to the minimum \hat{J}_6^{min} occur only at grid points near x_s^{est} and yield radii $R(x_s)$ similar to R^{est} . The same behaviour has been observed on corresponding numerical experiments performed for other frequencies and for the true scatterer configurations (H) and (V).

Finally, the effect of data errors on the approximate search procedure has been considered. The (synthetically) measured total field u_q^{obs} in cost function (5) has been replaced with a perturbed version \tilde{u}_q^{obs} such that

$$\text{Re}[\tilde{u}_q^{\text{obs}}(x_m)] = (1 + \eta'_{q,m})\text{Re}[u_q^{\text{obs}}(x_m)], \quad \text{Im}[\tilde{u}_q^{\text{obs}}(x_m)] = (1 + \eta''_{q,m})\text{Im}[u_q^{\text{obs}}(x_m)]$$

where $\eta'_{q,m}$ and $\eta''_{q,m}$ are uniform random numbers with zero mean and 0.05 standard deviation. The measure-

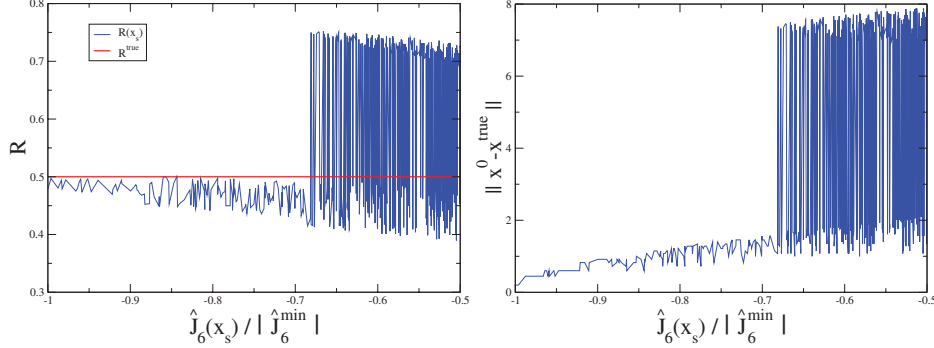


Figure 2: Radius estimates $R(x_s)$ (left) and distances $\|x_s - x^{\text{true}}\|$ (right) for all grid points, ranked according to value of approximate cost function $\hat{J}_6(x_s)$; R^{est} and $\|x^{\text{est}} - x^{\text{true}}\|$ correspond to leftmost point of graphs.

Table 2: Radius estimate R^{est} and distance $\|x_s^{\text{est}} - x^{\text{true}}\|$, for testing configurations $T^{(1)}$, $T^{(2)}$, $T^{(3)}$ and synthetic data with 5% noise on total field: sphere (a), horizontally-elongated ellipsoid (b), vertically-elongated ellipsoid (c).

	$R^{\text{est}}/R^{\text{true}} - 1$			$R(x^{\text{true}})/R^{\text{true}} - 1$			
	$T^{(1)}$	$T^{(2)}$	$T^{(3)}$	$T^{(1)}$	$T^{(2)}$	$T^{(3)}$	
(a)	$ka=0.5$	$-2.67e-01$	$-2.15e-02$	$-3.51e-02$	$4.06e+00$	$4.47e-01$	$4.47e-01$
	$ka=1$	$-1.25e-01$	$-1.17e-01$	$-1.25e-01$	$4.47e-01$	$2.00e-01$	$2.00e-01$
	$ka=2$	$-3.33e-01$	$-3.33e-01$	$-3.33e-01$	$2.00e-01$	$2.00e-01$	$2.00e-01$
	$ka=0.5$	$4.21e-02$	$-4.74e-02$	$-2.65e-03$	$4.47e-01$	$2.00e-01$	$2.00e-01$
	$ka=1$	$-1.47e-01$	$-1.43e-01$	$-1.65e-01$	$2.00e-01$	$2.00e-01$	$2.00e-01$
	$ka=2$	$-4.19e-01$	$-4.23e-01$	$-4.22e-01$	$2.00e-01$	$2.00e-01$	$2.00e-01$
	$ka=0.5$	$-1.10e-01$	$-9.09e-02$	$-7.74e-02$	$4.47e-01$	$2.00e-01$	$2.00e-01$
	$ka=1$	$-1.97e-01$	$-2.08e-01$	$-2.05e-01$	$2.00e-01$	$2.00e-01$	$2.00e-01$
	$ka=2$	$-4.59e-01$	$-4.66e-01$	$-4.68e-01$	$2.00e-01$	$2.00e-01$	$2.00e-01$

ment residuals $u_q^{\text{obs}}(x_m) - u_q^*(x_m)$ being on average of much smaller magnitude than the measured total field, especially at the lower frequency $ka=0.5$, they are severely affected by the above-defined, relatively small, perturbation of the total field. The best estimates R^{est} and x^{est} over the sampling grid \mathcal{G} for true scatterer configurations (S), (H) and (V) have been computed for testing configurations $T^{(1)}$ and $T^{(2)}$ and the same three frequencies as before. The relative error on R^{est} and the distance $\|x_s^{\text{est}} - x^{\text{true}}\|$ resulting from these computations are displayed in table 2. A comparison of these results with those of table 1 obtained with error-free data shows that mildly perturbed values of R^{est} and x^{est} are obtained for $ka=1, 2$, whereas the deterioration of accuracy is much stronger for $ka=0.5$, especially when the coarsest testing configuration $T^{(1)}$ is used.

References

- [1] AMMARI, H., KANG, H. *Reconstruction of small inhomogeneities from boundary measurements*. Lecture Notes in Mathematics 1846. Springer-Verlag (2004).
- [2] BONNET, M., GUZINA, B. B. Sounding of finite solid bodies by way of topological derivative. *Int. J. Num. Meth. in Eng.*, **61**, 2344–2373 (2004).
- [3] COLTON, D., KIRSCH, A. A simple method for solving inverse scattering problems in the resonance region. *Inverse Problems*, **12**, 383–393 (1996).
- [4] GUZINA, B. B., BONNET, M. Topological derivative for the inverse scattering of elastic waves. *Quart. J. Mech. Appl. Math.*, **57**, 161–179 (2004).

Analysis and Optimization of Dynamically Loaded Reinforced Plates by the Coupled Boundary and Finite Element Method

Piotr Fedelinski and Radoslaw Gorski

Silesian University of Technology
Department for Strength of Materials and Computational Mechanics
44-100 Gliwice, Konarskiego 18A, Poland
e-mail: Piotr.Fedelinski@polsl.pl, Radoslaw.Gorski@polsl.pl

Keywords: dynamics, optimization, reinforcement, stiffener, boundary element method, finite element method, coupled methods

Abstract. The aim of the present work is to analyze and optimize plates in plane strain or stress with stiffeners subjected to dynamic loads. The reinforced structures are analyzed using the coupled boundary and finite element method. The plates are modeled using the dual reciprocity boundary element method (DR-BEM) and the stiffeners using the finite element method (FEM). The matrix equations of motion are formulated for the plate and stiffeners. The equations are coupled using conditions of compatibility of displacements and equilibrium of tractions along the interfaces between the plate and stiffeners. The final set of equations of motion is solved step-by-step using the Houbolt direct integration method. The aim of optimization is to find the optimal length and location of stiffeners. The objective functions, which characterize strength and stiffness, depend on displacements or tractions. The optimization problem is solved using an evolutionary method. The results of the dynamic analysis by the proposed method are compared with the solutions computed by the professional finite element code, showing a very good agreement. As the result of optimization, an improvement of dynamic response is obtained, in comparison with an initial design.

Introduction

Structures are reinforced by stiffeners in order to increase strength, stiffness and stability. The stiffened structures are frequently subjected to dynamic loads, and the knowledge of their transient dynamic response has a practical significance. Optimal choice of a number of stiffeners, their properties and locations in the structure decides about the effectiveness of the reinforcement.

An analysis of structures with arbitrary geometries, material properties and boundary conditions requires numerical methods. One of the versatile methods, which is intensively developed in dynamics of solids, is the boundary element method (BEM) [1]. The method has been used in static and dynamic analysis of structures with stiffeners. Salgado and Aliabadi [2,3,4] presented the analysis of statically loaded stiffened panels with cracks. The dual BEM was used for sheets with cracks and analytical equations for stiffeners. Growth of single and multiple cracks in plates with continuously and discretely attached stiffeners were considered. Coda, Venturini [5], Coda, Venturini and Aliabadi [6] showed the coupling of three-dimensional bodies, modeled by the time-domain BEM, with shells, plates and frames, analyzed by the FEM. The proposed method is particularly suitable to analysis of soil-structure interactions. Coda [7] presented a static and dynamic non-linear analysis of reinforced two-dimensional structures. The plates were modeled using the BEM. In the BEM, static fundamental solutions were applied, which allowed the formulation of a mass matrix of a structure. The plates were reinforced by non-linear trusses modeled by the FEM. Leite, Coda and Venturini [8] presented a particular approach for two-dimensional reinforced structures, in which bars were represented by very thin sub-regions. In this method, tractions along the interfaces were eliminated from equations and displacements were assumed to be constant over the bars cross-sections. Leite and Venturini [9] presented an alternative formulation, in which displacements at interfaces were eliminated.

In this work, a static and dynamic analysis and optimization of plates with stiffeners is presented. The plates are modeled by the BEM and the stiffeners by the FEM. The optimization problem is solved by the evolutionary method. The preliminary results of optimization were presented by Gorski and Fedelinski [10,11]. In those works, the stiffeners were attached at boundaries of the plates. In the present work, the reinforcement is in the interior of 2D structures.

Matrix equation for the reinforced plate

Let us consider a two-dimensional, homogenous, isotropic and linear elastic body with the boundary Γ_1 occupying the domain Ω_1 . The body is subjected to dynamic boundary tractions, as shown in Fig.1. If the plate is reinforced by a thin beam, having the domain Ω_2 , the deformed stiffener acts on the plate along the line of attachment. In this case, the interaction tractions are distributed along the interface line Γ_{12} .

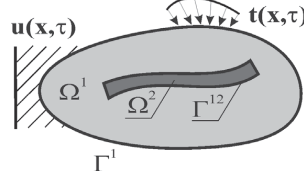


Figure 1: A plate reinforced by a stiffener

Matrix equation for the plate (BEM). The relationship between mechanical fields for the plate is expressed by the boundary integral equations, which are formulated using the dual reciprocity boundary element method (DR-BEM) [1]. In order to obtain the numerical solution, the boundary and the interface where the stiffener is attached, are divided into boundary elements. In the proposed method, quadratic 3-node elements are used. The boundary integral equations are applied for collocation points, which are nodes along the boundary and interface. The variations of boundary coordinates, displacements, tractions and interface tractions are interpolated using quadratic shape functions. The set of resulting algebraic equations can be written in a matrix form [1]

$$\begin{bmatrix} \mathbf{M}^1 & \mathbf{M}^{12} \end{bmatrix} \begin{Bmatrix} \ddot{\mathbf{u}}^1 \\ \ddot{\mathbf{u}}^{12} \end{Bmatrix} + \begin{bmatrix} \mathbf{H}^1 & \mathbf{H}^{12} \end{bmatrix} \begin{Bmatrix} \mathbf{u}^1 \\ \mathbf{u}^{12} \end{Bmatrix} = \begin{bmatrix} \mathbf{G}^1 & \mathbf{G}^{12} \end{bmatrix} \begin{Bmatrix} \mathbf{t}^1 \\ \mathbf{t}^{12} \end{Bmatrix} \quad (1)$$

where: \mathbf{M} is the mass matrix, \mathbf{H} and \mathbf{G} are the BEM coefficient matrices, \mathbf{u} and $\ddot{\mathbf{u}}$ are displacement and acceleration vectors, respectively, and \mathbf{t} is a vector of tractions applied at the boundary or interface. The superscripts denote the matrices, which correspond to the boundary or interface.

Matrix equation for the stiffener (FEM). The stiffener is divided into 2-node straight finite beam elements (3 degrees of freedom in a node). After the discretization and interpolation of displacements, the equation of motion for the stiffener can be written in a matrix form [12]

$$\mathbf{M}^{21} \ddot{\mathbf{u}}^{21} + \mathbf{K}^{21} \mathbf{u}^{21} = \mathbf{T}^{21} \mathbf{t}^{21} \quad (2)$$

where: \mathbf{K} is the FEM stiffness matrix, \mathbf{T} is the matrix, which expresses the relationship between the FE nodal forces and the BE tractions. The matrix \mathbf{T} for a single finite element is given in [8].

Matrix equation for the reinforced plate (coupled BEM/FEM). If the stiffener is bonded to the plate, and the structure is subjected to boundary conditions, the interaction forces between the plate and the stiffener act along the connection line Γ^{12} . The displacement compatibility conditions and the traction equilibrium conditions over the interface Γ^{12} are

$$\mathbf{u}^{12} = \mathbf{u}^{21}; \quad \mathbf{t}^{12} = -\mathbf{t}^{21} \quad (3)$$

If the above conditions are taken into account in Eqs 1 and 2, then the following system of equations for the whole structure is obtained

$$\begin{bmatrix} \mathbf{M}^1 & \mathbf{M}^{12} \\ 0 & \mathbf{M}^{21} \end{bmatrix} \begin{Bmatrix} \ddot{\mathbf{u}}^1 \\ \ddot{\mathbf{u}}^{12} \end{Bmatrix} + \begin{bmatrix} \mathbf{H}^1 & \mathbf{H}^{12} \\ 0 & \mathbf{K}^{21} \end{bmatrix} \begin{Bmatrix} \mathbf{u}^1 \\ \mathbf{u}^{12} \end{Bmatrix} - \begin{bmatrix} \mathbf{G}^{12} \\ \mathbf{T}^{21} \end{bmatrix} \begin{Bmatrix} \mathbf{t}^{12} \\ \mathbf{t}^{12} \end{Bmatrix} = \begin{bmatrix} \mathbf{G}^1 \\ 0 \end{bmatrix} \begin{Bmatrix} \mathbf{t}^1 \\ \mathbf{t}^1 \end{Bmatrix} \quad (4)$$

The above system of equations is rearranged according to the boundary conditions and solved step-by-step by the Houbolt direct integration method giving the unknown displacements and tractions on the external boundary and at the interface in each time step. The method can be used for the static analysis by assuming that the accelerations of all nodes are equal to zero. In a similar way, the method can be implemented for more stiffeners.

Evolutionary method of optimization

The aim of optimization is to find the optimal length and location of stiffeners. The design variables are coordinates of characteristic points of stiffeners. The constraints are imposed on these coordinates. The objective functions, which characterize strength or stiffness, depend on displacements or tractions.

The optimization problem is solved using an evolutionary algorithm (EA) [13]. The algorithm imitates evolutionary processes in nature. Contrary to the gradient methods of optimization, which require sensitivities of objective functions, the evolutionary methods can be simply implemented because they need only the values of objective functions. The probability of obtaining of the global optimal solution is very high, but the methods are very time consuming.

The evolutionary algorithm used in the paper is a modified simple genetic algorithm which uses modified genetic operators and the floating point representation. The computations starts using the initial population of chromosomes randomly generated from the feasible solution domain. Each chromosome, which consists of genes (design variables), is responsible for exactly one potential solution. An objective function plays the role of a fitness function. Chromosomes are estimated using a fitness function and some of them are selected for the next generation. Meanwhile, the genetic operators and the selection are applied. On each gene appropriate constraints are imposed. This procedure is repeated until the optimal solution is reached. The solution of the problem is given by the best chromosome of all generations. Genes of this chromosome define optimal geometry of a structure.

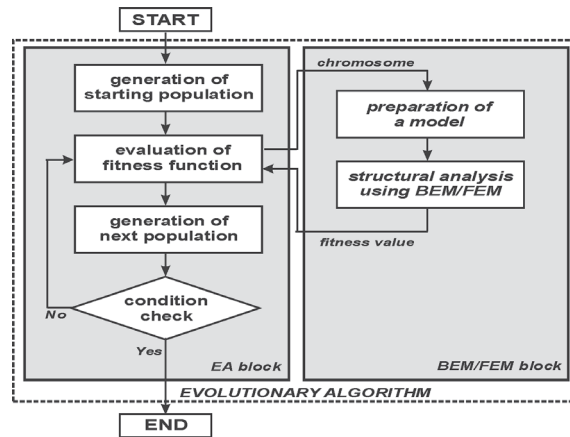


Figure 2: An evolutionary algorithm

The evolutionary program consisting of two main blocks, shown in Fig.2, has been developed. To evaluate a fitness function for each chromosome, first the parameters which specify geometry of a structure are randomly generated. Then the BEM/FEM model is prepared. After that, the BEM/FEM analysis is performed and displacements and tractions on the external boundary and the interfaces are obtained. Finally, a fitness function is evaluated using the boundary displacements or tractions.

Numerical example

The aim of the example is analysis and optimization of a rectangular cantilever plate reinforced by a frame structure and statically or dynamically loaded, as shown in Fig.3a. The frame is composed of 4 straight beams of square cross-section. The length and the height of the plate are $L=10$ cm and $H=5$ cm, respectively. The thickness of the plate is $g=0.25$ cm, the dimensions of cross-section of beams are $2a=0.5$ cm and $b=0.5$ cm. The plate is fixed at its left edge and the uniformly distributed load is applied at the upper edge. For the dynamic problem, the plate is subjected to the sinusoidal load $p(\tau)=p_0 \sin(2\pi\tau/T)$. The amplitude of the load is $p_0=10$ MPa and the period of time is $T=20\pi$ μ s. The material of the plate and the frame is aluminum in plane stress for which the values of mechanical properties are: modulus of elasticity $E=70$ GPa, Poisson's ratio $\nu=0.34$ and density $\rho=2700$ kg/m³. The material is homogeneous, isotropic and linear elastic.

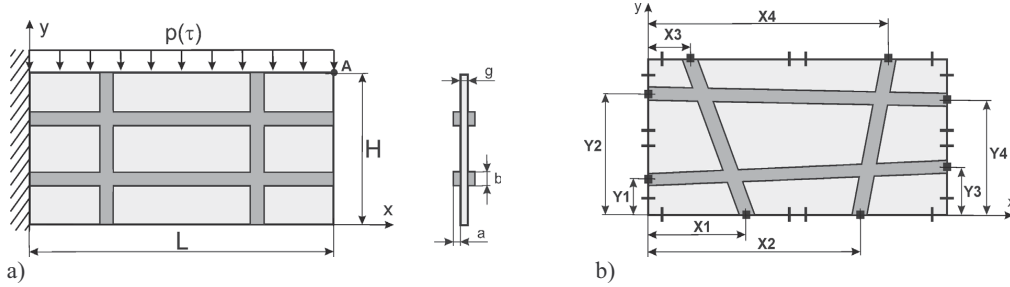


Figure 3: Reinforced cantilever plate: a) dimensions and boundary conditions, b) design variables and constraints

The aim of optimization is to find the location of the reinforcement (the shape of the frame) in order to maximize stiffness of the plate. The following objective function J is minimized

$$J = \max |u^A(\tau)| \quad (5)$$

where $u^A(\tau)$ is the static or dynamic vertical displacement at the considered point A (see Fig.3a).

The number of design variables defining the shape of the frame is 8 (see Fig.3b). They are the coordinates of the ends of all straight beams ($X_i, Y_i, i=1,2,3,4$). The position of each beam is defined by 2 design variables on which the constraints are imposed. The ends of beams can move along the edges of the plate within the constraints, as shown in Fig.3b. The constraints are given in Table 1.

Variable	Constraints [cm]
X1, X3	0.50÷4.75
X2, X4	5.25÷9.50
Y1, Y3	0.50÷2.25
Y2, Y4	2.75÷4.50

Table 1: Constraints on design variables

The total number of boundary and finite elements in the BEM/FEM analysis is 120 and 120, respectively (each horizontal and the vertical beam is discretized into 40 and 20 finite elements, respectively). The total number of quadrilateral plate and beam finite elements in the FEM analysis is 800 and 120, respectively. During the optimization, the number of boundary and finite elements is constant, which simplifies significantly the modification of BE and FE discretization. The time of analysis by the Houbolt method is 600 μs and the time step $\Delta t=2 \mu s$. The number of chromosomes in the population is 50 and the number of generations of the EA is 100.

The accuracy of the developed method is investigated. The analysis is performed for the plate before optimization, called the reference plate, shown in Fig.3a (design variables for this plate are given in Table 2). The dynamic horizontal displacement at the point A, obtained by the present coupled BEM/FEM and by the professional FEM Nastran code, is presented in Fig.4. The agreement of the results is good.

The results of optimization obtained by the evolutionary algorithm, when the criterion of optimization is minimization of the static or maximal dynamic vertical displacement at the point A given by (5), are presented. The values of design variables for the optimal designs, the values of J and its reduction $R=(J_o-J)/J_o \cdot 100\%$ (where: J_o is the u^A for the plate without stiffeners and J is the u^A for the reference or the optimal plate), are shown in Table 2. One can observe that the reduction R for the reference plate and the optimal designs is significant in comparison with the non-stiffened plate. The optimal structures for statics and dynamics are shown in Fig.5a and Fig.5b. It can be seen that in the present example of optimization, most of design variables are active, both for the static and dynamic load.

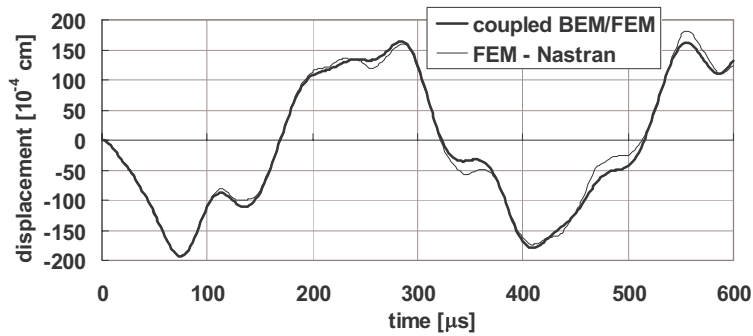


Figure 4: Displacement at the point A

Loading	Plate	Design variables [cm]								J [10^4 cm]	R [%]
		X1	Y1	X2	Y2	X3	Y3	X4	Y4		
static	non-stiffened	-								885	-
	reference	2.50	1.50	7.50	3.50	2.50	1.50	7.50	3.50	793	10.3
	optimal	4.75	0.50	7.05	4.50	0.50	1.10	9.50	4.50	487	45.0
dynamic	non-stiffened	-								430	-
	reference	2.50	1.50	7.50	3.50	2.50	1.50	7.50	3.50	193	55.2
	optimal	2.71	0.50	9.50	4.50	4.75	2.25	9.50	4.50	148	65.6

Table 2: Values of design variables, J and R

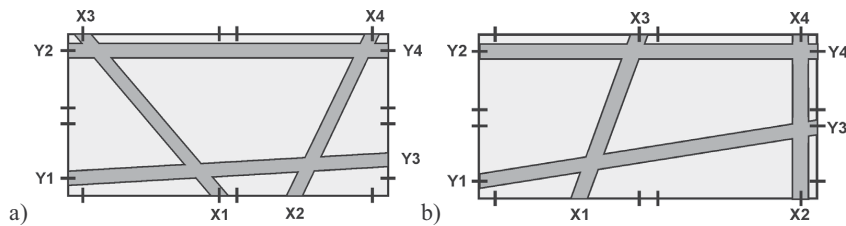


Figure 5: Optimal structures: a) statics, b) dynamics

The dynamic vertical displacements at the point A for the non-stiffened, the reference and the optimal plate are presented in Fig.6. An improvement of dynamic response of the optimal plate in comparison with the non-stiffened and the reference one can be observed.

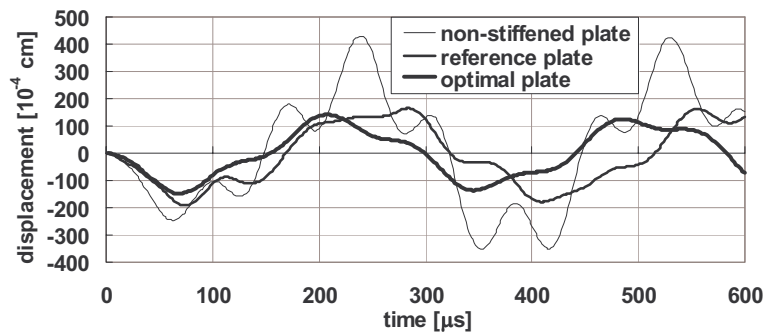


Figure 6: Displacement at the point A

Conclusions

In the paper, the formulation and application of the coupled boundary and finite element method to static and dynamic analysis of two-dimensional reinforced structures is presented. The problem of the optimal reinforcement, which gives the highest strength or stiffness, is solved using the evolutionary method. The proposed method requires only discretization of boundaries of the plates and stiffeners. The reduced discretization simplifies modifications of the reinforcement, which is necessary during the optimization process. The results of dynamic analysis are in a very good agreement with the finite element solutions. The evolutionary method can be simple implemented because it needs only the values of objective functions. The probability of obtaining of the global optimal solution is very high, but the method is very time consuming. An improvement of dynamic response is obtained, as the result of optimization, in comparison with the initial design and the structures without reinforcement. The effectiveness of optimization depends on the problem.

References

- [1] J. Dominguez, *Boundary elements in dynamics*, Computational Mechanics Publications, Southampton-Boston, Elsevier Applied Science, London-New York (1993).
- [2] N.K. Salgado, *Boundary element methods for damage tolerance design of aircraft structures*, Topics in Engineering, Computational Mechanics Publications, Southampton-Boston, **33** (1998).
- [3] N.K. Salgado and M.H. Aliabadi, The application of the dual boundary element method to the analysis of cracked stiffened panels, *Engineering Fracture Mechanics*, **54**, 91-105 (1996).
- [4] N.K. Salgado and M.H. Aliabadi, An object oriented system for damage tolerance design of stiffened panels, *Engineering Analysis with Boundary Elements*, **23**, 21-34 (1999).
- [5] H.B. Coda and W.S. Venturini, On the coupling of 3D BEM and FEM frame model applied to elastodynamic analysis, *International Journal of Solids and Structures*, **36**, 4789-4804 (1999).
- [6] H.B. Coda, W.S. Venturini and M.H. Aliabadi, A general 3D BEM/FEM coupling applied to elastodynamic continua/frame structures interaction analysis, *International Journal for Numerical Methods in Engineering*, **46**, 695-712 (1999).
- [7] H.B. Coda, Dynamic and static non-linear analysis of reinforced media: a BEM/FEM coupling approach, *Computers and Structures*, **79**, 2751-2765 (2001).
- [8] L.G.S. Leite, H.B. Coda and W.S. Venturini, Two-dimensional solids reinforced by thin bars using the boundary element method, *Engineering Analysis with Boundary Elements*, **27**, 193-201 (2003).
- [9] L.G.S. Leite and W.S. Venturini, Boundary element formulation for 2D solids with stiff and soft thin inclusions, *Engineering Analysis with Boundary Elements*, **29**, 257-267 (2005).
- [10] R. Gorski and P. Fedelinski, Optimization of stiffened plates by the coupled BEM/FEM and the evolutionary algorithm, In: *Proceedings of the 6th World Congress on Computational Mechanics in conjunction with the 2nd Asian-Pacific Congress on Computational Mechanics*, Beijing, China, Abstract, Vol. II. Tsinghua University Press, Beijing, Springer-Verlag, Z.H. Yao, M.W. Yuan and W.X. Zhong (eds), 448 (CD-ROM Proceedings - 7 pages) (2004).
- [11] R. Gorski and P. Fedelinski, Evolutionary shape optimization of plates with reinforcements, In: *Proceeding of the Third MIT Conference on Computational Fluid and Solid Mechanics*, Cambridge, USA, Elsevier, Amsterdam, The Netherlands, K.J. Bathe (ed.), 239-242 (2005).
- [12] O.C. Zienkiewicz and R.L. Taylor, *The finite element method. Vol. 1: The basis*, Butterworth-Heinemann, Oxford (2000).
- [13] Z. Michalewicz, *Genetic algorithms + data structures = evolution programs*, Springer-Verlag, Berlin (1996).

Local buckling of thin walled structures by BEM

P.M. Baiz and M.H. Aliabadi

Department of Aeronautical Engineering, Imperial College London
South Kensington campus, London SW7 2AZ

Keywords: Buckling, Multi-region BEM, Shear Deformable Theory.

Abstract. In this paper a boundary element formulation for local buckling analysis of assembled thin walled structures is presented. The assembled structure is divided into several regions, and equilibrium and compatibility equations along the interface edges are imposed. In each region, the formulation is formed by coupling boundary element formulation of shear deformable plate bending and two dimensional plane stress elasticity. The distribution of membrane stresses are obtained from the pre buckling state, therefore the resulting system of equations is presented as a standard eigenvalue problem, from which critical load factors and buckling modes can be obtained in a single procedure. Domain integral appearing in the formulation are transformed into equivalent boundary integrals by the dual reciprocity method. Several numerical examples are presented to demonstrate the capabilities of the proposed method.

Introduction. When the internal membrane state created by the external loading is compressive in thin walled members, it is most likely that the structure will fail due to stability problems. Instability in plate and shell assemblies can be studied from different perspectives depending on if global, local or interactive buckling affects the behaviour of the structure. The main difference between global and local buckling is in the assumption that in local instability the global axis of the member remains straight. There is a considerable amount of works on the stability problem of thin walled structures by numerical methods such as; finite element method (FEM) [4], finite strip method (which is basically a special form of FEM) [10], transfer matrix method [9], among others. Bedair presents an extensive review on some of these techniques [5], with special emphasis on stiffened panels. The Boundary Element Method (BEM) is a well established numerical technique in structural mechanics [1], and in recent years has shown its capabilities for stability modelling of plate structures. Syngellakis and Elzein [12] extended a boundary element formulation to incorporate any combination of loading and support conditions in plate buckling; Nerantzaki and Katsikadelis [8] presented a boundary element formulation for buckling of plates with variable thickness; Lin, Duffield and Shih [7] described general boundary element formulation for different boundary conditions and arbitrary planar shapes. Recently, Purbolaksono and Aliabadi [11] presented the first BEM plate buckling formulation based on a shear deformable theory to solve problems with a variety of loading and boundary conditions while Baiz and Aliabadi [3] presented the first BEM formulation for buckling analysis of shear deformable shallow shells, in which domain integrals were treated using quadratic isoparametric cells, buckling modes and buckling coefficients were obtained for different boundary conditions and geometries. Scarce studies on plate assemblies using BEM are available. Dirgantara and Aliabadi [6] presented an application of BEM for the analysis of plate structures subjected to a variety of loadings and boundary conditions using a shear deformable plate formulation. In the case of linear buckling for assembled plate structures, the only available work has been presented by Tanaka and Miyazaki [13] using classical plate

theory with domain discretization.

Boundary Integral Formulation. As it was presented by Purbolaksono and Aliabadi [11], appropriate forms of the linearized buckling problem for a shear deformable plate can be obtained from the out of plane integral equation by introducing a multiplication factor λ of a pseudo transversal body force $(N_{\alpha\beta}w_{3,\beta})_{,\alpha}$, resulting in a group of equation in terms of the prebuckling membrane stresses and the buckled displacements for each plate:

$$\begin{aligned} c_{ij}(\mathbf{x}')w_j(\mathbf{x}') + \int_{\Gamma} P_{ij}^*(\mathbf{x}', \mathbf{x})w_j(\mathbf{x}) d\Gamma(\mathbf{x}) &= \int_{\Gamma} W_{ij}^*(\mathbf{x}', \mathbf{x})p_j(\mathbf{x}) d\Gamma(\mathbf{x}) \\ &+ \lambda \int_{\Omega} W_{i3}^*(\mathbf{x}', \mathbf{X})f(\mathbf{X})d\Omega(\mathbf{X}) \end{aligned} \quad (1)$$

The out of plane deflection w_3 at the domain points \mathbf{X}' is required as the additional equation to arrange an eigenvalue problem, as follows:

$$\begin{aligned} w_3(\mathbf{X}') &= \int_{\Gamma} W_{3j}^*(\mathbf{X}', \mathbf{x})p_j(\mathbf{x}) d\Gamma(\mathbf{x}) - \int_{\Gamma} P_{3j}^*(\mathbf{X}', \mathbf{x})w_j(\mathbf{x}) d\Gamma(\mathbf{x}) \\ &+ \lambda \int_{\Omega} W_{33}^*(\mathbf{X}', \mathbf{X})f(\mathbf{X})d\Omega(\mathbf{X}) \end{aligned} \quad (2)$$

Derivatives $w_{3,\beta}(\mathbf{X})$ and $w_{3,\alpha\beta}(\mathbf{X})$ are expressed in terms of $w_3(\mathbf{X})$ by the use of radial basis functions, as explained in [11]. $f(\mathbf{X})$ in the last integral of equations (1) and (2), is given by,

$$f(\mathbf{X}) = N_{\alpha\beta,\alpha}\mathbf{f}(r)_{,\beta}\mathbf{F}^{-1}w_3 + N_{\alpha\beta}\mathbf{f}(r)_{,\alpha}\mathbf{f}(r)_{,\beta}\mathbf{F}^{-1}w_3 \quad (3)$$

The boundary integral equation for membrane is also necessary in the linear buckling formulation of assembled plates:

$$\begin{aligned} c_{\theta\alpha}(\mathbf{x}')u_{\alpha}(\mathbf{x}') + \int_{\Gamma} T_{\theta\alpha}^*(\mathbf{x}', \mathbf{x})u_{\alpha}(\mathbf{x})d\Gamma(\mathbf{x}) \\ = \int_{\Gamma} U_{\theta\alpha}^*(\mathbf{x}', \mathbf{x})t_{\alpha}(\mathbf{x})d\Gamma(\mathbf{x}) + \int_{\Omega} U_{\theta\alpha}^*(\mathbf{x}', \mathbf{X})b_{\alpha}(\mathbf{X})d\Omega(\mathbf{X}) \end{aligned} \quad (4)$$

The membrane stresses at domain points \mathbf{X}' can be obtained after the derivative of equation (4) is introduced in the constitutive equation, resulting in the following boundary integral equation [6]:

$$\begin{aligned} N_{\alpha\beta}(\mathbf{X}') &= \int_{\Gamma} U_{\alpha\beta\gamma}^*(\mathbf{X}', \mathbf{x})t_{\gamma}(\mathbf{x})d\Gamma(\mathbf{x}) - \int_{\Gamma} T_{\alpha\beta\gamma}^*(\mathbf{X}', \mathbf{x})u_{\gamma}(\mathbf{x})d\Gamma(\mathbf{x}) \\ &+ \int_{\Omega} U_{\alpha\beta\gamma}^*(\mathbf{X}', \mathbf{X})b_{\gamma}(\mathbf{X})d\Omega(\mathbf{X}) \end{aligned} \quad (5)$$

As it can be seen from the integral equations presented above, a domain integral appears in the formulation. This integral is transferred to the boundary by the use of the dual reciprocity method (DRM) [11]:

$$\begin{aligned} \int_{\Omega} W_{ij}(\mathbf{x}', \mathbf{X})f(\mathbf{X})d\Omega &= \sum_{l=1}^L \left[c_{ik}(\mathbf{x}')\hat{w}_{kl}^3(\mathbf{x}') - \int_{\Gamma} W_{ik}(\mathbf{x}', \mathbf{X})\hat{p}_{kl}^3(\mathbf{X})d\Gamma \right. \\ &\left. + \int_{\Gamma} P_{ik}(\mathbf{x}', \mathbf{X})\hat{w}_{kl}^3(\mathbf{X})d\Gamma \right] \mathbf{F}^{-1}f^l(\mathbf{X}) \end{aligned} \quad (6)$$

where L is the number of collocation domain points chosen for the application of the DRM in each plate. $\hat{w}_{kl}^3, \hat{p}_{kl}^3$ are the plate bending particular solutions for a radial basis function $F(r) = 1 + r$ and are given in [14].

Multi-region BEM. Because two or more angled plates joined together are considered in this work, the approach proposed in [15] is followed. In order to simplify this approach, the local coordinate systems of each plate is assumed to be defined such that the x_2^m directions are all aligned with the global direction x_2 along a straight joining line. Base on this, the compatibility equations for each pair of plates (e.g. $m = 1$ and $m = 2$), and equilibrium equations (compatibility gives a system of $5M - 4$ equations and have to be supplemented with 4 equilibrium conditions) could be written as follows:

$$\begin{array}{l}
 \text{Compatibility} \\
 u_1^1 n_{11}^1 + w_3^1 n_{13}^1 = u_1^2 n_{11}^2 + w_3^2 n_{13}^2 \\
 u_1^1 n_{31}^1 + w_3^1 n_{33}^1 = u_1^2 n_{31}^2 + w_3^2 n_{33}^2 \\
 u_2^1 = u_2^2; \quad w_1^1 = w_1^2 \\
 w_2^1 = 0; \quad w_2^2 = 0
 \end{array}
 \quad
 \begin{array}{l}
 \text{Equilibrium} \\
 \sum_M (t_1^m n_{11}^m + p_3^m n_{13}^m) = 0 \\
 \sum_M (t_1^m n_{31}^m + p_3^m n_{33}^m) = 0 \\
 \sum_M t_2^m = 0 \\
 \sum_M p_1^m = 0
 \end{array}$$

n_{ik}^m are the components of the rotation matrix of plate m from local to global coordinates, and the upper index refers to $m = 1$ and $m = 2$. This approach relies on the assumption that the plate flexural rigidity in its own plane is so large that it is possible to ignore its associated deformation.

Solution Strategy. In order to implement the integral equations, the boundary of each plate is discretized into a series of quadratic isoparametric boundary elements, including the junction lines; while in the domain of each plate several points are required for the application of the dual reciprocity method. The numerical procedure to solve the linear eigenvalue buckling of assembled plate structures can be summarized as follows:

- Solution of the assembly under the in plane loading is performed, obtaining boundary displacements and tractions on all the plates (junctions and external boundaries).
- Membrane stresses at domain nodes in each plate $N_{\alpha\beta}(\mathbf{X}')$ are obtained with equation (5), with $b_\gamma = 0$.
- Approximated derivatives of membrane stresses and out of plane displacement are calculated (as explained in [11]), obtaining $f(\mathbf{X})$ from equation (3).
- Finally, the boundary integral equations for the buckling problem for the assembled plates are solved; obtaining buckling modes and buckling load factors.

Buckling equation can be written in matrix form for each plate j as follows,

$$\begin{aligned}
 & [\mathbf{H}]_{5N_j \times 5N_j} \{\mathbf{d}\}_{5N_j} - [\mathbf{G}]_{5N_j \times 15NE_j} \{\mathbf{b}\}_{15NE_j} = \\
 & \lambda \left\{ [\mathbf{H}]_{5N_j \times 5N_j} [\bar{\mathbf{d}}]_{5N_j \times L_j} - [\mathbf{G}]_{5N_j \times 15NE_j} [\bar{\mathbf{b}}]_{15NE_j \times L_j} \right\} [\mathbf{F}]_{L_j \times L_j}^{-1} \{f\}_{L_j}
 \end{aligned} \quad (7)$$

where N_j and NE_j are the number of boundary source points and number of boundary elements for plate j , respectively; L_j represent the number of domain points in plate j , \mathbf{d} is the displacement vectors while \mathbf{b} is the traction vector, $\bar{\mathbf{d}}$ and $\bar{\mathbf{b}}$ are matrices containing particular solutions and \mathbf{F} is the radial basis function matrix. The buckling system matrix for the assembled plate structure can be written as,

$$\begin{array}{|c|c|c|c|} \hline \mathbf{A}^j & 0 & 0 & 0 \\ \hline 0 & \dots & 0 & 0 \\ \hline 0 & 0 & \mathbf{A}^k & 0 \\ \hline 0 & 0 & 0 & \dots \\ \hline \mathbf{J}^{jk} & \dots & \mathbf{J}^{kj} & \dots \\ \hline \end{array} \times \begin{array}{|c|} \hline \mathbf{x}^j \\ \hline \dots \\ \hline \mathbf{x}^k \\ \hline \dots \\ \hline \end{array} = \lambda \begin{array}{|c|c|c|c|} \hline \mathbf{A}_b^j & 0 & 0 & 0 \\ \hline 0 & \dots & 0 & 0 \\ \hline 0 & 0 & \mathbf{A}_b^k & 0 \\ \hline 0 & 0 & 0 & \dots \\ \hline 0 & 0 & 0 & 0 \\ \hline \end{array} \times \begin{array}{|c|} \hline \mathbf{w}_3^j \\ \hline \dots \\ \hline \mathbf{w}_3^k \\ \hline \dots \\ \hline 0 \\ \hline \end{array} \quad (8)$$

where $[\mathbf{A}_b^j]_{(5 \times N_j) \times L_j}$ is the matrix containing the coefficients of unknowns out of plane displacement (buckling mode \mathbf{w}_3^j) for the plate j . In order to facilitate the notation, the total number of boundary degrees of freedom will be denoted by NT and the total number of domain degrees of freedom by LT . It is clear that:

$$NT = \sum_{m=1}^{MT} (5 \times N_m + 5 \times N_{J_m}); \quad LT = \sum_{m=1}^{MT} L_m \quad (9)$$

where MT is the total number of plates in the assembly. Using this new notation, equation (8) can be written as follows:

$$[\mathbf{B}]_{NT \times NT} \{\mathbf{Y}\}_{NT} = \lambda [\mathbf{K}]_{NT \times LT} \{\mathbf{w}_3\}_{LT} \quad (10)$$

In order to arrange an eigenvalue formulation, equation (2) can also be written in matrix form, similar as equation (10):

$$[\mathbf{I}] \{\mathbf{w}_3\}_{LT} = [\mathbf{BB}]_{LT \times NT} \{\mathbf{Y}\}_{NT} + \lambda [\mathbf{KK}]_{LT \times LT} \{\mathbf{w}_3\}_{LT} \quad (11)$$

where the matrices $[\mathbf{B}]$ and $[\mathbf{BB}]$ contain coefficient matrices related to the fundamental solutions; $[\mathbf{I}]$ is the identity matrix. Vector $\{\mathbf{Y}\}$ represents the unknown boundary conditions (including the junctions). Vector $\{\mathbf{w}_3\}$ contains the unknown out of plane displacement $w_3(\mathbf{X})$ of all the plates. Matrices $[\mathbf{K}]$ and $[\mathbf{KK}]$ are obtained by multiplication of the fundamental solutions with the prebuckling in plane stresses $N_{\alpha\beta}(\mathbf{X})$ and approximation functions. As it can be seen in equation (10) the only load considered in this transformed linearized buckling equation is the transverse body load $((N_{\alpha\beta} w_{3,\beta})_{,\alpha})$ multiplied by the critical load factor λ , implying that all the known values of w_i, u_α or p_i, t_α are set to zero (homogenous boundary conditions). Equation (10) can be rearranged in term of the unknown vector $\{\mathbf{Y}\}_{NT}$,

$$\{\mathbf{Y}\}_{NT} = \lambda [\mathbf{B}]_{NT \times 5NT}^{-1} [\mathbf{K}]_{NT \times LT} \{\mathbf{w}_3\}_{LT} \quad (12)$$

The substitution of equation (12) into equation (11) yields:

$$[\mathbf{I}]_{LT \times LT} \{\mathbf{w}_3\}_{LT} = \lambda [\mathbf{BB}]_{LT \times NT} [\mathbf{B}]_{NT \times NT}^{-1} [\mathbf{K}]_{NT \times LT} \{\mathbf{w}_3\}_{LT} + \lambda [\mathbf{KK}]_{LT \times LT} \{\mathbf{w}_3\}_{LT} \quad (13)$$

Equation (1) can be written as a standard eigenvalue problem equation as follows:

$$([\psi] - \frac{1}{\lambda} [\mathbf{I}]) \{\mathbf{w}_3\}_{LT} = 0 \quad (14)$$

Buckling analysis of shear deformable assembled plates has been presented as a standard eigenvalue problem; buckling modes $\{\mathbf{w}_3\}$ and buckling load factors λ can be directly obtained by solving equation (14).

Numerical Example. The following example presents local buckling coefficients for channel sections. Results are compared with the analytical solution given by Allen and Bulson [2], numerical solution obtained with a commercial FEM package (ABACUS), and additionally, the numerical results reported by Basu and Akhtar for an aspect ratio of $b_2/b_1 = 0.5$, see figure 1. The edges are simple supported ($w_3 = 0$) and uniform axial compressive is applied at the ends. Critical buckling load for the complete section is given in terms of the dimension of the central plate b_1 . The thickness is the same for all the plates and l represent the length of the assembly. As it can be seen from figure 1, the solutions from all the three different techniques agree well for channel sections of different dimensions ($b_2/b_1 = 1, 0.5, 0.2$ and $b_1/l = 1, 2, 3, 4, 5$). Buckling modes for configuration with $b_1/b_2 = 1$ and $b_1/l = 4$ are also given in figure 1. The plotted geometries correspond for a FEM model which contains 5652 nodes and 11022 linear triangular general purpose shell element (S3), while in the case of the BEM model, 168 boundary nodes (84 quadratic elements) with 180 domain nodes were employed. As it is expected for sections buckling locally into several half waves, it can be seen from figure 1 that the critical buckling coefficients tend to be virtually independent of length (except for short length members, when $l/b \lesssim 1$).

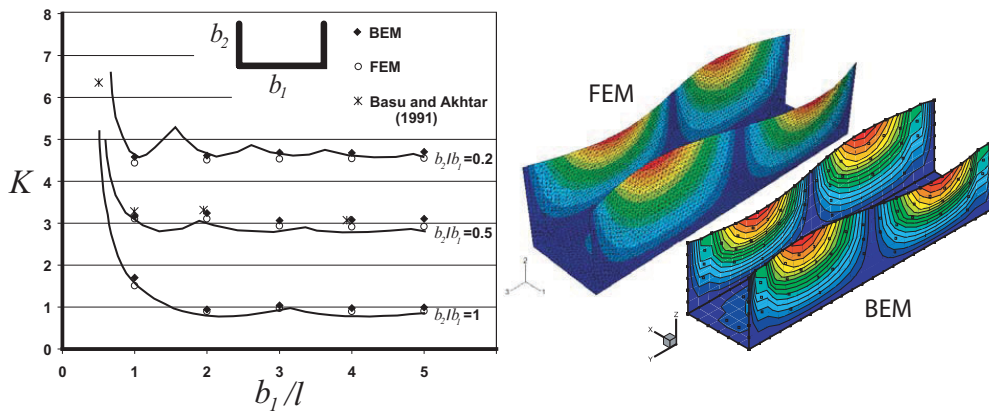


Figure 1: Buckling coefficients and buckling mode for channel sections.

Conclusion. In this work, a boundary element formulation for local eigen buckling of assembled plate structures under uniform compression was presented. Linear buckling equations were obtained by introducing multiplication factors of transverse loads (due to the large deflection of the out of plane displacement) into the bending and transverse shear boundary integral equation. The domain integral appearing in the formulation was transferred to the boundary by the dual reciprocity method. Membrane stresses at discrete domain points of each plate in the assembly ($N_{\alpha\beta}$) are obtained from the prebuckling state, resulting in a set of linear buckling equations in terms of the buckling deflection ($w_3 = 0$) and the buckling factors (λ). Buckling equations were presented as a standard eigenvalue problem, making possible to obtaining critical load factors and buckling modes in a single procedure. Base on the results, the presented boundary element approach can be used as an effective tool to solve linear local buckling problems of assembled plate structures subjected to axial compressive loads.

Acknowledgement. This work was supported by the Department of Aeronautical Engineering, Imperial College London.

References

- [1] Aliabadi, M.H., *The Boundary Element Method, vol II: Applications to Solid and Structures*, Wiley, Chichester (2002).
- [2] Allen, H.G., Bulson, P.S., *Background to Buckling*, Mc Graw Hill Book Company UK (1980).
- [3] Baiz, P.M., Aliabadi, M.H., Linear Buckling Analysis of Shallow Shells by the Boundary Domain Element Method, *Computer Modelling in Engineering & Sciences*, **13**, 19-34 (2006).
- [4] Basu, P.K., Akhtar, M.N., Interactive and local buckling of thin walled members, *Thin-Walled Structures*, **12**, 335-352 (1991).
- [5] Bedair, O.K., A contribution to the stability of stiffened plates under uniform compression, *Computers & Structures*, **66**, 535-570 (1998).
- [6] Dirgantara, T., Aliabadi, M.H., Boundary element analysis of assembled plate structures, *Communications in Numerical Methods in Engineering*, **17**, 749-760 (2001).
- [7] Lin, J., Duffield, R.C., Shih, H.R., Buckling Analysis of Elastic Plates by Boundary Element Method, *Engineering Analysis with Boundary Elements*, **23**, 131-137 (1999).
- [8] Nerantzaki, M.S. and Katsikadelis, J.T., Buckling of Plates with Variable Thickness - An Analog Equation Solution, *Engineering Analysis with Boundary Elements*, **18**, 149-154 (1996).
- [9] Ohga, M., Kawaguchi, K., Shigematsu, T., Buckling analysis of thin-walled members with closed cross sections, *Thin-Walled Structures*, **22**, 51-70 (1995).
- [10] Plank, R.J., Wittrick, W.H., Buckling under combined loading of thin, flat-walled structures by a complex finite strip method, *International Journal for Numerical Methods in Engineering*, **8**, 323-339 (1974).
- [11] Purbolaksono, J., Aliabadi, M.H., Buckling analysis of shear deformable plates by the boundary element method, *International Journal for Numerical Methods in Engineering*, **62**, 537-563 (2005).
- [12] Syngellakis, S., Elzein, A., Plate Buckling Loads by the Boundary Element Method, *International Journal Numerical Method in Engineering*, **37**, 1763-1778 (1994).
- [13] Tanaka, M., Miyazaki, K., Elastic buckling analysis of assembled plate structures by boundary element method, *Boundary Elements VIII*, Berlin, Springer, 537-546 (1986).
- [14] Wen, P.H., Aliabadi, M.H., Young, A., Application of Dual Reciprocity Method to Plates and Shells, *Engineering Analysis with Boundary Element*, **24**, 583-590 (2000).
- [15] Zienkiewicz, O.C., Taylor, R., *The Finite Element Method, Vol2: Solid Mechanics*, B-H, Oxford, (2000).

A procedure to solve generalized plane problems with contact using a 2D BEM code

A. Blázquez, V. Mantič and F. París

School of Engineering, University of Seville, Spain
abg@esi.us.es, mantic@esi.us.es, paris@esi.us.es

Keywords: Generalized plane problem, anisotropy, contact, particular solution, body forces, Saint-Venant problem, Voigt hypothesis.

Abstract. A new formulation is developed to solve generalized plane problems for anisotropic materials with possible friction contact zones. For an advantageous application of the Boundary Element Method, an explicit expression of a new particular solution of the problem associated to constant body forces is introduced and used to avoid domain integrations. Numerical solutions where the free edge effect in composite laminates is studied are presented.

Introduction

It is very instructive and useful to have the possibility to treat three-dimensional problems by means of two-dimensional models. It implies always a reduction in computing cost which is particularly significant in presence of non-linearities (for instance contact problems). The term generalized plane problem (GPP) [1], is adopted here for a three-dimensional problem in a homogeneous linear elastic cylindrical body where strains and stresses are independent of the axial-coordinate (Voigt hypothesis). Plane strain, generalized plane strain, generalized plane stress, pure torsion and generalized torsion can be considered as particular cases of GPP.

In this work an approach for the numerical solution, using a two-dimensional BEM code, of the GPP with contact between the solids involved in the problem is developed in a systematic way without any restrictions.

Formulation of the Generalized Plane Problem

Let us consider two homogeneous solids, A and B (an extension to more bodies is straightforward), of a cylindrical shape and of the same finite (or infinite) length, with constant transversal sections and straight parallel lateral surfaces. Contact may occur along a part of their lateral surfaces. Anisotropic linear elastic behavior is assumed for both solids. Let \mathcal{D}^K ($K=A,B$) be the three-dimensional domains, $\partial\mathcal{D}^K$ the lateral boundaries, and $\partial\mathcal{D}^{eK}$ the two extreme sections of the solids if they are of a finite length ($e=t$ or b respectively for top or bottom extremes of the bodies). The transversal section of \mathcal{D}^K determines a two-dimensional domain \mathcal{Q}^K , its boundary $\partial\mathcal{Q}^K$ being determined by the transversal section of $\partial\mathcal{D}^K$. An elastic problem for these solids will be called GPP if stresses and strains depend only on the planar coordinates of \mathcal{Q}^K . Integrating compatibility equations, the following general displacement solution field is obtained [2]:

$$\begin{aligned} u_1^K(x_1, x_2, x_3) &= -\frac{A^K}{2}x_3^2 + D^K x_2 x_3 + U_1^K(x_1, x_2) + \mu_1^K(x_2, x_3) \\ u_2^K(x_1, x_2, x_3) &= -\frac{B^K}{2}x_3^2 - D^K x_1 x_3 + U_2^K(x_1, x_2) + \mu_2^K(x_1, x_3) \\ u_3^K(x_1, x_2, x_3) &= (A^K x_1 + B^K x_2 + C^K)x_3 + U_3^K(x_1, x_2) + \mu_3^K(x_1, x_2) \end{aligned} \quad (1)$$

where the x_3 -axis is parallel to the axes of the cylinders; A^K , B^K , C^K and D^K ($K=A,B$) are constants, U_i^K ($i=1,2,3$) represent displacements of the transversal section independent of the x_3 -coordinate and μ_i^K ($i=1,2,3$) represent a rigid body movement. Substituting (1) into compatibility, then into constitutive and finally into equilibrium equations gives [2]:

$$L_{ij}^K U_j^K + f_i^K = 0 \quad (2)$$

where L_{ij}^K are given in terms of the elastic stiffnesses, c_{ij} (defined using the contracted Voigt notation):

$$\begin{aligned} L_{11}^K &= c_{11}^K \frac{\partial^2}{\partial x_1^2} + 2c_{16}^K \frac{\partial^2}{\partial x_1 \partial x_2} + c_{66}^K \frac{\partial^2}{\partial x_2^2} & L_{12}^K &= L_{21}^K = c_{16}^K \frac{\partial^2}{\partial x_1^2} + (c_{12}^K + c_{66}^K) \frac{\partial^2}{\partial x_1 \partial x_2} + c_{26}^K \frac{\partial^2}{\partial x_2^2} \\ L_{22}^K &= c_{66}^K \frac{\partial^2}{\partial x_1^2} + 2c_{26}^K \frac{\partial^2}{\partial x_1 \partial x_2} + c_{22}^K \frac{\partial^2}{\partial x_2^2} & L_{13}^K &= L_{31}^K = c_{15}^K \frac{\partial^2}{\partial x_1^2} + (c_{14}^K + c_{56}^K) \frac{\partial^2}{\partial x_1 \partial x_2} + c_{46}^K \frac{\partial^2}{\partial x_2^2} \\ L_{33}^K &= c_{55}^K \frac{\partial^2}{\partial x_1^2} + 2c_{45}^K \frac{\partial^2}{\partial x_1 \partial x_2} + c_{44}^K \frac{\partial^2}{\partial x_2^2} & L_{23}^K &= L_{32}^K = c_{56}^K \frac{\partial^2}{\partial x_1^2} + (c_{25}^K + c_{46}^K) \frac{\partial^2}{\partial x_1 \partial x_2} + c_{24}^K \frac{\partial^2}{\partial x_2^2} \end{aligned} \quad (3)$$

and where the modified body forces f_i^K are defined by the original body forces of the problem, the elastic stiffnesses and the constants A^K , B^K and D^K :

$$\begin{aligned} f_1^K &= X_1^K + c_{13}^K A^K + c_{36}^K B^K + (c_{56}^K - c_{14}^K) D^K \\ f_2^K &= X_2^K + c_{36}^K A^K + c_{23}^K B^K + (c_{25}^K - c_{46}^K) D^K \\ f_3^K &= X_3^K + c_{35}^K A^K + c_{34}^K B^K \end{aligned} \quad (4)$$

Boundary conditions at the extreme sections. Normally these conditions are established in terms of the resultant forces and moments:

$$F_j^K = \int_{\partial D^{eK}} \sigma_{j3}^K da \quad M_1^K = \int_{\partial D^{eK}} \sigma_{33}^K x'_2 da \quad M_2^K = \int_{\partial D^{eK}} \sigma_{33}^K x'_1 da \quad M_3^K = \int_{\partial D^{eK}} (\sigma_{23}^K x'_1 - \sigma_{13}^K x'_2) da \quad (5)$$

where $e=t,b$; $j=1,2,3$ and the coordinates x'_1 , x'_2 are referred to the principal axes of inertia of the section. Due to the fact that stresses are independent of the x_3 -coordinate, these conditions must be identical at both extreme sections. Some previous works [1,3,4] adopt restrictions which are not strictly necessary. Assuming typical hypothesis on the functions U_i^K ($i=1,2,3$) (for instance those derived from the bar model or from the laminate theory), eqs. (5) are transformed to a linear system whose unknowns are constants A^K , B^K , C^K , D^K and the variations $U_{3,1}$ and $U_{3,2}$. In some cases such an assumption is not straightforward, and an iterative procedure may be required.

If conditions are established on the displacements field, usually on u_3^K , some of the conditions given in (5) will be changed. In any case, constants A^K , B^K , C^K and D^K are assumed hereinafter known.

Boundary conditions on the lateral boundary. Because of the stresses do not depend of the x_3 -coordinate and the displacement field must have the general form indicated by eq (1), it is enough to impose the conditions on a particular transversal section, for instance at $x_3=0$. These conditions are shown in Table 1.

Formulation of the Equivalent Generalized Plane Strain Problem (EGPSP)

In order to solve a GPP using a 2D BEM code, the problem will be decomposed into two problems:

$$\varepsilon_{ij}^K = \begin{pmatrix} U_{1,1}^K & (U_{1,2}^K + U_{2,1}^K)/2 & U_{3,1}^K/2 \\ (U_{1,2}^K + U_{2,1}^K)/2 & U_{2,2}^K & U_{3,2}^K/2 \\ U_{3,1}^K/2 & U_{3,2}^K/2 & 0 \end{pmatrix} + \begin{pmatrix} 0 & 0 & D^K x_2 \\ 0 & 0 & -D^K x_1 \\ D^K x_2 & -D^K x_1 & A^K x_1 + B^K x_2 + C^K \end{pmatrix} = \varepsilon_{ij}^{*K} + \varepsilon_{ij}^{aK} \quad (6)$$

The problem defined by the material stiffnesses c_{ij}^K , the strains ε_j^{*K} , the stresses $\sigma_i^{*K} = c_{ij}^K \varepsilon_j^{*K}$ ($i,j=1,\dots,6$) and by the displacements $u_i^{*K} = U_i^K$ ($i,j=1,2,3$) defined in \mathcal{L}^K is denoted here as an equivalent generalized plane strain problem EGPSP [1,2]. Magnitudes corresponding to the GPP and to the EGPSP are related by:

$$u_i^K(x_3=0) = U_i^K = u_i^{*K} \quad f_i^K = X_i^{*K} \quad i=1,2,3$$

$$\varepsilon_{ij}^K = \varepsilon_{ij}^{*K} + \varepsilon_{ij}^{aK} \quad \sigma_i^K = c_{ij}^K \varepsilon_j^K = \sigma_i^{*K} + \sigma_i^{aK} \quad i,j=1,\dots,6 \quad (7)$$

Recall that ε_{ij}^{aK} and σ_i^{aK} depend on the constants A^K , B^K , C^K and D^K , which have known values.

Boundary conditions, summarized in Table 1, can be deduced applying (7) to the conditions of the GPP. In Table 1, \mathbf{t}_i^K represents the total tangential traction to the lateral boundary (whose components are in s and l directions), $\mu > 0$ is the friction coefficient and $\lambda > 0$ forces opposite direction of tangential stress and sliding.

Table 1: Boundary conditions for the GPP and the EGPP

		GPP	EGPP	
t -boundary conditions		$t_i^K = \bar{t}_i^K$	$t_i^{*K} = \bar{t}_i^K - t_i^{aK}$	$i=1,2,3$
u -boundary conditions		$u_i^K = U_i^K = \bar{u}_i^K$	$u_i^{*K} = \bar{u}_i^K$	$i=1,2,3$
Contact boundary conditions	Equilibrium	$t_i^A - t_i^B = 0$	$t_i^{*A} - t_i^{*B} = -t_i^{aA} + t_i^{aB}$	$i=n,s,l$
	Compatibility	$u_n^A + u_n^B = 0$	$u_n^A + u_n^B = 0$	
	Adhesion	$u_i^A + u_i^B = 0$	$u_i^{*A} + u_i^{*B} = 0$	$i=s,l$
	Sliding	$ \mathbf{t}_i^K + \mu t_n^K = 0$ $t_i^K = -\lambda(u_i^A + u_i^B)$	$ \mathbf{t}_i^{*K} + \mathbf{t}_i^{aK} + \mu t_n^{*K} + \mu t_n^{aK} = 0$ $t_i^{*K} + t_i^{aK} = -\lambda(u_i^{*A} + u_i^{*B})$	$i=s,l$

The application of a set of contact conditions [5,6] is limited by: the conditions of the geometric non interference, the compressive character of the normal contact traction and the limit values of the tangential stress in relation to the normal stress and the dissipative character of the friction. Note that the application of some of these equations may lead to relations between the constant A^A , B^A , C^A , D^A , and A^B , B^B , C^B , D^B [2].

The EGPP is established as the solution of the Navier equation (2) in \mathcal{L}^K with boundary conditions given in Table 1, and can be solved by means of a two-dimensional numerical tool. Once the EGPP solution is obtained, displacements, strains and stresses of the original GPP are calculated using eqs (7) and (1).

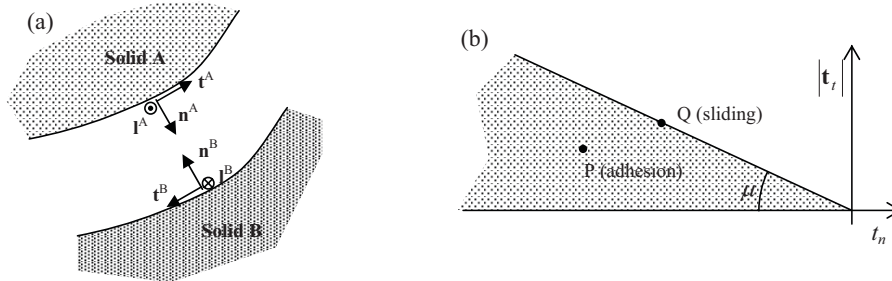


Figure 1: (a) Contact coordinate system, (b) Coulomb friction law.

Application of BEM to solve the GPP

In this work BEM is applied in its traditional collocation form [7]; the fundamental solution presented in [8,9] is used; the tensor of the free term is evaluated analytically as shown in [9]; elements give a piecewise linear approximation of displacements and tractions; nodes placed at the geometric ends are used as collocation points. Applying BEM procedure to the EGPP gives:

$$\mathbf{H}^K \mathbf{u}^{*K} = \mathbf{G}^K \mathbf{t}^{*K} + \mathbf{B}^{*K} \quad K=A,B \quad (8)$$

with the classical meaning of the matrices \mathbf{H}^K and \mathbf{G}^K , and vectors \mathbf{u}^{*K} and \mathbf{t}^{*K} ; \mathbf{B}^{*K} is a vector that groups the volume integrals due to the presence of body forces $X_i^{*K} = f_i^K$ defined in eq (4).

Domain forces vector. In order to avoid the discretization of the domain, \mathbf{B}^{*K} can be evaluated using an analytical approach as in [7,10], or using a particular solution as in [4,11]. Nevertheless, simple analytical

approaches for general anisotropic solids do not exist actually and the existing particular solutions are not applicable in the present study because in that of reference [4] the material must be monoclinic and in that of reference [11] it depends on the x_3 -coordinate. Thus, an explicit expression of a new particular solution of EGPSP in general anisotropic materials with constant body forces X_i^{*K} ($i=1,2,3$) is proposed here:

$$\begin{aligned} u_1^{pK} &= -\frac{1}{2}X_1^{*K}(b_{11,4}^K x_1^2 - b_{12,4}^K x_2^2) - \frac{1}{2}X_2^{*K}(2b_{12,5}^K x_1 x_2 + b_{26,5}^K x_2^2) - \frac{1}{4}X_3^{*K}(b_{15}^K x_1^2 + 2b_{14}^K x_1 x_2 + (b_{46}^K - b_{25}^K)x_2^2) \\ u_2^{pK} &= -\frac{1}{2}X_1^{*K}(b_{16,4}^K x_1^2 + 2b_{12,4}^K x_1 x_2) - \frac{1}{2}X_2^{*K}(b_{22,5}^K x_2^2 - b_{12,5}^K x_1^2) - \frac{1}{4}X_3^{*K}((b_{56}^K - b_{14}^K)x_1^2 + 2b_{25}^K x_1 x_2 + b_{24}^K x_2^2) \\ u_3^{pK} &= -\frac{1}{2}X_1^{*K}b_{15,4}^K x_1^2 - \frac{1}{2}X_2^{*K}b_{24,5}^K x_2^2 - \frac{1}{4}X_3^{*K}(b_{55}^K x_1^2 + 2b_{45}^K x_1 x_2 + b_{44}^K x_2^2) \end{aligned} \quad (9)$$

where b_{ij}^K are reduced elastic compliances [1,2]: $b_{ij}^K = s_{ij}^K - \frac{s_{i3}^K s_{3j}^K}{s_{33}^K}$, $s_{ij}^K = [c_{ij}^K]^{-1}$ being the compliance

matrix, and $b_{ij,k}^K = b_{ij}^K - \frac{b_{ik}^K b_{kj}^K}{b_{kk}^K}$ ($k=4,5$). The stresses can be deduced easily [2]. Applying (8) to this solution,

$\mathbf{B}^{*K} = \mathbf{H}^K \mathbf{u}^{pK} - \mathbf{G}^K \mathbf{t}^{pK}$ ($K=A,B$) can be computed without evaluation of volume integrals.

Application of boundary conditions. t and u -boundary conditions can be imposed directly, although requiring in some cases additional considerations [7]. On the contrary, contact conditions require some elaboration. Here, contact conditions are imposed in a weak form following the approach presented in [12], and summarized in the following: (a) Compatibility is imposed at one of the solids, for instance A, by means of Theorem of Virtual Forces; in the nodes of this solid two new variables, defining the separation and sliding, are defined. (b) Equilibrium is imposed at the other solid, B, by means of the Theorem of Virtual Displacements. (c) At the nodes of solid A that are in adhesion, the gap and sliding must be zero. (d) At the nodes of solid A that are sliding, the gap must be zero and the tangential component of the stress vector is related to the normal component by the friction coefficient.

Strategy of solution. Three strategies to solve the GPP by a 2D-BEM code are presented and commented in [2]. The most attractive of them consists in expressing (8) in terms of the variables associated to the GPP at the specific transversal section $x_3=0$, by means of relations (7):

$$\mathbf{H}^K \mathbf{u}^K = \mathbf{G}^K (\mathbf{t}^K - \mathbf{t}^{aK}) + \mathbf{B}^{*K} = \mathbf{G}^K \mathbf{t}^K + (\mathbf{B}^{*K} - \mathbf{G}^K \mathbf{t}^{aK}) = \mathbf{G}^K \mathbf{t}^K + \mathbf{B}^K \quad K=A,B \quad (10)$$

In this way neither modifying the equations that define the boundary and contact conditions, Table 1, nor processing the initial data and final results are required.

Numerical example: Traction and bending of a laminate

The formulation here arisen has been presented more detailed in [2], where two examples of applications are discussed, and has been applied successfully to the study of the delamination process induced by transversal cracks of a composite laminate in [13]. In this work another example with the aim of validating the formulation is presented. It deals with the laminate of the Fig. 2a. Traction and bending are applied at $x=\pm 25\text{mm}$ faces, other faces being traction free. The problem can be analyzed defining two GPP, one in the xz plane and other in the yz plane; in this work only the yz -plane problem is presented (note that the loads are perpendicular to the yz -plane). The size of the elements adjacent to the selected points is shown in Fig. 2b. Because of the symmetry, only half of the problem is considered using implicit symmetry [7].

Two configurations, $[0/90]_s$ and $[90/0]_s$, are analyzed and compared with the laminate theory solution. The properties of the material are: $E_{11} = 45.6$ GPa, $E_{22} = E_{33} = 16.2$ GPa, $\nu_{12} = \nu_{13} = 0.278$, $\nu_{23} = 0.4$, $G_{12} = G_{13} = 5.83$ GPa and $G_{23} = 5.786$ GPa, fiber direction defining direction 1. The load is applied by means of an axial force equal to $N = 100$ N/mm and a bending moment equal to $M = 10$ N mm/mm. Assuming the laminate theory hypothesis, constants are calculated for the two aforementioned configurations; their values being shown in Table 2.

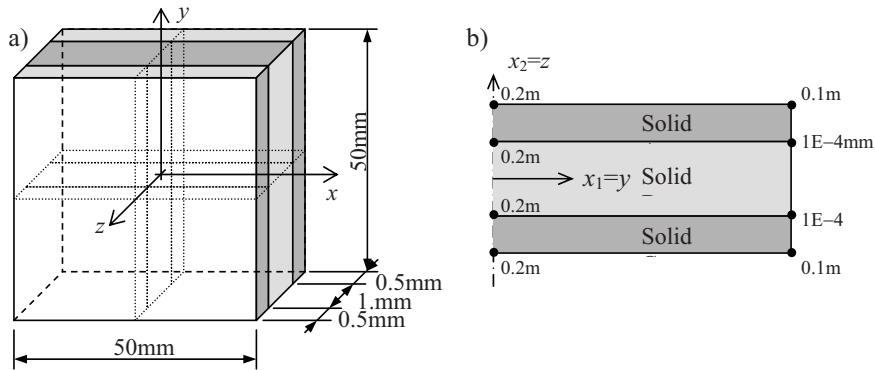


Figure 2: Problem configuration and BEM-mesh scheme.

Table 2: Constant values for the configuration analyzed

Configuration	$A^A = A^B = A^C$	$B^A = B^B = B^C$	$C^A = C^B = C^C$	$D^A = D^B = D^C$
$[0/90]_s$	0	$-3.56639E-4$	$1.60785E-3$	0
$[90/0]_s$	0	$-7.52307E-4$	$1.60785E-3$	0

In Fig. 3 the behavior of the displacements, normalized by the average elongation in direction x of the specimen ($u_{ref}=0.04mm$), are shown for the $[0/90]_s$ configuration. Continuous lines represent the BEM solution and dashed lines represent the laminated theory solution. Results for the $[90/0]_s$ configuration are very similar and are not presented here for the sake of brevity.

The u_y displacement is very close to the linear evolution and results are not distinguishable from the laminate theory. Some differences are noted for the u_z displacement, the maximum difference being equal to 5.25% for the $[0/90]_s$ configuration (and slightly smaller for the $[90/0]_s$ configuration).

Obviously, the laminate theory is unable to evaluate the thickness variation and the traction appearing at the interface. In Fig. 4 the normal and tangential components of the stress vector along the interfaces are shown. These results have been normalized by the maximum traction applied to the specimen when linear distribution of stresses is assumed ($t_{ref} = 57.5$ MPa).

For every configuration, the components of stress vectors have similar behavior along both interfaces, the zone affected by the free edge effect being of the order of the specimen thickness. Nevertheless, singular character of the components of the stress vector is clearly identified. This behavior appears because of the presence of a multimaterial corner and may be the origin of a delamination crack. Although very close to the corner the two configurations have tensile stresses, the distributions are very different: whereas in the $[0/90]_s$ configuration the interface zone subjected to tensile stresses has a size comparable to the ply thickness, in the case of the $[90/0]_s$ configuration this zone is of a very small size, which clearly induces different behavior, in terms of delamination, of both configurations.

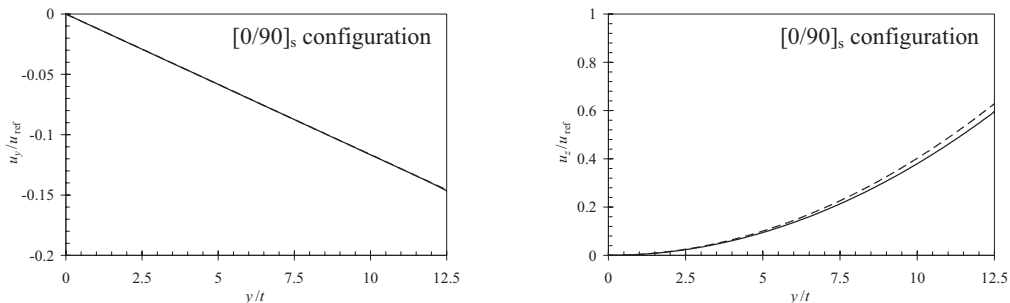


Figure 3: Behavior of the displacements at the middle line of the laminate $[0/90]_s$.

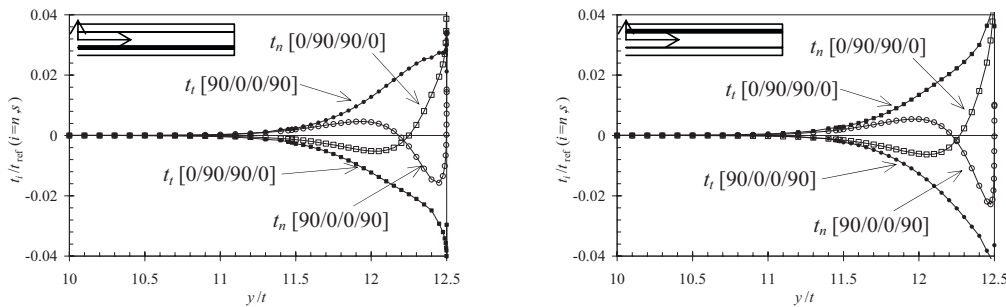


Figure 4: Components of the stress vector along the two interfaces

Summary and conclusions

Formulation of the GPP for cylindrical solids in contact, in which stresses (and strains) are independent of the coordinate oriented along the axis of the cylinder (Voigt hypothesis), is developed in a completely general form, with no restrictions on material symmetries, volume forces, boundary or contact conditions.

To solve the contact GPP by the BEM, an EGSP has been defined in the transversal section at $x_3 = 0$. In this problem, fictitious constant body forces depending of the material characteristics appear. To tackle these body forces in an efficient way by BEM a new particular solution has been proposed.

To show the possibilities of the procedure, an example corresponding to a laminate loaded in tension and bending has been solved. The results have been compared with that afforded by the laminate theory, the agreement being very good in the zones not affected by the free edge effect.

Acknowledgement

The authors acknowledge the financial support from the Spanish Ministry of Science and Technology (Project No. MAT2003-03315) and Junta de Andalucía (Proyecto de Excelencia 1207EP)

References

- [1] S.G. Lekhnitskii. *Theory of Elasticity of an Anisotropic Body*. MIR Publishers (1981).
- [2] A. Blázquez, V. Mantič and F. París. *Engng. Anal. with Boundary Elements*, **30**, 489-502 (2006).
- [3] J.-Q. Tarn. *Int. J. of Solids and Structures*, **39**, 5143-5155 (2002).
- [4] A. Deb and P.K. Banerjee. *Communications in Applied Numerical Methods*, **6**, 111-119 (1990).
- [5] T. Andersson, B. Fredriksson and A.B.G. Persson. *New Developments in Boundary Element Methods*, CML Publications, 239-258 (1980).
- [6] F. París and J.A. Garrido. *Int. J. for Engng. Anal. with Boundary Elements*, **6**, 202-213 (1989).
- [7] F. París and J. Cañas. *Boundary Element Method. Fundamentals and Applications*. Oxford University Press (1997).
- [8] V. Mantič and F. París. *Computational Mechanics*, **22**, 77-87 (1998).
- [9] V. Mantič and F. París. *Advances in Boundary Element Techniques V*, V.M.A. Leitão and M.H. Aliabadi (Eds.), 57-62 (2004).
- [10] J.J. Zhang, C.L. Tan and F.F. Afagh. *Int. J. for Numerical Methods in Engineering*, **40**, 89-109 (1997).
- [11] E. Pan and B. Amadei. *Applied Mathematical Modelling*, **20**, 114-120 (1996).
- [12] A. Blázquez, F. París and V. Mantič. *Int. J. of Solids and Structures*, **35**, 3259-3278 (1998).
- [13] V. Mantič, A. Blázquez, F. París and N.L. McCartney. *IABEM-2002* (CD) (2002).

Accelerating fluid layers

Gregory Baker

Department of Mathematics
The Ohio State University
231 W. 18th Ave
Columbus, Ohio 43210
USA.

Keywords: Free Surface Flow, dipole distributions.

Abstract. A liquid column in a vertical channel is assumed to lie above a gas and below either another free surface or is capped by a solid boundary. A pressure difference across the two free surfaces will cause the layer to accelerate and be susceptible to instability. Alternately, the solid boundary that caps the layer may be accelerated and cause motion at the free surface. In either case, boundary integral techniques can be used to capture the motion of the free surfaces under the assumption the motion is irrotational. In particular, dipole distribution can be used, leading to coupled Fredholm integral equations of the second kind. In the case of two free surfaces, the Fredholm integral equations are singular. The application of the Fredholm alternative provides a way to determine the acceleration of the layer. The formulation and numerical solution is provided for both cases and results presented that describe the difference in behavior when the upper surface is free or capped.

Formulation. Liquid in a vertical channel is constrained to lie between two surfaces, one free and the other either capped with a solid boundary or also free. A schematic is presented in Fig. 1. The density of the fluid is ρ . The fluid is assumed incompressible and the pressure P can take on different values above and below the layer. A pressure difference will, of course, cause the layer to accelerate and the objective of this article is to show how the motion of the free surfaces can be followed very accurately through the use of boundary integral techniques. If the upper surface is capped, then its motion is given and P_1 is no longer relevant.

Let the location of the interfaces be parametrized as $(X_j(p, t), Y_j(p, t))$ with $j = 1, 2$ indicating the lower, upper interfaces respectively. For convenience, the interface locations are written in complex form,

$$X_j(p, t) + iY_j(p, t) = Z_j(p, t) = z_j(p, t) + i\bar{y}_j(t), \quad (1)$$

where $\bar{y}_j(t)$ is the mean height of the j th interface.

With the additional assumption that the flow is irrotational, we may introduce a velocity potential ϕ and a streamfunction ψ that satisfy $\nabla^2\phi = \nabla^2\psi = 0$. Introduce the complex potential $\Phi = \phi + i\psi$ and express it in terms of dipole distributions along the surfaces:

$$\Phi(Z) = \frac{1}{4\pi i} \sum_{k=1}^2 \int_0^{2\pi} \mu_k \alpha_k(p) Z_{kp}(p) \cot \left\{ \frac{Z - Z_k(p)}{2} \right\} dp - iV(t)z, \quad (2)$$

where $\mu_k(p)$, a real-valued function, is the strength of the dipole distribution along the k th interface. The additional term accounts for the possible acceleration of the layer. Also assumed is that the width of the channel is 2π , a convenient choice for spectral methods. The parameters α_k determine whether the potential or the streamfunction is being expressed in terms of the dipole distributions. For a free surface, $\alpha = 1$ determines the potential, a quantity governed by Bernoulli's equation, whereas $\alpha = i$ determines the streamfunction, a quantity governed by the motion of a solid surface. Along the interfaces, we define the complex potential $\Phi_j(p)$ as $\Phi(Z_j(p))$ where the principal-value of the singular integral in (2) is taken. This means that as we approach the lower interface from above, the potential approaches the value

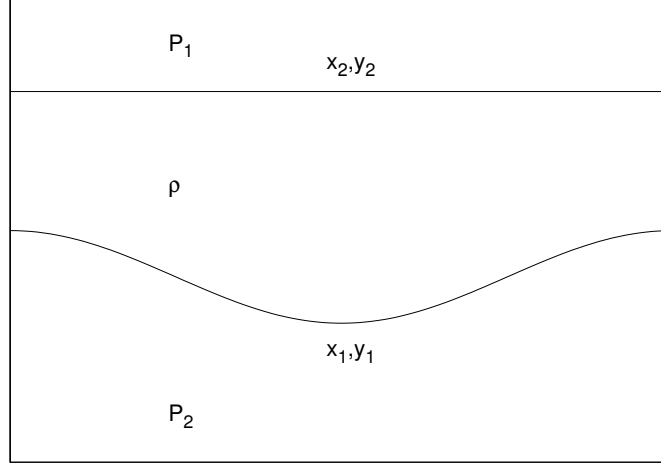


Figure 1: A schematic of the fluid layer.

On the other hand,

$$\Phi \rightarrow \Phi_2(p) + \frac{\alpha \mu_2(p)}{2}. \quad (4)$$

as we approach the upper interface from below. These results lead to Fredholm integral equations for the dipole strengths, but the details depend on whether the surface is free or capped.

Free Surfaces. We follow Baker, McCrory, Verdon, and Orszag [1] in defining the motion of the interfaces to be that of the fluid. Thus,

$$\frac{d\bar{y}_j}{dt} = V, \quad (5)$$

$$\frac{\partial z_j^*}{\partial t} = q_j^* \equiv \frac{\Phi_{jp}}{z_{jp}} + \frac{w_j \mu_{jp}}{2 z_{jp}}. \quad (6)$$

Subscripts with respect to p indicate differentiation, and the parameter w_j takes the values, $w_1 = -1$ and $w_2 = 1$, for the motion of the markers on the bottom and top interfaces respectively, a natural physical choice which also has useful mathematical properties [2].

As described in [1], the evolution of the dipole sheet strengths is determined by substituting (12) into Bernoulli's equation. Here the choice $\alpha_1 = \alpha_2 = 1$ is appropriate. The result is two coupled Fredholm integral equations of the second kind,

$$\frac{w_j}{2} \frac{\partial \mu_j}{\partial t}(p) + \sum_{k=1}^2 \int_0^{2\pi} \frac{\partial \mu_k}{\partial t}(p') \text{Re} \{K_{jk}(p, p')\} dp' = G_j(p) - \frac{dV}{dt} (y_j(p) + \bar{y}_j), \quad (7)$$

where

$$G_j(p) = - \sum_{k=1}^2 \int_0^{2\pi} \mu_k(p') \text{Re} \{K_{tjk}(p, p')\} dp' + \frac{q_j q_j^*}{2} - \frac{P_j}{\rho} - g(y_j + \bar{y}_j) + C. \quad (8)$$

and its time rate of change, $K_{tjk}(p, p')$, is given by

$$K_{tjk}(p, p') = \frac{q_{kp}(p')}{4\pi i} \cot \left\{ \frac{Z_j(p) - Z_k(p')}{2} \right\} - \frac{Z_{kp}(p')}{8\pi i} (q_j(p) - q_k(p')) \operatorname{csc}^2 \left\{ \frac{Z_j(p) - Z_k(p')}{2} \right\}. \quad (10)$$

As shown in [1], these integral equations are singular, and they have solutions only if the following Fredholm condition is satisfied,

$$\frac{dV}{dt} \sum_{k=1}^2 \int_0^{2\pi} \tau_k(p') (y_k(p') + \bar{y}_k) dp' = \sum_{k=1}^2 \int_0^{2\pi} \tau_k(p') G_k(p') dp', \quad (11)$$

where τ_j are the eigenfunctions of the adjoint integral equations,

$$\frac{w_j}{2} \tau_j(p) + \sum_{k=1}^2 \int_0^{2\pi} \tau_k(p') \operatorname{Re} \left\{ K_{jk}^\dagger(p, p') \right\} dp' = 0. \quad (12)$$

The adjoint kernel is defined by

$$K_{jk}^\dagger(p, p') = K_{kj}(p', p). \quad (13)$$

Equation (11) determines the mean acceleration of the layer, and together with (5,6,7), determines the motion of the interfaces. Incidentally, the nontrivial homogeneous solutions to (7) are just constants which affect only the mean level of Φ . Thus the mean levels of μ_j may be set arbitrarily without affecting the motion of the liquid layer.

Capped Surfaces. The top of the liquid layer is now assumed to lie next to a solid boundary. We use the notation of the previous section, but $Z_2(p, t)$ is now a parametrization of the solid boundary. With the same decomposition as (1), the motion of the interface and solid boundary is given by

$$\frac{d\bar{y}_j}{dt} = V, \quad (14)$$

$$\frac{\partial z_2}{\partial t} = q_2, \quad (15)$$

$$\frac{\partial z_1^*}{\partial t} = q_1^* \equiv \frac{\Phi_{1p}}{z_{1p}} + \frac{w_1 \mu_{1p}}{2 z_{1p}}. \quad (16)$$

Here, q_2 is considered prescribed. It can be time-dependent and spatially varying, for example, as when a flexible boundary is used to generate motion in the liquid.

As described in Baker, Meiron and Orszag [3], the complex potential may be expressed as a dipole distribution along the interface for the real potential plus a dipole distribution along the solid boundary for the streamfunction. Thus $\alpha_1 = 1, \alpha_2 = i$.

Application of Bernoulli's equation at the interface leads to the same results as in (7) for $j = 1$.

An equation for the rate of change of μ_2 comes about from requiring that the normal velocity of the liquid vanishes at the solid boundary. Alternately, the streamfunction must be a constant, C say, along the solid boundary. Thus,

$$\frac{1}{2} \mu_2(p) + \sum_{k=1}^2 \int_0^{2\pi} \mu_k(p') \operatorname{Im} \left\{ \alpha_k K_{2k}(p, p') \right\} dp' = C. \quad (17)$$

By differentiating this equation, we obtain a second Fredholm integral equation of the second kind,

$$\frac{1}{2} \frac{\partial \mu_2}{\partial t}(p) + \sum_{k=1}^2 \int_0^{2\pi} \frac{\partial \mu_k}{\partial t}(p') \operatorname{Im} \left\{ \alpha_k K_{2k}(p, p') \right\} dp' = - \sum_{k=1}^2 \int_0^{2\pi} \mu_k(p') \operatorname{Im} \left\{ \alpha_k K_{t2k}(p, p') \right\} dp'. \quad (18)$$

Thus, (14,15,16,7($j = 1$),18) constitute a set of evolution equations for the interface. The coupled Fredholm equations (7($i = 1$), 18) are non-singular in this case.

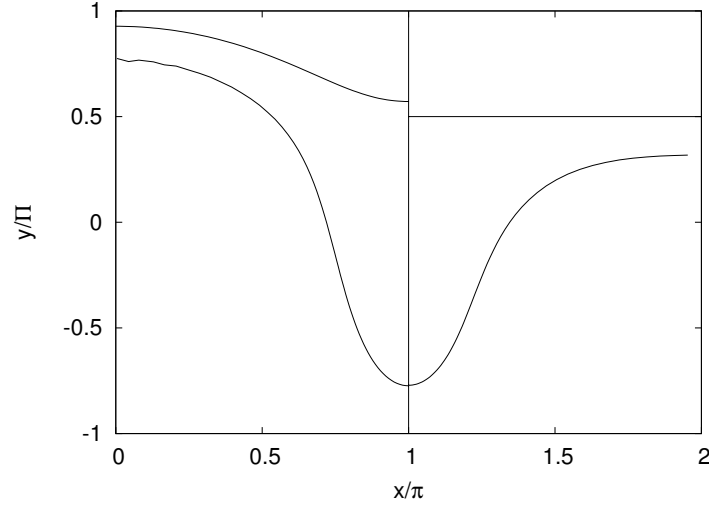


Figure 2: The location of the interfaces for two free surfaces are shown in the left half, while the location for the capped surface is shown as a mirror image in the right half.

As done in [1,3], we remove the singularity in the principal-valued integrals in (7,8,18) and apply the alternate point trapezoidal rule [4] with N intervals which has been shown to be spectrally accurate [5]. All derivatives are obtained through the use of cubic spline approximations.

The eigenvector τ is determined by the iteration, subject to the normalization $\sum \tau_j = N$ where N is the number of intervals. The iteration is considered converged when the pointwise difference between successive iterates is less than 10^{-10} . In this way, the solution to a discrete approximation to (12) is obtained.

The acceleration dV/dt is calculated by applying the trapezoidal rule to the integrals in (11).

The integral equation for the rate of change of the dipole strength $\partial\mu_j/\partial t$ is solved by iteration. The eigenvectors corresponding to eigenvalues $\lambda = \pm 1$ are removed by simply fixing the dipole strength to a constant value at a chosen point. The iteration is considered converged when the pointwise difference between successive iterates is less than 10^{-10} . The Fredholm integral equations (7,18) are solved in an identical manner.

Once q_j , dV/dt , and $\partial\mu_j/\partial t$ have been determined, we advance the location of the interface and its dipole strength by using a fourth-order Adams-Moulton predictor-corrector. The starting values are obtained by the standard fourth-order Runge-Kutta method.

For all the result reported here, we use the initial condition, $z_1 = p + 0.1\pi i \cos(p)$, $\mu_1 = 0$. In the case of the liquid column being open above, we set $z_2 = p + iH$, $\mu_2 = 0$ initially. For the liquid column capped above, we set $z_2 = p + iH$ and keep the boundary stationary $V = 0$ and $q_2 = 0$. We choose a simple cosine perturbation to the lower interface because it leads to a single bubble and spike, making a comparison of results quite easy. The physical constants are set as $g = \rho = 1$ which simply means a basic dimensionless form has been assumed.

The results at $t = 2.75$ are shown in Fig. 2. Two sets of calculations are displayed: the location of two free surfaces are shown in the left half of the column, while the free surface and the capped surface are show in the right half.

A resolution study establishes the accuracy in results. In particular, the maximum difference between the results for N and $2N$ are tracked as N is increased while $\Delta t = 0.005$ is kept fixed. For $t < 2$, the trend follows expectations. At first, there is a rapid improvement in accuracy reflecting the spectral accuracy of the

the lower interface near the left boundary. A slightly jagged profile is visible. The source of the error is in the integration along the upper surface for points fixed on the lower surface. If one examines the kernel K_{12} in (9), it is apparent that it varies strongly when z_2 is near z_1 due to the pole singularity in the cotangent function. This behavior has been studied extensively [6] and an elaborate procedure based on interpolation of quadrature points is proposed as a remedy. Current research seeks to remove the influence of the nearby pole singularity with an appropriate subtraction.

The results do show some striking physical behavior. Most notable is that the liquid in the falling spike appears oblivious to the influence of the upper surface whether it is free or capped. It simply falls under the influence of gravity. On the other hand, the rising gas below the lower surface is constrained by the capped surface, while the upper free surface allows the gas to penetrate rapidly into the upper region. With improved integration methods, it should be possible to extend these calculations further in time to observe the thinning of the layer as the bubble of gas accelerates upwards.

Acknowledgments

Some of the computations were performed at the Ohio Supercomputer Center under grant no. PAS555-4.

Reference

- [1] G.R.Baker, R.L.McCrory,C.P.Verdon and S.A.Orszag *J. Fluid Mech.*, **178**, 161-175 (1987).
- [2] G.R.Baker, R.E.Cafisch and M.Siegel *J. Fluid Mech.*,**252**, 51-78 (1993).
- [3] G.R.Baker, D.I.Meiron amd S.A.Orszag *J. Fluid Mech.*, **123**, 477-501 (1982).
- [4] G.R.Baker *Waves on Fluid Interfaces*, Academic Press (1983).
- [5] A.Sidi and M.Israeli *J. Sci. Comp.*, **3**, 201-220 (1988).
- [6] G.R. Baker and M.J.Shelley *J. Comp. Phys.*, **64**, 112-132 (1986).

Accurate modelling of rigid and soft inclusions in 2D elastic solids by the boundary element method

Luciano G. S. Leite & Wilson S. Venturini

São Carlos School of Engineering – University of São Paulo
Av. Trabalhador São-Carlense, 400, 13566-970 – São Carlos, Brazil.
venturin@sc.usp.br

Keywords: Boundary elements, sub-regions, inclusions

Abstract. In this work, a particular sub-region technique that does not require traction approximations along interfaces is used to model rigid and soft inclusions. The stability and the accuracy of the formulation have been studied for several applications, including the degenerated cases where one dimension is strongly reduced to represent an embedded bar. The rigid inclusions have been modelled by increasing their elastic modulus. On the other hand thin inclusions with elastic modulus reduced to nearly zero can accurately model crack problems. In all analysed cases, the obtained results have shown that this simple strategy is reliable and can be applied to complex stress analysis problems.

Introduction

Analysis of solids characterized by exhibiting inhomogeneous elastic domains is very suitable to be carried out by boundary element method. The method is very accurate to compute stress concentrations that appear in this kind of analysis. Using combinations of finite and boundary elements is the standard procedure to handle this problem [1,2]. However, inclusion problems can become very complex depending on the geometry and the material properties, which may require more accurate numerical representations. For instance, the inclusion can be very stiff or extremely flexible, large or small, thick or thin, when compared with solid sizes and material properties and also randomly displayed inside the domain. In some situations, the solutions in terms of interface forces are not accurate. Usually they come out showing some inconvenient oscillations. To overcome these difficulties, improved BEM formulations have recently appeared to deal with some important inclusion cases in elastic domains emphasising the performance of using integral equations in this context [3].

In this study we studying the performance of the technique suggested by the senior author [4] to analyse some cases of soft and rigid inclusions. In this formulation the in which isotropic inclusions are considered the difference of the inclusion elastic modulus is taken into account by an appropriate domain integral that can be transformed to the interfaces and boundary when a single Poisson's ratio is defined for the inclusion and the main domain. Moreover, as a result of this transforming all interface traction integrals are eliminated. The advantage of this modified formulation is the requirement of a reduced number of degrees of freedom along the interface. This formulation has been recently modified and successfully adopted to solve fibered two-dimensional solids [5].

In this work we analysed the performance of the technique suggested by the senior author [4] to deal with some cases of soft and rigid inclusions. We are going to analyse the case of thin inclusions with elastic modulus reduced to nearly zero that can model crack problems, rigid inclusion and also fibers embedded in 2D domain to simulate reinforced beam problems.

Integral equations of inhomogeneous solids

Let us consider the domain depicted in Fig. 1, formed by several sub-regions, Ω_m , with elasticity shear moduli, G_m . For a single Ω_m the integral representation of displacements reads:

$$c_{ij}^m u_j^m = - \int_{\Gamma_{m0}} p_{ij}^{m*} u_j^m d\Gamma - \sum_k \int_{\Gamma_{mk}} p_{ij}^{m*} u_j^m d\Gamma + \int_{\Gamma_{m0}} u_{ij}^{m*} p_j^m d\Gamma + \sum_k \int_{\Gamma_{mk}} u_{ij}^{m*} p_j^m d\Gamma \quad (1)$$

where u_j^m and p_j^m are boundary values, u_{ij}^{m*} and p_{ij}^{m*} are Kelvin's fundamental solutions referred to Ω_m , Γ_{m0} is the external sub-region boundary, Γ_{mk} are interfaces and N_a is the number of the adjacent connected sub-regions; no summation on m is implied.

We assume that the fundamental $u_{ij}^{m*} = u_{ij}^* G / G_m$ and $p_{ij}^{m*} = p_{ij}^*$, in which $*$ gives the fundamental values of a reference sub-region with shear modulus G .

One can combine all displacement representations, equation (1), individually written for each sub-region, enforcing equilibrium and compatibility conditions, to find an integral representation, containing only displacement values along interfaces as follows [4]:

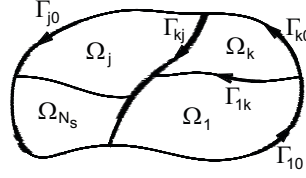


Figure 1. Zoned domain.

$$c_{ij}^k u_j^k = - \sum_{m=1}^{N_s} \frac{G_m}{G_k} \int_{\Gamma_m} p_{ij}^* u_j^m d\Gamma + \int_{\Gamma} u_{ij}^* p_j d\Gamma \quad (2)$$

The free term c_{ij}^k , for a collocation point in the sub-region Ω_k , is similar to the one obtained for a single region case, while for smooth points on the interface the value is $c_{ij}^k = \frac{1}{2}(1 + G_m / G_k) \delta_{ij}$, in which G_m the elasticity shear modulus of the adjacent sub-region.

From eq (2) one derives the stress integral equation as follows:

$$\sigma_{ij}^k = - \sum_{m=1}^{N_s} \frac{G_m}{G_k} \int_{\Gamma_k} S_{ijk}^{m*} u_k^m d\Gamma + \int_{\Gamma} D_{ijk}^* p_k d\Gamma \quad (3)$$

where S_{ijk}^{m*} and D_{ijk}^* are well-known fundamental solution tensors for the stress equation.

Algebraic equations

By discretizing the boundary and interfaces and approximating displacements and tractions along the boundary and displacements along interfaces eq (2) written for boundary and interface collocations gives the following algebraic equation:

$$\begin{bmatrix} \mathbf{H}_{bb} & \mathbf{H}_{bi} \\ \mathbf{H}_{ib} & \mathbf{H}_{ii} \end{bmatrix} \begin{Bmatrix} \mathbf{U}_b \\ \mathbf{u}_i \end{Bmatrix} = \begin{bmatrix} \mathbf{G}_{bb} \\ \mathbf{G}_{ib} \end{bmatrix} \{\mathbf{P}_b\} \quad (4)$$

where the subscripts b and i indicate nodes and values defined on the boundary and interface, respectively; \mathbf{U}_b and \mathbf{P}_b represent displacements and traction along the boundary and \mathbf{u}_i contains the interface displacements.

For the examples analysed here, only continuous and discontinuous linear elements have been used to approximate displacements along the boundary and interfaces and tractions along the boundary.

Equation (4) can be represented in the usual form: $\mathbf{HU} = \mathbf{GP}$. In this representation \mathbf{H} is a full-populated square matrix, while \mathbf{G} is a rectangular matrix. The final system of equations is however always smaller in comparison with the one obtained using the standard sub-region technique. It is also important to point out that boundary conditions can be assigned to boundary nodes. Thus, only \mathbf{U}_b and

P_b can be prescribed. The vector u_i is always unknown. Two unknowns are always assigned to boundary and interface nodes.

Similarly, from the stress integral equation we obtain:

$$\{\sigma\} = -[H'_b \ H'_i] \begin{Bmatrix} U_b \\ u_i \end{Bmatrix} + [G'_b] \{P_b\} \tag{5}$$

where H'_k and G'_k are matrices similar to the corresponding ones in eq (4), obtained by integrating the stress kernels S_{ijk}^{m*} and D_{ijk}^* , respectively.

The selection of the procedure to carry out the integrals over the boundary and particularly over the interface elements requires special attention. For this zoned problem, there are always collocation points defined very close to the elements and therefore the standard Gauss cannot be used to accurately perform the element integrals. Collocations defined along thin zone interface or inside them are always present and the corresponding integrals are always inaccurate if standard Gauss scheme were adopted. Herein, we have performed all boundary and interface element integrals using closed analytical expressions that were properly derived. A Gaussian numerical integral scheme used together with an efficient sub-element scheme [5] has also been used for comparison.

Numerical results

In order to demonstrate the capability of this formulation, two simple examples are solved and the results compared with solutions obtained by using a commercial FEM pack, other BEM approaches and also analytical solution.

The first example consists of analyzing the square shaped solid with a small square inclusion depicted in Fig. 2. The adopted sizes of the square domain and the inclusion are also given in the figure, together with the prescribed boundary values. Several discretizations have been tested to guarantee the convergence of the solution. The adopted uniform discretizations started from the coarsest case with 320 nodes to the finest one with 1440 nodes. We have studied the convergence and the stability of the method for inclusions defined by the elastic modulus $E_i = E \times 10^n$, assuming n varying from 1 to 10, being E the elastic modulus of the main square domain. The Poisson's ration assumed for this analysis was $\nu = 0.25$.

Fig. 3 gives only the relevant values of vertical displacements computed along the axis x defined by the interface direction, as indicated. The obtained results compare very well with the solution given by the element shell 43 of ANSYS (version 5.7) using a 6400 finite element mesh. Significant displacement changes occur only for $n \leq 2$. For higher inclusion elastic modulus, no practical variation in the displacement values was observed. Rigid inclusion case is obtained by simply increasing the inclusion elastic modulus E_i . For any value of $n \geq 4$, the results obtained along the axis x are practically the same, therefore equivalent to the rigid inclusion. Stable results were obtained for all assumed rigid cases ($n \geq 4$) up to $n=10$, demonstrating therefore the stability of the procedure.

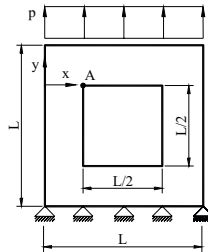


Figure 2. Square domain with an inclusion. Prescribed boundary values.

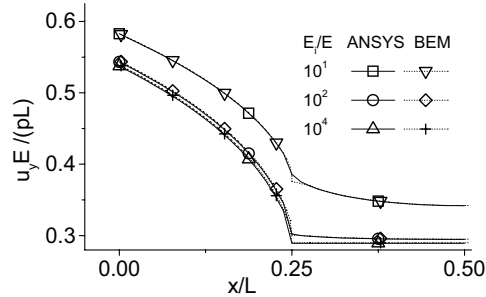


Figure 3. Vertical displacements along the axis x for different inclusion elastic modulus.

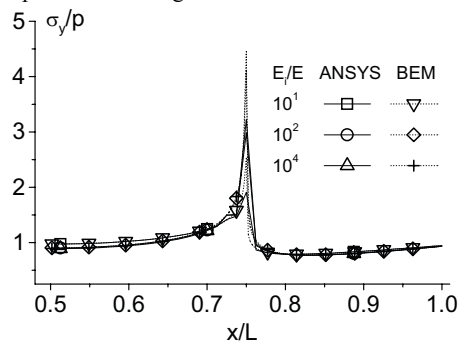


Figure 4. Stress component σ_y computed along the axis x .

Fig. 4 shows the comparison between BEM and ANSYS for stress (or traction) distributions along axis x . The obtained curves are completely smooth, exhibiting very high stress values over the corner vicinity.

The second example is a square domain, reinforced by a single thin bar obliquely displayed inside the matrix material, as shown in Fig. 5. The domain side and the thin bar given lengths are L and $2a$, respectively. The thin bar length was assumed $2a=L/4$, while its position is given by the eccentricity $(e_x, e_y)=(L/4, L/4)$ and the angle α . L has been assumed 2.0, while several bar thickness c , given in terms of the bar length $c = \beta 2a$, have been experimented.

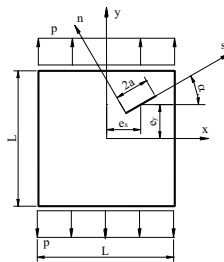


Figure 5. Reinforced square domain. Geometry and prescribed boundary values.

Several discretizations were tested to carry out all numerical analyses chosen to verify the performance of the formulation to deal with thin bar inclusions represented by degenerated 2D sub-region. The analysis started by using a very coarse discretization and then refining it to the finest one with 640 boundary nodes and 600 interface nodes.

Three analyses have been carried out to verify the formulation. First, we considered the usual case of a single thin inclusion embedded in the square domain. We have assumed that the thin inclusion elastic modulus is given by $E_i = 10E$, with β varying from 2×10^{-2} to 2×10^{-4} .

Figs. 6 and 7 show the displacement and stress distributions along the inclusion interface. The results obtained by using this degenerated 2D inclusion are practically the same ones obtained by using reinforced BEM approach or BEM-FEM combination for reinforced domains.

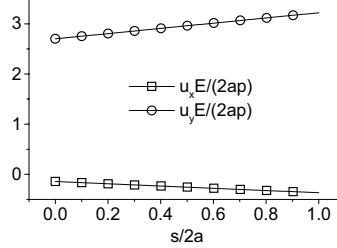


Figure 6. Displacement distribution along the inclusion interface s for $E_i = 10E$

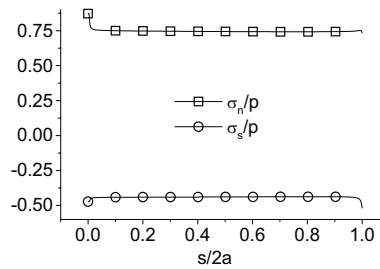
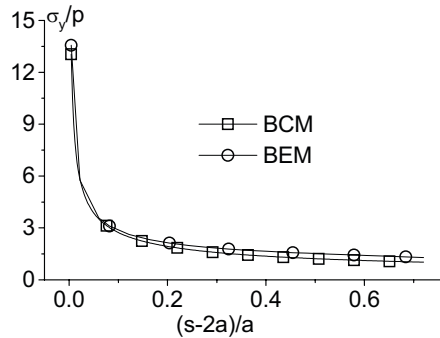


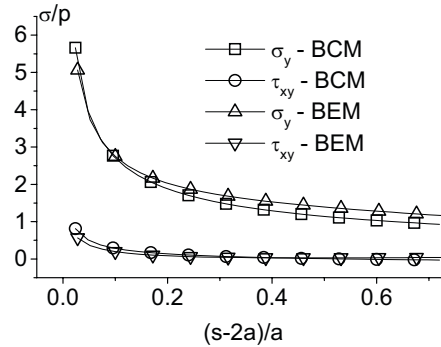
Figure 7. Stress distribution measured along the inclusion interface s for $E_i = 10E$



Figures 8. Normal stress (σ_y) along the axis s . Horizontal fracture case.

To simulate fracture using the thin inclusion elastic modulus E_i is reduced to zero. This formulation works because we are performing exactly the integral along the elements and are keeping a very small, but finite, distance between the two fracture lips. The numerical analysis of this case has demonstrated that adopting 320 nodes with continuous linear elements (discontinuous elements were used only to define the tip) was enough to obtain good results. Fig. 8 shows the normal stress (σ_y) distribution computed from the tip (axis s) and assuming the fracture angle $\alpha = 0.0$. The solution compares very well with the solution obtained by Yuannhan [6] using the boundary collocation method - BCM. The

accuracy of the solutions was also confirmed by solving the problem with $\alpha = \pi / 6$, as illustrated in Fig. 9. Numerical tests were also carried out to verify the independency of the algebraic equation written for two nodes defined at opposite lips. Stable systems of equations were observed for gap width $c = 4a10^{-6}$. On the other hand, much larger crack gaps, $c = 4a10^{-2}$, have been tested without any significant loss of accuracy. The results used for comparison were all obtained by assuming $c = 4a10^{-3}$.



Figures 9. Normal (σ_y) and shear (τ_{xy}) stress components along the axis s . Inclined fracture.

Conclusions

Modelling inclusion using the BEM sub-region formulation that does not require traction approximations along the interface has demonstrated to be an excellent technique. The results are accurate and the solution stable even when degenerated sub-regions are considered to model either thin, rigid or soft inclusions.

References

- [1] Zienkiewicz, O.C., Kelly, D.W. & Bettess, P., The coupling of the finite element method and boundary solution problems. *International Journal for Numerical Methods in Engineering*, **11**, 355-375 (1977).
- [2] Beer, G., Implementation of combined boundary element finite element analysis with application in geomechanics. In: Banerjee, P.K.; Watson, J.O, eds. *Developments in boundary element methods - 4*. App. Sc. Pub. (1986).
- [3] Dong, C.Y., Lo, S.H. & Cheung, Y.K., Stress analysis of inclusion problems of various shapes in an infinite anisotropic elastic medium. *Computer Methods in Applied Mechanics and Engineering*, **192** (5-6), 683-696 (2003).
- [4] Venturini, W.S., Alternative formulations of the boundary element method for potential and elastic zoned problems. *Engineering Analysis with Boundary Elements*, **9** (3), 203-207 (1992).
- [5] Leite, L.G.S., Coda, H.B. & Venturini, W.S., Two-dimensional solids reinforced by thin bars using the boundary element method. *Engineering Analysis with Boundary Elements*, **27**, 193-201 (2003).
- [6] Yuannhan W., Axymmetric crack problems calculated by the boundary collocation method. *Engineering Fracture Mechanics*, **40**, 133-143 (1991).

Boundary elements for elastoplastic solids without domain integrals

M. Brun¹, K. Bertoldi² and D. Bigoni³

¹ Laboratoire de Mécanique des Solides

Ecole Polytechnique - 91128, Palaiseau, FRANCE

brunmi@lms.polytechnique.fr

^{2,3} Dipartimento di Ingegneria Meccanica Strutturale

Università di Trento. Via Mesiano, 77 - 38050, Povo, Trento, ITALIA

katia.bertoldi@ing.unitn.it, bigoni@ing.unitn.it

Keywords: Boundary integral equations, elastoplasticity, domain integrals, Green's function.

Abstract. A boundary element method is proposed to analyze boundary value problems for elastoplastic solids. The technique is based on the use of the Green's functions corresponding to both the loading and unloading branches of the tangent constitutive operators to solve for the plastic and the elastic region. Two main advantages make the present approach particularly attractive: first, domain integrals are avoided, so that the numerical and analytical treatment of hypersingular terms is not needed; second, since the loading branch of the constitutive operator is formally analogous to a special type of elastic anisotropic constitutive tensor, the method is developed as a straightforward application of multidomain techniques for linear constitutive operators. Numerical examples, involving explicit and implicit integration schemes, shows that the method is stable, performs well and give results in accordance with commercial codes.

Introduction

The boundary element method is broadly used to solve elastoplastic boundary value problems for its well-known advantages such as volume discretization of only the plastic zone, easy treatment of incompressibility, easy treatment of singularities and infinite domains.

Following the standard approach, volume integral appears in the governing integral equations, containing hypersingular terms multiplied by the unknown plastic strain rate fields. A new methodology is proposed here, retaining all the advantages of these types of formulation, but avoiding domain integrals. As a consequence, though a volume discretization remains necessary to account for the inhomogeneity of plastic deformation, the implementation simplifies drastically, when compared to the other techniques currently in use. In particular the presented approach traces back to [1,2] where it was suggested that the use of a Green's function defined for incremental deformation leads to a boundary integral formulation for homogeneous finite deformation in which domain integrals are simply absent.

Constitutive Assumptions

In the framework of small deformations, we consider constitutive equations, which are both plastically and elastically incompressible. In particular, we specialize the J_2 -flow theory of plasticity to linear hardening. The rate constitutive equations, complemented by the incompressibility constraint $div \mathbf{v} = 0$, are

$$\dot{\boldsymbol{\sigma}} - \dot{p}\mathbf{I} = \begin{cases} 2\mu\dot{\boldsymbol{\varepsilon}} - \frac{4\mu^2}{h+\mu}\langle\mathbf{Q}\dot{\boldsymbol{\varepsilon}}\rangle\mathbf{Q} & \text{if } \sqrt{J_2} - \frac{\sqrt{\sigma_0}}{3} = 0 \\ 2\mu\dot{\boldsymbol{\varepsilon}} & \text{if } \sqrt{J_2} - \frac{\sqrt{\sigma_0}}{3} < 0 \end{cases}, \quad (1)$$

where \dot{p} is the rate of pressure, μ the elastic shear modulus, h the hardening coefficient, σ_0 the current value of yielding in uniaxial stress and the yield function gradient and the second invariant of the deviatoric stress \mathbf{S} are:

$$\mathbf{Q} = \frac{\mathbf{S}}{2\sqrt{J_2}}, \quad J_2 = \frac{\mathbf{S} \cdot \mathbf{S}}{2}.$$

The Green's Function and Boundary Integral Equations

With reference to an infinite medium characterized by constitutive eqn. (1), the Green's function set $\{v_i^g, \dot{p}^g\}$ is [1]

$$v_i^g(r, \theta) = \frac{1}{2\pi^2} \left\{ \frac{\pi \delta_{ig} \log \hat{r}}{[(2-t)\gamma_2 + 1-t]\sqrt{-\gamma_1} + [(2-t)\gamma_1 + 1-t]\sqrt{-\gamma_2}} + \int_0^{\pi/2} [K_i^g(\alpha + \vartheta) + (3-2g)(3-2t)K_i^g(\alpha - \vartheta)] \log(\cos \alpha) d\alpha \right\} \quad (2)$$

and

$$\dot{p}^g(r, \theta) = -\frac{1}{2\pi r} \left\{ \cos \left[\theta - (g-1) \frac{\pi}{2} \right] + \frac{1}{\pi} \int_0^{\pi} \frac{\tilde{K}_g(\alpha + \theta)}{\cos \alpha} d\alpha \right\} \quad (3)$$

where r and θ are the generic polar coordinates singling out the generic point with respect to the position \mathbf{y} of the concentrated force, indices t and g range between 1 and 2, and

$$K_i^g(\alpha) = \frac{\sin[\alpha + (t-1)\pi/2] \sin[\alpha + (g-1)\pi/2]}{\mu - 4(\mu - \mu_*) \sin^2 \alpha \cos^2 \alpha},$$

$$\gamma_{1,2} = 1 - 2 \frac{\mu_*}{\mu} \pm \sqrt{\frac{\mu_*}{\mu} \left(\frac{\mu_*}{\mu} - 1 \right)} \quad \text{and}$$

$$\tilde{K}_g(\alpha) = 2K_g^g(\alpha) \cos \left[\alpha + (g-1) \frac{\pi}{2} \right] \left(\frac{\mu_*}{\mu} - 1 \right) (2 \cos^2 \alpha - 1).$$

Boundary Element Formulation

We consider mixed boundary value problems in which velocities \mathbf{v} and incremental tractions $\dot{\mathbf{t}}$ are prescribed functions defined on separate portions ∂B_v and ∂B_t , respectively, of the boundary ∂B of a solid B.

In this context, an integral representation exists relating the velocity (at points interior, exterior or at the boundary of the body) to the boundary values of traction rates and velocities

$$e^g \mathbf{v}(\mathbf{y}) = \int_{\partial B} \dot{\mathbf{t}}(\mathbf{x}) \mathbf{v}^g(\mathbf{x}, \mathbf{y}) d\mathbf{x} - \int_{\partial B} \dot{\mathbf{v}}(\mathbf{x}, \mathbf{y}) \mathbf{v}(\mathbf{x}) d\mathbf{x} \quad (4)$$

where the e^g -matrix depends on the material parameters and the geometry in the neighborhood of the point \mathbf{y} . A discretized version of the integral equation (4) is then applied on the collocation nodes of the discretized boundary geometry in order to derive the *collocation boundary element method*.

Integration of the incremental solution

Two different techniques are employed to integrate the incremental solution; in the first case an explicit forward Euler scheme is adopted, which allows for a precise transition from elastic to plastic and viceversa and imposes a limit on the maximum possible rotations of the principal stress reference systems.

The second scheme is an iterative strategy akin to techniques used for the finite element method. In particular we propose a Newton-Rapson iterative method based on a cutting plane return-mapping algorithm [3] where the equilibrium, the compatibility and the yield conditions are satisfied at the end of each incremental step.

Numerical examples

The first example concerns the punch problem sketched in Fig. 1a which has been investigated also by [4] employing finite elements. The load per unit length \mathbf{t} applied to the material and normalized through division by the load at first yielding \mathbf{t}_0 is plotted in Fig.1b versus the vertical displacement u_B of the point B (Fig. 1a) divided by the displacement at first yielding u_{0B} for the initial yield stress $\sigma_0/\mu=3/500$ and for the different values of the hardening coefficient $h/\mu=0.5, 0.1, 0.01$. The results concerning the two different integration schemes are compared in Fig. 1b with simulations obtained with ABAQUS-Standard (Ver 6.4.-1, Hibbit Karlsson and Sorensen Inc.).

The level sets of the equivalent plastic strain

$$\mathcal{E}_{equiv} = \int_{loading\ path} \sqrt{\frac{3}{2} \dot{\boldsymbol{\epsilon}}^p \cdot \dot{\boldsymbol{\epsilon}}^p} dt$$

has been showed in Fig. 1c for the BEM with explicit integration scheme and a finite element simulation. The results are shown for $h/\mu=0.01$ and $u_B, u_{0B}=12$.

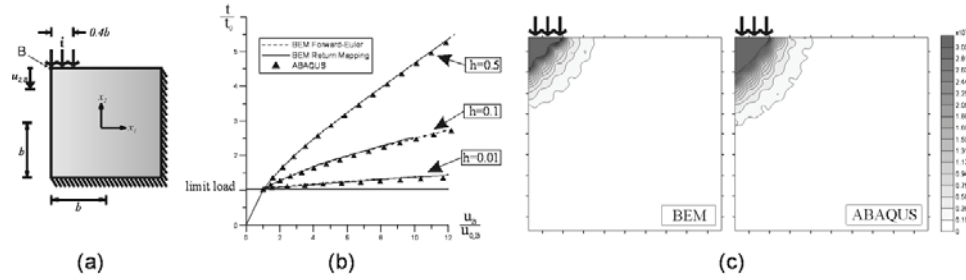


Fig. 1. Foundation on a vertical cut: (a) loading geometry, (b) load versus displacement curve, (c) level sets of plastic equivalent strain.

The second example concerns an infinite elastic-plastic medium containing two rectangular holes and loaded by imposing constant displacements on the internal ligament as indicated in Fig. 2a together with the geometrical discretization adopted. The level sets of the modulus of the velocity together with the level sets of the pressure distribution are shown in Fig. 2b and Fig. 2c, respectively, for initial yield stress $\sigma_0/\mu=3/500$, hardening coefficient $h/\mu=0.01$, and for the displacement of the central left plate equal to $u/u_0=6$ where u_0 is the displacement at first yielding.

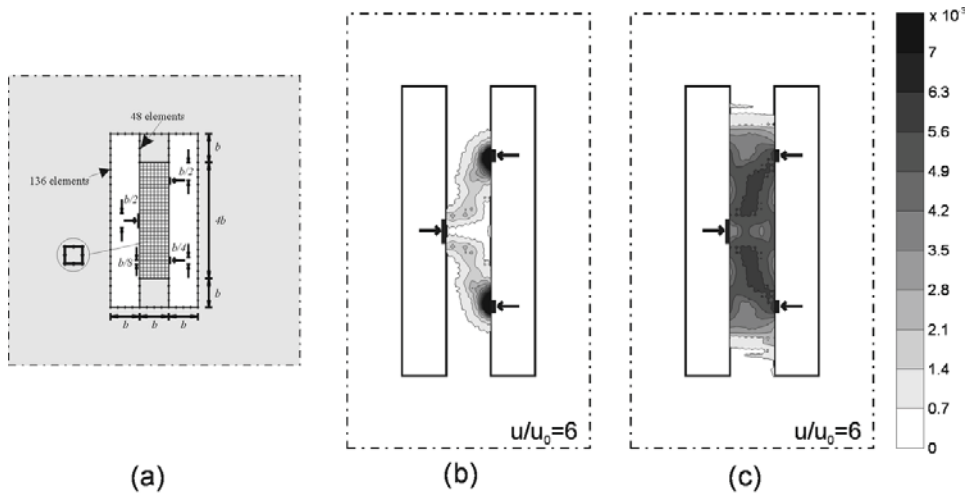


Fig. 2. Two rectangular holes in an infinite elastic-plastic media: (a) loading geometry and geometrical discretization, (b) level sets of velocity modulus, (c) level sets of pressure distribution.

Acknowledgments

Financial support of MIUR-PRIN 2005 (prot. 2005085973_002) is gratefully acknowledged.

References

- [1] M. Brun *Boundary element techniques in finite elasticity*, PhD Thesis, (2003).
- [2] M. Brun, D. Capuani and D. Bigoni *A boundary element technique for incremental non-linear elasticity Part I: formulation*. *Comp. Meth. Appl. Mech Eng.* **192**, 2481-2499 (2003).
- [3] J.C. Simo, T.J.R. Hughes. *General return mapping algorithms for rate-independent plasticity*. *Const. Laws Eng. Mat.*, Desai CS (ed.) Elsevier: New York, 1995.
- [4] M. Cervera, M. Chiumenti, Q. Valverde, C. Agelet de Saraciba. *Mixed linear/linear simplicial elements for incompressible elasticity and plasticity*. *Comp. Meth. Appl. Mech Eng.* **192**, 5249-5263 (2003).

Time-domain BEM Formulation Applied to the Solution of the Scalar Wave Equation: a Step-by-Step Approach

J. A. M. Carrer¹ and W. J. Mansur²

¹ Programa de Pós-Graduação em Métodos Numéricos em Engenharia, Universidade Federal do Paraná, CEP 81531-990, Curitiba, PR, Brasil. e-mail: carrer@mat.ufpr.br

² Programa de Engenharia Civil, COPPE/UFRJ, Caixa Postal 68506, CEP 21945-970, Rio de Janeiro, RJ, Brasil. e-mail: webe@coc.ufrj.br

Keywords: Time-domain BEM, scalar wave equation, step-by-step analysis

Abstract. This article is concerned with the presentation of a time-domain BEM approach applied to the solution of the scalar wave equation for 2D problems. The basic idea is quite simple: the basic variables of the problem at time t_n (potential and flux) are computed with the results related to the potential and to its time derivative at time t_{n-1} playing the role of the “initial conditions”. This time-marching scheme needs the computation of the potential and its time derivative at all boundary nodes and internal points, as well as the entire discretization of the domain. The convolution integrals of the standard time-domain BEM formulation, however, are not computed; the matrices assembled, only at the initial time interval, are those related to the potential, flux and to the potential time derivative. One example is presented at the end of the article, in order to verify the potentialities of the proposed formulation.

Introduction

This work is concerned with the solution of scalar wave equation for 2D problems by employing a modified version of the standard time-domain BEM (TD-BEM) formulation. The approach proposed in this work is quite simple and is based on the computation of the basic variables of the problem at time t_n (potential and flux) with the results related to the potential and to its time derivative at time t_{n-1} playing the role of the “initial conditions”. As a consequence, due to the time translation property of the kernels, e.g. Mansur [1], the convolution integrals, which appear in the standard TD-BEM formulation, are no longer evaluated. As a matter of fact, as will be demonstrated in the next section, time integration is restricted only to the interval $[0, \Delta t]$. However, some steps must be followed in order to avoid the computation of the convolution integrals. Initially, it becomes necessary to calculate the derivative, with respect to time, of the potential from the basic BEM integral equation (potential integral equation), thus generating the velocity integral equation. As the potential and the velocity at time t_{n-1} play the role of “initial conditions” for the potential, for the flux and for the velocity at time t_n , the domain integrals of the TD-BEM formulation, restricted to the part of the domain with non-homogeneous initial conditions, are extended to the entire domain. Besides, by following an approach similar to that from the D-BEM formulation, e.g. Carrer & Mansur [2], Hatzigeorgiou and Beskos [3], potential and velocity integral equations are applied at boundary nodes and internal points simultaneously; generating an enlarged system of equations. After solving this system of equations one has the values of the potential and of the flux at boundary nodes and the values of the potential at internal points. The values of the velocity are computed directly, since the boundary variables are already known. It is important to mention that the integral equations are written by making use of the concept of finite part of integrals (FPI), due to Hadamard [4].

In the numerical implementation carried out, linear boundary elements and linear triangular cells were adopted. In order to verify the potentialities of the proposed formulation, one example is presented at the end of the article.

Standard TD-BEM Integral Equations

Potential Integral Equation. The potential integral equation associated in the TD-BEM formulation of the scalar wave problem, by making use of the concept of FPI, can be written as (note that Γ is the boundary; Ω is the domain, or the part of the domain, that presents non-homogeneous initial conditions):

$$\begin{aligned}
4\pi c(\xi)u(\xi,t) &= \int_{\Gamma} \int_0^{t^+} u^*(X,t;\xi,\tau)p(X,\tau)d\tau d\Gamma(X) - \int_{\Gamma} \frac{\partial r}{\partial n} \int_0^{t^+} u_r^*(X,t;\xi,\tau)u(X,\tau)d\tau d\Gamma(X) - \\
\frac{1}{c} \int_{\Gamma} \frac{\partial r}{\partial n} u_o^*(X,t;\xi)u_o(X)d\Gamma(X) &+ \frac{1}{c^2} \int_{\Omega} u_o^*(X,t;\xi)v_o(X)d\Omega(X) + \\
\frac{1}{c} \int_{\Omega} \left[\frac{u_o^*(X,t;\xi)}{r} - b_o^*(X,t;\xi) \right] u_o(X)d\Omega(X) &+ \frac{1}{c} \int_{\Omega} u_o^*(X,t;\xi) \frac{\partial u_o(X)}{\partial r} d\Omega(X) \quad (1)
\end{aligned}$$

In eq(1), the coefficient $c(\xi)$ assumes the same values of the static case, e.g. Mansur [1], and the subscript 'o' means that $\tau = 0$.

The fundamental solution, $u^*(X,t;\xi,\tau)$, that corresponds to the effect of a source represented by an impulse at $t = \tau$ located at $X = \xi$ propagating with velocity equal to c , has the following expression:

$$u^*(X,t;\xi,\tau) = U^*(X,t;\xi,\tau)H[c(t-\tau)-r] \quad \text{with} \quad U^*(X,t;\xi,\tau) = \frac{2c}{\sqrt{c^2(t-\tau)^2-r^2}} \quad (2)$$

In expression (2), $H[c(t-\tau)-r]$ stands for the Heaviside function ($r = r(X;\xi)$ is the distance between the field (X) and the source (ξ) points).

The functions $b^*(X,t;\xi,\tau)$ and $u_r^*(X,t;\xi,\tau)$, in eq. (1), are given by:

$$b^*(X,t;\xi,\tau) = B^*(X,t;\xi,\tau)H[c(t-\tau)-r] \quad \text{with} \quad B^*(X,t;\xi,\tau) = \frac{2c[c(t-\tau)-r]}{[c^2(t-\tau)^2-r^2]^{3/2}} \quad (3)$$

and:

$$u_r^*(X,t;\xi,\tau) = U_r^*(X,t;\xi,\tau)H[c(t-\tau)-r] \quad \text{with} \quad U_r^*(X,t;\xi,\tau) = \frac{2cr}{[c^2(t-\tau)^2-r^2]^{3/2}} \quad (4)$$

The symbol \int on the second term on the right-hand-side of eq (1) stands for the FPI, Hadamard [4]:

$$\int_0^{t^+} u_r^*(X,t;\xi,\tau)u(X,\tau)d\tau = \lim_{\tau \rightarrow t-r/c} \left\{ \int_0^{\tau} U_r^*(X,t;\xi,\tau)u(X,\tau)d\tau - \frac{1}{c} U^*(X,t;\xi,\tau)u(X,\tau) \right\} \quad (5)$$

Velocity Integral Equation. The integral equation associated to the potential time derivative can be written as:

$$\begin{aligned}
4\pi c(\xi) \frac{\partial u(\xi,t)}{\partial t} &= \int_{\Gamma} \int_0^{t^+} u_r^*(X,t;\xi,\tau)p(X,\tau)d\tau d\Gamma(X) - \int_{\Gamma} \frac{\partial}{\partial t} \left(\int_0^{t^+} u_r^*(X,t;\xi,\tau)u(X,\tau)d\tau \right) \frac{\partial r}{\partial n} d\Gamma(X) \\
- \frac{1}{c} \int_{\Gamma} \frac{\partial r}{\partial n} \frac{\partial u_o^*(X,t;\xi)}{\partial t} u_o(X)d\Gamma(X) &+ \frac{\partial}{\partial t} \left(I_{\Omega,v_o} + I_{\Omega,u_o} \right) \quad (6)
\end{aligned}$$

where, for simplicity and because the resulting expressions do not require any special treatment in the domain integration, the time derivative of the domain integrals related to the non-homogeneous initial conditions are indicated by the last term on the right-hand-side of eq(6).

The FPI in the first term on the right-hand-side of eq(6) is interpreted as:

$$\int_0^{t^+} u_t^*(X,t;\xi,\tau)p(X,\tau)d\tau = \lim_{\tau \rightarrow t-\tau/c} \left\{ \int_0^\tau U_t^*(X,t;\xi,\tau)p(X,\tau)d\tau + U^*(X,t;\xi,\tau)p(X,\tau) \right\} \quad (7)$$

The function $u_t^*(X,t;\xi,\tau)$ in expression (7) is given by:

$$u_t^*(X,t;\xi,\tau) = U_t^*(X,t;\xi,\tau)H[c(t-\tau) - r] \quad \text{with} \quad U_t^*(X,t;\xi,\tau) = -\frac{2c^3(t-\tau)}{[c^2(t-\tau)^2 - r^2]^{3/2}} \quad (8)$$

The time derivative of the FPI indicated on the second term on the right-hand-side of eq(13) is defined as:

$$\frac{\partial}{\partial t} \left(\int_0^{t^+} u_r^*(X,t;\xi,\tau)u(X,\tau)d\tau \right) = \lim_{\tau \rightarrow t-\tau/c} \left\{ \int_0^\tau \frac{\partial U_t^*(X,t;\xi,\tau)}{\partial t} u(X,\tau)d\tau + U_t^*(X,t;\xi,\tau)u(X,\tau) - \frac{1}{c} U^*(X,t;\xi,\tau) \frac{\partial u(X,\tau)}{\partial \tau} \right\} \quad (9)$$

Numerical Solution

For the solution of the problem, linear and constant time variations were assumed, respectively, for the potential and for the flux. Following the usual time-domain BEM approach, e.g. Mansur [1] and Dominguez [5], time integrals were computed analytically. For the boundary approximation, isoparametric linear elements are employed; the domain is approximated by triangular linear cells, in which the initial conditions vary linearly.

The application of equation (1) to all boundary nodes and internal points simultaneously (in the next section this procedure becomes clearer) generates the system of equations below:

$$\begin{bmatrix} \mathbf{H}^{bb} & \mathbf{0} \\ \mathbf{H}^{db} & \mathbf{I} \end{bmatrix} \begin{Bmatrix} \mathbf{u}_n^b \\ \mathbf{u}_n^d \end{Bmatrix} = \begin{bmatrix} \mathbf{G}^{bb} \\ \mathbf{G}^{db} \end{bmatrix} \left\{ \mathbf{p}_n^b \right\} + \begin{bmatrix} \mathbf{U}^{bb} & \mathbf{U}^{bd} \\ \mathbf{U}^{db} & \mathbf{U}^{dd} \end{bmatrix} \begin{Bmatrix} \mathbf{u}_o^b \\ \mathbf{u}_o^d \end{Bmatrix} + \begin{bmatrix} \mathbf{V}^{bb} & \mathbf{V}^{bd} \\ \mathbf{V}^{db} & \mathbf{V}^{dd} \end{bmatrix} \begin{Bmatrix} \mathbf{v}_o^b \\ \mathbf{v}_o^d \end{Bmatrix} \quad (10)$$

In eq(10) the superscripts b and d correspond to the boundary and to the domain (internal points), respectively. In the sub-matrices, the first and second superscripts correspond, respectively, to the positions of the source and of the field points. The identity matrix, $\mathbf{I} = \mathbf{H}^{dd}$, is related to the coefficients $c(\xi) = 1$ of the internal points. Eq(10) can be written in a more compact way as:

$$\mathbf{C} \mathbf{u}_n + \sum_{m=0}^n \mathbf{H}_{nm} \mathbf{u}_m = \sum_{m=0}^n \mathbf{G}_{nm} \mathbf{p}_m + \mathbf{U}_n \mathbf{u}_o + \mathbf{V}_n \mathbf{v}_o \quad (11)$$

After the solution of the system of equations represented by eq(11), the velocity at boundary nodes and internal points can be computed directly, with the use of eq(6). The resulting system of equation can be represented, in a compact form, as:

$$\mathbf{C}\mathbf{v}_n = \sum_{m=0}^n \bar{\mathbf{G}}_{nm} \mathbf{p}_m - \sum_{m=0}^n \bar{\mathbf{H}}_{nm} \mathbf{u}_m + \bar{\mathbf{U}}_n \mathbf{u}_o + \bar{\mathbf{V}}_n \mathbf{v}_o \quad (12)$$

Since matrix \mathbf{C} is a diagonal matrix, eq(12) above can easily be solved for \mathbf{v}_n .

Step-by-step Procedure. The solution procedure employed in this article is based mainly in the time translation property, e.g. Mansur [1], which can be written as:

$$u^*(X,t;\xi,\tau) = u^*(X,t+t_i;\xi,\tau+t_i) \quad (13)$$

Due to the time-translation property, one can write (note that, in the expression below, $k^*(X,t;\xi,\tau)$ represents a generic kernel and $q(X,\tau)$, a boundary variable):

$$\int_0^{\Delta t} k^*(X,t;\xi,\tau)q(X,\tau)d\tau = \int_{\Delta t}^{2\Delta t} k^*(X,t;\xi,\tau)q(X,\tau)d\tau = \dots = \int_{(n-1)\Delta t}^{n\Delta t} k^*(X,t;\xi,\tau)q(X,\tau)d\tau \quad (14)$$

The application of the translation property, as illustrated by eq(13), together with equations (1) and (6), enables one to solve the time-dependent problem by considering the results related to \mathbf{u}_{n-1} and \mathbf{v}_{n-1} as "initial conditions" in the computation of the results at time t_n . That is, in the computation of \mathbf{u}_n and \mathbf{v}_n , the convolution integrals, represented by the summation symbol in eq(11) and eq(12), are no longer computed. For the approach proposed here, the following versions of eq(11) and eq(12) can be written:

$$\mathbf{C}\mathbf{u}_n + \mathbf{H}_{nn} \mathbf{u}_n = \mathbf{G}_{nn} \mathbf{p}_n + \mathbf{U}_n \mathbf{u}_{n-1} + \mathbf{V}_n \mathbf{v}_{n-1} \quad (15)$$

$$\mathbf{C}\mathbf{v}_n = \bar{\mathbf{G}}_{nn} \mathbf{p}_n - \bar{\mathbf{H}}_{nn} \mathbf{u}_n + \bar{\mathbf{U}}_n \mathbf{u}_{n-1} + \bar{\mathbf{V}}_n \mathbf{v}_{n-1} \quad (16)$$

The values of the potentials and the velocities, treated as "initial conditions", are stored in the vectors \mathbf{u}_{n-1} and \mathbf{v}_{n-1} . Note that proceeding this way, the entire domain needs to be discretized. This means that the proposed approach is suitable for finite domain applications.

Example

An application is presented next. In order to verify the accuracy, numerical results are compared with the analytical solutions [6]. The dimensionless parameter $\beta = c\Delta t/l$, which relates the wave velocity (c), the smallest element length (l), and the time interval Δt (assumed constant), is used to estimate the time-step length.

One-dimensional rod. This example consists of a one-dimensional rod under a Heaviside-type forcing function, applied instantaneously at $t = 0$ and kept constant in time.

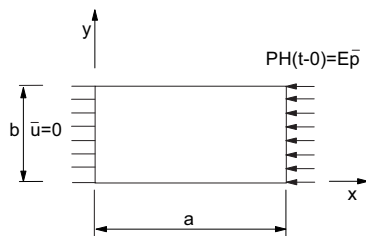


Fig. 1 – Geometry and boundary conditions

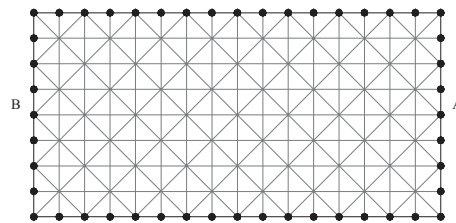


Fig.2 – Boundary and domain discretization

Boundary conditions and geometry are depicted in Fig. 1. Two analyses were carried out, in order to verify the convergence of the results furnished by the proposed formulation. In the first analysis, 48 boundary elements and 256 internal cells were employed, see Fig. 2. In the second analysis, 96 boundary elements and 1024 internal cells were employed. Results related to the potential and to the velocity ($v = \partial u / \partial t$) at node A($a, b/2$) are presented, respectively, in Fig. 3 and Fig. 4. Results related to the flux at node B($0, b/2$) are presented in Fig.5. It can be observed that, with the refinement of the mesh, the numerical damping, observed in both analyses; diminishes producing more reliable results. It is important to mention that the optimum time-step length was obtained by taking $\beta = 0.5$. This is not the value recommended by Mansur [1] for the standard TD-BEM formulation, i.e. $\beta = 0.6$.

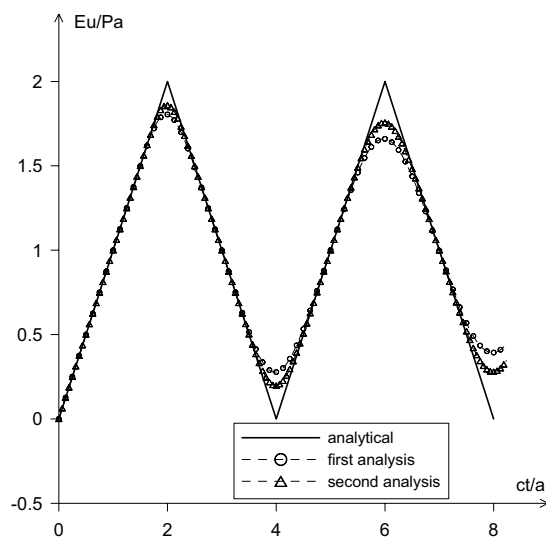


Fig.3 – Potential at node A($a, b/2$)

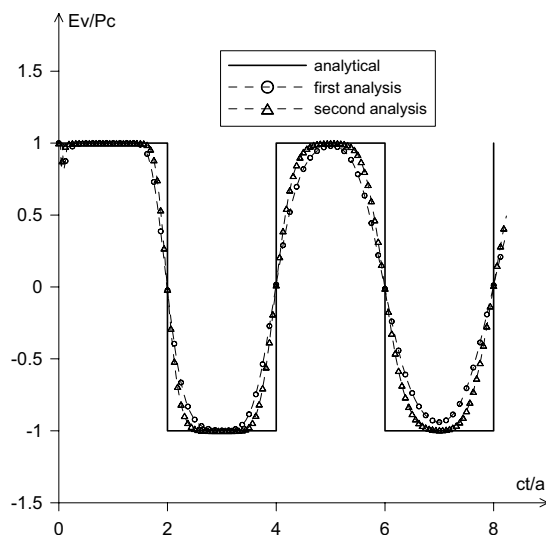


Fig.4 – Velocity at node A($a, b/2$)

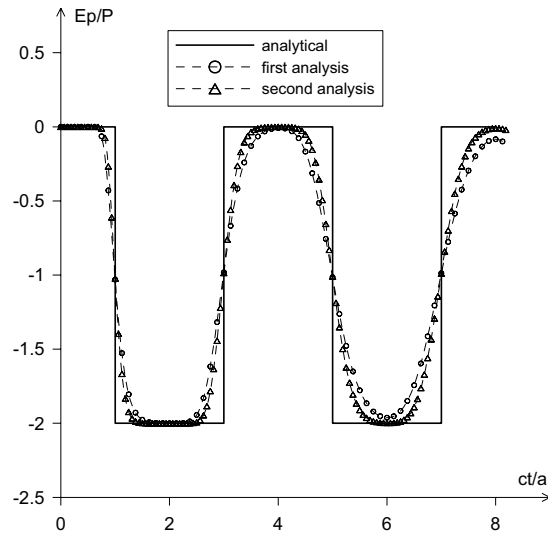


Fig.5 – Flux at node B(0, b/2)

Conclusions

In this work, a modified version of the standard TD-BEM formulation is presented. The main characteristic of proposed formulation and, perhaps, what could turn it attractive, is that the convolution integrals are no longer evaluated. Now, the results at a given value of the time, say t_n , are computed with the results related to the potential and to its time derivative at t_{n-1} playing the role of “initial conditions”. Note that such a version of the TD-BEM formulation, beside the basic integral equation, called here potential integral equation, also makes use of the integral equation corresponding to the velocity. Both integral equations are applied simultaneously to all boundary nodes and internal points, in order to obtain the results that will be used as “initial conditions” for the next time-step. This is the main disadvantage of the proposed formulation: as the entire domain needs to be discretized, the analysis of infinite domain problems becomes almost impossible or, at least, very expensive in the computational point of view, for late times results. In spite of the numerical damping observed in Figs. 3, 4 and 5, which deserves special attention and some effort to turn it smaller, the results presented encourage future research in this area.

Literature References

- [1] W.J. Mansur *A Time-Stepping Technique to Solve Wave Propagation Problems Using the Boundary Element Method*, Ph.D. Thesis, University of Southampton, England (1983).
- [2] J.A.M. Carrer & W.J. Mansur Alternative Time-Marching Schemes for Elastodynamic Analysis with the Domain Boundary Element Method Formulation, *Computational Mechanics*, **34**, 387-399 (2004).
- [3] G.D. Hatzigeorgiou & D.E. Beskos Dynamic Elastoplastic Analysis of 3-D Structures by the Domain/Boundary Element Method, *Computer & Structures*, **80**, 339-347 (2002).
- [4] J. Hadamard *Lectures on Cauchy's Problem in Linear Partial Differential Equations*, Dover Publications, New York (1952).
- [5] J. Dominguez *Boundary Elements in Dynamics*, Computational Mechanics Publications, Southampton and Boston (1993).
- [6] G. Stephenson *An Introduction to Partial Differential Equations for Science Students*, Longman (1970).

Meshless Boundary Interpolation: Local and Global Multi-Level Techniques

Csaba Gáspár¹

¹Széchenyi István University, Department of Mathematics
P.O.Box 701, H-9007 Győr, Hungary

Email: gasparcs@sze.hu

Keywords: meshless methods, multi-level methods, boundary interpolation, direct multi-elliptic interpolation.

Abstract. Local schemes are generated based on the method of radial basis functions, which result in large but sparse systems. Replacing the radial basis function interpolation with the multi-elliptic interpolation, global schemes are obtained, however, the use of large and dense matrices are avoided. The computational cost of the resulting meshless method is considerably low, and the method contains no scaling parameter to be optimized. In addition to this, the approach can be extended to more general problems in a straightforward way.

Introduction

Meshless methods have become quite popular because of the fact that they require neither domain nor boundary discretization. Instead, a sufficiently fine set of discrete points is needed. The lack of the structure, however, causes certain numerical difficulties in general. For example, the popular *method of radial basis functions* suffers from the disadvantage of producing large, dense and often severely ill-conditioned linear equations to be solved. A lot of variants of this general approach can be realized in a computationally economical way only in the case when the number of discretization points is relatively low. Otherwise, some special technique, the basic idea of which is often far from the method of radial basis functions have to be applied e.g. *domain decomposition* or *fast multipole evaluation* [2] etc. This remains the case when creating meshless schemes based on the method of radial basis functions using either the direct substitution or the *method of particular solutions*. The boundary versions of the technique (e.g. the *method of fundamental solutions* [1]) result in boundary meshless methods which exhibit the same numerical difficulties.

The use of *local schemes* circumvents the above computational problems. Here the interpolation is used in a local sense, thus, the size of appearing local linear systems becomes much smaller, and the global discrete problem becomes sparse. In this paper, the interpolation subproblem appearing in the construction of meshless schemes is solved by the direct multi-elliptic interpolation method [3,4]. Thus, again global schemes (re-globalized schemes) are obtained, but without introducing large and dense matrices. The schemes can be easily incorporated in the multi-level solution techniques of the multi-elliptic interpolation, resulting in a robust boundary-type meshless method.

Interpolation using radial basis functions

One of the most popular meshless interpolation techniques is based on the method of radial basis functions (rbfs). Here the interpolation function is defined as a linear combination of shifted rbfs:

$$u(x) = \sum_{j=1}^N \alpha_j \Phi(x - x_j), \quad (1)$$

with a properly chosen circularly symmetric function Φ , e.g.: Hardy's multiquadric function ($\Phi(r) := \sqrt{r^2 + c^2}$ with a scaling parameter c) or the thin plate splines of Duchon: ($\Phi(r) := r^2 \log r$, no scaling parameter involved). To make the approximation more exact, Equation (1) is often completed with low-order polynomials (augmented interpolation):

$$u(x) = \sum_{j=1}^N \alpha_j \Phi(x - x_j) + \sum_{j=1}^M a_j p_j(x) \quad (2)$$

To determine the unknown coefficients α_j , a_j , one has to solve the following *interpolation equations*:

$$\sum_{j=1}^N \alpha_j \Phi(x_k - x_j) + \sum_{j=1}^M a_j p_j(x_k) = u_k \quad (k=1,2,\dots,N) \quad (3)$$

completed with the orthogonality conditions:

$$\sum_{j=1}^N \alpha_j p_k(x_j) = 0 \quad (k=1,2,\dots,M) \quad (4)$$

If the applied radial basis function Φ is globally supported, this results in a large, dense and often ill-conditioned matrix, which can cause numerical difficulties.

The direct multi-elliptic interpolation. Here the interpolation function is assumed to satisfy a higher order multi-elliptic auxiliary partial differential equation, typically of the form

$$(\Delta - c_1^2 I)(\Delta - c_2^2 I)u = 0 \quad \text{in } \Omega_0 \setminus \{x_1, x_2, \dots, x_N\} \quad (5)$$

supplied with the interpolation conditions as special (pointwise) boundary conditions. The domain Ω_0 can be chosen in a practically arbitrary way, such that $x_1, x_2, \dots, x_N \in \Omega_0$ are satisfied. Along the boundary of Ω_0 , any regular boundary conditions can be prescribed. It can be shown [3] that this problem has a unique solution in the Sobolev space $H^2(\Omega_0)$ and the solution can be uniquely represented in an rbf-like form:

$$u(x) = w(x) + \sum_{j=1}^N \beta_j \Phi(x - x_j), \quad (6)$$

where the function w satisfies Equation (5) everywhere (including also the interpolation points), and Φ is the fundamental solution of the applied multi-elliptic operator. In the special case $c_1 = c_2 = 0$, we obtain the biharmonic interpolation, which is closely related with the thin plate splines. If $c_1 = c_2 = c$, the bi-Helmholtz interpolation is obtained, where the parameter c plays some scaling role. To solve the multi-elliptic problem (5), special numerical techniques can be applied based on the quadtree subdivision and multi-level techniques. The method is extremely economical from computational point of view: the overall computational cost is $O(N \log N)$ only, and the use of large, dense and ill-conditioned matrices is completely avoided.

Meshless methods based on interpolation

Consider the 2D model problem in a bounded domain Ω :

$$\Delta u = f \quad (7)$$

supplied with e.g. Dirichlet boundary condition: $u|_{\Gamma} = u_0$ (where Γ denotes the boundary of Ω). The *method of particular solutions* gives the solution as a sum of a particular solution and a homogeneous solution: $u = v + w$, where $\Delta v = f$ in Ω (no boundary condition is prescribed) and $\Delta w = 0$ (supplied with modified boundary condition: $w|_{\Gamma} = u_0 - v|_{\Gamma}$). By applying an rbf-like interpolation for the source function f , a particular solution is immediately obtained:

$$v(x) = \sum_{j=1}^N \alpha_j \Psi(x - x_j) + \sum_{j=1}^M a_j q_j(x), \quad (8)$$

where $\Delta \Psi = \Phi$ and $\Delta q_j = p_j$. Such functions Ψ and q_j can be easily found in general. Thus, the problem is reduced to the (meshless) solution of the homogeneous problem. This can be performed e.g. by

the *method of fundamental solutions* [1] It should be pointed out, however, that these tasks inherit the computational disadvantages of the rbf-method. This can be avoided by using multi-elliptic interpolation.

Meshless methods based on multi-elliptic interpolation. For constructing a particular solution, the multi-elliptic interpolation approach results in the following algorithm:

- Perform a biharmonic interpolation for the source function f , using a quadtree cell system generated by the interpolation points. Thus, an interpolated value is attached to each cell center.
- Solve the original problem on the same quadtree grid.

The homogeneous solution requires a different approach. If the homogeneous problem is solved on the same quadtree cell system, the number of the boundary points has to be extremely high. Otherwise, boundary singularities are generated which completely destroy the solution. To overcome this difficulty, the regularized method of fundamental solutions or the boundary reconstruction method [5] can be applied. It is also possible to approximate the homogeneous problem $\Delta w = 0$ by a Laplace-Helmholtz equation $\Delta(\Delta - c^2 I)w = 0$ where the scaling parameter c is inversely proportional to the characteristic distance of the boundary points [4]. However, a common disadvantage of the above approaches is that they are based on a carefully chosen scaling parameter which must be uniform in the whole domain. If this parameter is not defined in a proper way, boundary singularities and/or poor approximation can occur. In addition to it, the treatment of more general problems is not straightforward.

Local schemes

These problems can be avoided by applying localized schemes i.e. by constructing generalized finite difference schemes on the basis of the applied interpolation. A possible way to construct local schemes is as follows. Assume that the homogeneous equation $\Delta u = 0$ (supplied with Dirichlet boundary conditions) is to be solved in a domain Ω which is discretized by the unstructured set of points x_1, x_2, \dots, x_N . Let x_k be a fixed interpolation point and let $x_1^{(k)}, x_2^{(k)}, \dots, x_{N_k}^{(k)}$ be some neighboring interpolation points chosen from a predefined neighborhood of x_k . Let h_k be the characteristic distance between x_k and its neighbors. Let $\tilde{x}_N^{(k)}, \tilde{x}_W^{(k)}, \tilde{x}_S^{(k)}, \tilde{x}_E^{(k)}$ be fictitious points lying in the main directions at the distance of h_k from x_k . Using an rbf-interpolation, generate the interpolated values at these points:

$$\tilde{u}(\tilde{x}_N^{(k)}) := \sum_{j=1}^{N_k} \alpha_j^{(k)} \Phi(\tilde{x}_N^{(k)} - x_j^{(k)}) + \sum_{j=1}^M a_j^{(k)} p_j(\tilde{x}_N^{(k)}), \quad (9)$$

and define $\tilde{u}(\tilde{x}_W^{(k)}), \tilde{u}(\tilde{x}_S^{(k)}), \tilde{u}(\tilde{x}_E^{(k)})$ in a similar way. Finally, update the value at the point x_k by the Seidel form

$$u_k := \frac{1}{4} (\tilde{u}(\tilde{x}_N^{(k)}) + \tilde{u}(\tilde{x}_W^{(k)}) + \tilde{u}(\tilde{x}_S^{(k)}) + \tilde{u}(\tilde{x}_E^{(k)})), \quad (10)$$

This approach can be easily extended to more general differential equations and/or more general boundary conditions in a straightforward way.

The updated values can be simply expressed as a linear combination of the values belonging to the neighboring points. To show this, consider the rbf-interpolation form of the updated value:

$$\begin{aligned} u_k &= \sum_{j=1}^{N_k} \alpha_j^{(k)} \frac{\Phi(\tilde{x}_N^{(k)} - x_j^{(k)}) + \dots + \Phi(\tilde{x}_E^{(k)} - x_j^{(k)})}{4} + \sum_{j=1}^M a_j^{(k)} \frac{p_j(\tilde{x}_N^{(k)}) + \dots + p_j(\tilde{x}_E^{(k)})}{4} =: \\ &= \sum_{j=1}^{N_k} \alpha_j^{(k)} \beta_j^{(k)} + \sum_{j=1}^M a_j^{(k)} b_j^{(k)} = \left\langle \begin{pmatrix} \mathbf{a}^{(k)} \\ \mathbf{a}^{(k)} \end{pmatrix}, \begin{pmatrix} \mathbf{\beta}^{(k)} \\ \mathbf{b}^{(k)} \end{pmatrix} \right\rangle \end{aligned} \quad (11)$$

The components of the vectors $\mathbf{a}^{(k)}$ and $\mathbf{a}^{(k)}$ are defined by the local interpolation and the orthogonality conditions:

$$\begin{aligned} \sum_{j=1}^{N_k} \alpha_j^{(k)} \Phi(x_r^{(k)} - x_j^{(k)}) + \sum_{j=1}^M a_j p_j(x_r^{(k)}) &= u_r, & (r = 1, 2, \dots, N_k) \\ \sum_{j=1}^{N_k} \alpha_j^{(k)} p_r(x_j^{(k)}) &= 0 & (r = 1, 2, \dots, M) \end{aligned} \quad (12)$$

In a more compact form:

$$\begin{pmatrix} A^{(k)} & B^{(k)} \\ (B^{(k)})^* & 0 \end{pmatrix} \begin{pmatrix} \mathbf{a}^{(k)} \\ \mathbf{a}^{(k)} \end{pmatrix} = \begin{pmatrix} \mathbf{u}^{(k)} \\ \mathbf{0} \end{pmatrix} \quad (13)$$

Substituting this expression into Equation (11), we obtain that the updated values can be expressed as:

$$u_k = \sum_{j=1}^{N_k} u_j^{(k)} w_j^{(k)} = \left\langle \begin{pmatrix} \mathbf{u}^{(k)} \\ \mathbf{0} \end{pmatrix}, \begin{pmatrix} \mathbf{w}^{(k)} \\ \mathbf{v}^{(k)} \end{pmatrix} \right\rangle, \quad (14)$$

where the vectors $\mathbf{w}^{(k)}$ and $\mathbf{v}^{(k)}$ are the solution of the local system

$$\begin{pmatrix} A^{(k)} & B^{(k)} \\ (B^{(k)})^* & 0 \end{pmatrix} \begin{pmatrix} \mathbf{w}^{(k)} \\ \mathbf{v}^{(k)} \end{pmatrix} = \begin{pmatrix} \mathbf{\beta}^{(k)} \\ \mathbf{b}^{(k)} \end{pmatrix} \quad (15)$$

Equation (14) is a Seidel form of the local scheme of the Laplace equation. Equation (15) is to be solved for each interpolation point x_k but only once. This requires a moderate computational cost, since the number of the neighboring points included in the scheme is limited and independent of the total number of the interpolation points N . The obtained scheme is not symmetric in general, however, very good convergence properties have been observed [6].

A natural question is the proper definition of the interpolation points, since in connection with boundary-type methods, only the boundary points can be assumed to be predefined. Another natural idea is to replace the augmented rbf-interpolation appearing in the local schemes with multi-elliptic interpolation, which makes the schemes global again (in a special sense). This will be investigated in the next section.

Re-globalized schemes using multi-elliptic interpolation

Consider again the homogeneous model problem $\Delta u = 0$ (supplied with Dirichlet boundary conditions, for simplicity). Assume that a set of unstructured points $x_1, x_2, \dots, x_N \in \Omega$ is given. The boundary $\Gamma := \partial\Omega$ is discretized by the points $x_{N+1}, x_{N+2}, \dots, x_{N+K} \in \Gamma$.

The local scheme construction strategy immediately suggests the following iterative algorithm:

- *Step 1.* Construct a multi-elliptic interpolation function \tilde{u} based on the interpolation points x_1, x_2, \dots, x_{N+K} and the values u_1, u_2, \dots, u_{N+K} . Along the boundary, the values u_{N+1}, \dots, u_{N+K} are prescribed.
- *Step 2.* For each inner interpolation point x_k ($k = 1, 2, \dots, N$), evaluate the interpolation function \tilde{u} at the fictitious neighboring points $\tilde{x}_N^{(k)}, \tilde{x}_W^{(k)}, \tilde{x}_S^{(k)}, \tilde{x}_E^{(k)}$ lying in the main coordinate directions around x_k at the distance h_k .
- *Step 3.* Update the value u_k by the Seidel scheme $u_k := \frac{1}{4}(\tilde{u}(\tilde{x}_N^{(k)}) + \tilde{u}(\tilde{x}_W^{(k)}) + \tilde{u}(\tilde{x}_S^{(k)}) + \tilde{u}(\tilde{x}_E^{(k)}))$
- *Step 4.* Repeat the procedure from *Step 1*.

The algorithm can be significantly simplified if initially no inner points are given (which is quite natural in the case of boundary-type methods). In this case, using a quadtree cell system generated by the boundary points, the inner interpolation points can be defined to coincide with the inner cell centers: the distance of these cell centers and the boundary should exceed the local characteristic distance of the neighboring boundary points. The Seidel scheme can be easily incorporated in the multi-level structure of the interpolation. Omitting the details, the following algorithm is obtained:

- *Step 1.* Generate a quadtree cell system based on the boundary points only.
- *Step 2.* Select the cells located in the vicinity of the boundary points. The distance of these cell centers and the boundary has to be at most the local characteristic distance of the boundary points. These cells are considered “near-boundary” cells, which cover the boundary.
- *Step 3.* Solve the following pair of problems on the cell system. At the near-boundary cells, a biharmonic interpolation is carried out based on the boundary points and the associated boundary values. At the remaining cells, the original partial differential equation (in the case of the model problem, the Laplace equation) has to be solved.

Step 3 – which is the heart of the algorithm – can be performed in a multi-level way, as it is usual in multi-elliptic interpolation techniques. Thus, the overall computational cost is $O(K \log K)$ only.

Roughly speaking, in Step 2, the boundary is covered by a narrow stripe of the near-boundary cells. Step 3 is a biharmonic-type boundary interpolation coupled with the original problem in the middle of the domain. The boundary interpolation assures that no numerical singularities arise at the boundary. However, the boundary interpolation is restricted to a narrow vicinity of the boundary, so that the approximation remains satisfactory.

A numerical example. We illustrate the technique through the following simple example. Consider the function defined by $u(x, y) := (1 - x)y$, which satisfies the Laplace equation. Let Ω be a square defined by the inequalities $\frac{1}{4} < x, y < \frac{3}{4}$. The Dirichlet boundary condition is defined in a consistent way. The boundary of the domain Ω is discretized by 48 boundary points.

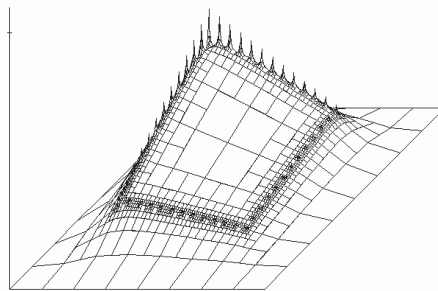


Figure 1. Direct solution of the original model problem on a quadtree cell system. Boundary singularities are generated

First, the model problem itself is solved on a quadtree cell system generated by the boundary points. The result can be seen in Figure 1. Due to the rough boundary discretization, boundary singularities are generated at the boundary points, which destroy the exactness of the method. The relative error measured in discrete L_2 -norm is 13.62%.

Figure 2 shows the result of the above outlined re-globalized method based on a biharmonic interpolation along the boundary. Observe that the boundary singularities are completely removed. The relative error is reduced to 0.90%.

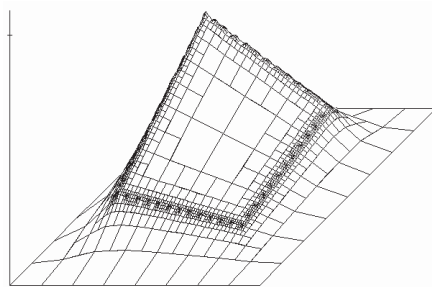


Figure 2. Solution of the model problem by re-globalized schemes with a biharmonic interpolation. Boundary singularities are removed

Summary and Conclusions

The rbf-method and the multi-elliptic interpolation have been applied to constructing meshless schemes for the homogeneous problem. Using a simple local augmented rbf-interpolation, localized meshless schemes are constructed as a generalization of traditional finite difference schemes. The same idea is utilized by replacing the rbf-interpolation with multi-elliptic interpolation. This results in a re-globalized scheme, which requires a boundary discretization only, since the inner interpolation points are generated automatically by the quadtree algorithm. The algorithm avoids the use of large, dense and ill-conditioned matrices, while the computational cost remains low.

Acknowledgement: The research was supported by the Hungarian National Research Fund (OTKA) under the project No. T047287.

References

- [1] C.J.S.Alves, C.S.Chen and B.Sarler *The method of fundamental solutions for solving Poisson problems. Int. Series on Advances in Boundary Elements* **13** (Proceedings of the 24th Int. Conf. on the Boundary Element Method incorporating Meshless Solution Seminar (ed. C.A.Brebbia, A.Tadeu, V.Popov)) 67-76, WitPress, Southampton, Boston (2002).
- [2] R.K.Beatson and W.A.Light *Fast evaluation of radial basis functions: methods for two-dimensional polyharmonic splines. IMA Journal of Numerical Analysis*, **17**, 343-372. (1997).
- [3] C. Gáspár *Fast multi-level meshless methods based on the implicit use of radial basis functions. Lecture Notes in Computational Science and Engineering*, **26**, 143-160, Springer-Verlag, Berlin, Heidelberg, New York (2002).
- [4] C. Gáspár *A meshless polyharmonic-type boundary interpolation method for solving boundary integral equations. Engineering Analysis with Boundary Elements*, **28/10**, 1207-1216 (2004).
- [5] C. Gáspár *Meshless direct multi-elliptic boundary interpolation applied to mixed problems. Advances in Boundary Element Techniques V (Proc. 5th International Conference on Boundary Element Techniques, held in Lisbon, Portugal, 21-23 July, 2004, ed. by V.M.A.Leitao and M.H.Aliabadi)*, 243-248. (2004).
- [6] C. Gáspár *Global and Local Multi-level Meshless Schemes Based on Multi-Elliptic Interpolation. In: Proceedings of ECCOMAS Thematic Conference on Meshless Methods, held in Lisbon, Portugal, July 11-14, 2005. (ed. by V.M.A.Leitao, C.J.S.Alves, C.A.Duarte)*, B12.1 - B12.6. (2005).